

Benjamin David William May

Properties and Reactions of
Transition Metals and
Transition Metal Complexes in Ionic Liquids

Benjamin David William May

Properties and Reactions of Transition Metals and
Transition Metal Complexes in Ionic Liquids

Benjamin David William May

Properties and Reactions of
Transition Metals and
Transition Metal Complexes
in Ionic Liquids

Erlangen
FAU University Press
2019

Bibliografische Information der Deutschen Nationalbibliothek:
Die Deutsche Nationalbibliothek verzeichnet diese Publikation in der
Deutschen Nationalbibliografie; detaillierte bibliografische Daten sind
im Internet über <http://dnb.d-nb.de> abrufbar.

Autoren-Kontaktinformation: Benjamin May, Department Chemie und
Pharmazie, Lehrstuhl fuer Physikalische Chemie II, Benjamin.May@fau.de,
ORCID: 0000-0003-1886-9372

Bitte zitieren als

May, Benjamin. 2019. *Properties and Reactions of Transition Metals and
Transition Metal Complexes in Ionic Liquids*.

Erlangen: FAU University Press. DOI: 10.25593/978-3-96147-232-1.

Das Werk, einschließlich seiner Teile, ist urheberrechtlich geschützt.
Die Rechte an allen Inhalten liegen bei ihren jeweiligen Autoren. Sie
sind nutzbar unter der Creative Commons Lizenz BY.

Der vollständige Inhalt des Buchs ist als PDF über den OPUS Server
der Friedrich-Alexander-Universität Erlangen-Nürnberg abrufbar:
<https://opus4.kobv.de/opus4-fau/home>

Verlag und Auslieferung:

FAU University Press, Universitätsstraße 4, 91054 Erlangen

Druck: docupoint GmbH

ISBN: 978-3-96147-231-4 (Druckausgabe)

eISBN: 978-3-96147-232-1 (Online-Ausgabe)

DOI: 10.25593/978-3-96147-232-1

Properties and Reactions of Transition Metals and
Transition Metal Complexes in Ionic Liquids

*Eigenschaften und Reaktionen von Übergangsmetallen und
Übergangsmetallkomplexen in Ionischen Flüssigkeiten*

Der Naturwissenschaftliche Fakultät der
Friedrich-Alexander-Universität Erlangen-Nürnberg

zur Erlangung des Doktorgrades Dr rer. nat.

vorgelegt von
BENJAMIN DAVID WILLIAM MAY
aus Lincoln, England

ALS DISSERTATION GENEHMIGT
VON DER NATURWISSENSCHAFTLICHE FAKULTÄT
DER FRIEDRICH-ALEXANDER-UNIVERSITÄT ERLANGEN-NÜRNBERG

TAG DER MÜNDLICHEN PRÜFUNG: 2019-04-16

VORSITZENDER DES PROMOTIONSORGANS: Univ.-Prof. Dr. Thomas Drewello
GUTACHTER: Univ.-Prof. Dr. Hans-Peter Steinrück
Univ.-Prof. Dr. Juergen Schatz

A theory or discipline which purports to be scientific is *pseudo-scientific* if and only if:

1. it has been less progressive than alternative theories over a long period of time, and faces many unsolved problems; but
2. the community of practitioners makes little attempt to develop the theory towards solutions of the problems, shows no concern for attempts to evaluate the theory in relation to others, and is selective in considering conformations and disconformations.

Progressiveness is a matter of the success of the theory in adding to its set of facts explained and problems solved.


— *Why Astrology is a Pseudoscience*, Paul Thagard, *PSA: Proceedings of the Biennial Meeting of the Philosophy of Science Association*, 1 (1978), pp. 223–234.

Publications

During the course of this work, the author contributed to the following publications:

- [1] F. Rietzler, B. May, H.-P. Steinrück et al. 'Switching adsorption and growth behavior of ultrathin [C₂C₁Im][OTf] films on Au(111) by Pd deposition'. In: *Physical Chemistry Chemical Physics* 18 (36 2016), pp. 25143–25150. DOI: 10.1039/C6CP04938A
- [2] X. Tang, M. Brandl, B. May et al. 'Photoinduced degradation of methylammonium lead triiodide perovskite semiconductors'. In: *Journal of Materials Chemistry A* 4 (41 2016), pp. 15896–15903. DOI: 10.1039/C6TA06497C
- [3] B. May, M. Hönle, B. Heller et al. 'Surface-Induced Changes in the Thermo-chromic Transformation of an Ionic Liquid Cobalt Thiocyanate Complex'. In: *The Journal of Physical Chemistry Letters* 8.6 (2017), pp. 1137–1141. DOI: 10.1021/acs.jpcllett.7b00142
- [4] M. Lexow, T. Talwar, B. S. J. Heller et al. 'Time-dependent changes in the growth of ultrathin ionic liquid films on Ag(111)'. In: *Physical Chemistry Chemical Physics* 20 (18 2018), pp. 12929–12938. DOI: 10.1039/C8CP01411F
- [5] B. May, M. Lexow, N. Taccardi et al. 'Reactions of a Polyhalide Ionic Liquid with Copper, Silver, and Gold'. In: *ChemistryOpen* (2018). DOI: 10.1002/open.201800149

Work from some of these publications is adapted and reproduced here. A full list of publications can be found at the author's ORCID profile:

 orcid.org/0000-0003-1886-9372

Contents

Introduction	1
1 Surface-Induced Changes in the Thermochromic Transformation of an Ionic Liquid Cobalt Thiocyanate Complex	5
1.1 Introduction	5
1.2 Methods and Materials	7
1.3 Results and Discussion	9
1.3.1 Bulk Thermochromatic Transition Temperature Range	9
1.3.2 Composition of the Ionic Liquids Studied	9
1.3.3 XP Spectra of the Thiocyanate Core Levels	15
1.3.4 High Temperature Comparison	18
1.3.5 XP Spectra of the Cobalt 2p Core Level	20
1.4 A Thermodynamics Based Explanation for the Near-Surface Behaviour	22
1.5 Conclusion	23
2 XPS of Four Polyhalide Anion Ionic Liquids, and Their Vacuum and Thermal Stability	25
2.1 Introduction	25
2.2 Methods and Materials	27
2.2.1 Ionic Liquid Synthesis	27
2.2.2 XPS Analysis	27
2.2.3 Mass Spectrometry	28
2.3 XPS Results	29
2.3.1 XPS Binding Energy Shifts and Polyhalide Lewis Basicity	33
2.3.2 Halogen Speciation	34
2.4 Mass Spectrometry Results	37
2.5 Conclusion	39
3 Reactions of a Polyhalide Ionic Liquid with Copper, Silver, and Gold	41
3.1 Introduction	41

3.2	Methods and Materials	44
3.2.1	IL Synthesis	44
3.2.2	Metal Foil Corrosion	45
3.2.3	NMR Analysis	46
3.2.4	Scanning Electron Microscopy	46
3.2.5	XPS Analysis	47
3.2.6	Vapour Phase Mass Spectrometry	48
3.3	Bulk Metal Corrosion Results	48
3.4	XPS of Neat [C ₆ C ₁ Im][Br ₂ I] Before and After Reacting With Cu, Ag, Au, and Mo	53
3.5	Vapour Phase Mass Spectrometry	60
3.6	Additional Gold Corrosion Experiments	62
3.6.1	The Effect of Water	63
3.6.2	Possible Carbene Formation	64
3.6.3	Imidazolium vs. Sodium Counter Ion	65
3.7	Conclusion	66
4	Comproportionation of Copper(II) Bromide in the Ionic Liquid 1-hexyl-3-Methylimidazolium Bromide	69
4.1	Introduction	69
4.2	Methods and Materials	70
4.3	Visual Changes	71
4.4	XP Spectra of the Cu ^{II} Solution	72
4.5	SEM of Corroded Copper Foil	79
4.6	Conclusion	82
5	Summary	83
6	Zusammenfassung	87
A	Preliminary investigations of High-Gold Content Ionic Liquids	91
A.1	Introduction	91
A.2	IL Synthesis	91
A.3	XPS of the Gold Saturated ILs	93
A.4	Spontaneous Plating	98
A.5	Reaction with Copper(I) Bromide	104
A.6	XRC of the Saturated ILs	104
A.7	Catalytic Activity	104
A.8	Cyclic voltammetry	105

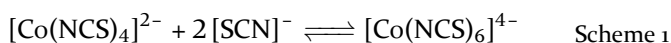
A.9	Differential Scanning Calorimetry and Thermogravimetric Analysis	107
A.10	Infrared Spectroscopy	107
B	New Sample Holders For The ESCA Chamber	109
B.1	The Bolt-On Well Plate	109
B.2	The Well Holder	111
C	Electroplating Stainless Steel and Molybdenum	113
C.1	Degreasing	113
C.2	Masking	114
C.3	Plating	114
	C.3.1 Wood's Nickel Strike	114
	C.3.2 Copper Plating Solution	115
	C.3.3 Gold Plating Solution	115
C.4	Polishing	115
C.5	Results	115
D	Spectra Plotting and Analysis Programs	117
D.1	Basic CasaXPS Export XPS Data Plotting	117
D.2	Plotting and Scaling Dual-Analyser XPS Data	119
D.3	Plotting Hiden Mass Spectra	124
D.4	Plotting Keithley Cyclic Voltammograms	127
D.5	Plotting Setaram TG-Analyser Data	131
D.6	Plotting Jasco FT/IR Data	134
E	Charge Correction in the ILSS Group	137
F	Graphics Standard For Thesis Work	143
F.1	Colour	143
F.2	Line Weights and Dashes	144
F.3	Dimensions	144
F.4	Micrographs	144
	Bibliography	147

Introduction

Ionic liquids (ILs) are a broad class of materials that have found a wide range of applications, for example in catalysis,⁶ as electrolytes for dye-sensitised solar cells (DSSCs),⁷ as reusable halogenating agents in organic synthesis,⁸ and in a number of other applications. In several of these applications, the behaviour of transition metals in ionic liquid solution is of interest, either because they are an explicit component of the system (as is the case for some catalysts), or because of the risk that the IL will react with the electrodes and dissolve them (this is an issue in the context of DSSCs). An early review of transition metal catalysts in IL solution was published by Wasserscheid and Keim,⁹ and a more general review of ILs in catalysis by Welton.¹⁰ In those publications ILs are highlighted as active components of catalysis (acting as co-catalysts, activators, and ligands for the transition metal) and as components of biphasic systems (which offer convenient separation of catalytic media and products). ILs are ideal candidates for studies involving ultra high vacuum (UHV) techniques, in particular X-ray photoelectron spectroscopy (XPS), due to their low vapour pressure – a number of systems have already been investigated by XPS.^{11,12} In the study of transition metals in ionic liquid solution, XPS offers access to information not accessible by more conventional techniques such as UV-vis or IR spectroscopy. The chemical shifts seen in XPS provide an insight into the chemical environment of ligands and metal centers (including metal oxidation state), and gives clues about the structure of complexes. Moreover, XPS can probe surface structure and phenomena, owing to its limited information depth (typically 7–9 nm, depending on kinetic energy^{13,14}).

In many applications, the behaviour of transition metal species at the surface or interface of an ionic liquid phase is of particular importance – for example in the supported ionic liquid phase (SILP) concept^{6,15} – here

the limited information depth of XPS allows for the detection and study of phenomena in the near-surface region. This capability is put to use in chapter 1, where in addition to demonstrating that XPS can be used to track the coordination number change of a Co-centred complex via the ligand-derived signals, XPS also revealed that there is a significant difference in the transition temperature in the bulk and in the near-surface region ($\sim 30^\circ\text{C}$ higher at the surface). Angle-resolved XPS gave insight into the reason why: the surface of the thermochromatic solution is semi-ordered, with the free thiocyanate anions orienting themselves to point towards the vacuum. Thus, the shift in transition temperature of the equilibrium reaction

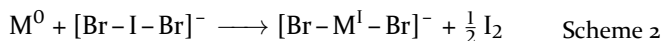


is attributed to the presence of the outer surface, which induces an ordering of the near-surface region, lowering the reaction entropy in the near-surface region compared to the bulk. In addition, an effective dilution of the cobalt complex was observed, which was attributed to the formation of a secondary solvation shell of $[\text{SCN}]^-$ ions.

As mentioned above, polyhalide ILs are of interest as electrolytes for DSSCs, and in this application the potential corrosion of electrode materials is an issue of concern. Before studying the corrosion process itself in chapter 3, a study of trihalide ILs was undertaken in chapter 2. Here the synthesis of four polyhalide $[\text{C}_6\text{C}_1\text{Im}]^+$ -based ILs and their characterisation by XPS and vapour phase mass spectrometry is reported. XPS was used to infer the structure of the polyhalide anions, probe the degree of inter-molecular interaction, and quantify the ILs vacuum stability. Mass spectrometry (MS) was used to identify the vacuum decomposition product of the polyhalide ILs. One can infer from the generally large shift of the halogen peaks to higher binding energy that the anions are charge-delocalised, with the anionic charge spread out over all of the halogen centres. Additionally, the symmetry of the $[\text{Cl}_2\text{I}]^-$ and $[\text{Br}_2\text{I}]^-$ anions is confirmed by the presence of only one set of peaks in the respective halogen spectra – an important finding since these trihalide species are known to be asymmetrical in other salts.^{16,17} For the other two anions studied, definite conclusion are not possible, but XPS clearly reveals that the speciation is not simply the nominal species. The XPS of $[\text{BrI}_2]^-$ does illustrate a potential pit fall of UHV techniques – this anion is not vacuum-stable, and loses a significant amount of iodine under vacuum (this also demonstrates the value of the quantitative

nature of XPS). The $[\text{Br}_2\text{I}]^-$ anion was found to be generally vacuum-stable, although a noticeable loss of iodine was noted after 70 h – the vacuum stability was improved by adding an excess of free Br^- , forming the supposed polyhalide species $[\text{Br}_3\text{I}]^{2-}$. All four were observed to be very weak lewis bases, seen in XPS as a low degree of cation-anions charge transfer.¹⁸

With two vacuum-stable trihalide ILs identified, corrosion of potential electrode materials by a trihalide IL could be studied. In chapter 3, mass loss, vapour phase mass spectrometry, and XPS were used to study the oxidative dissolution of the group 11 metals copper, silver, and gold by the trihalide IL $[\text{C}_6\text{C}_1\text{Im}][\text{Br}_2\text{I}]$. In this study, XPS was most useful as a probe of oxidation state, and for inferring coordination structure. The group 11 metals were found to be dissolved in the +1 oxidation, and the overall reaction



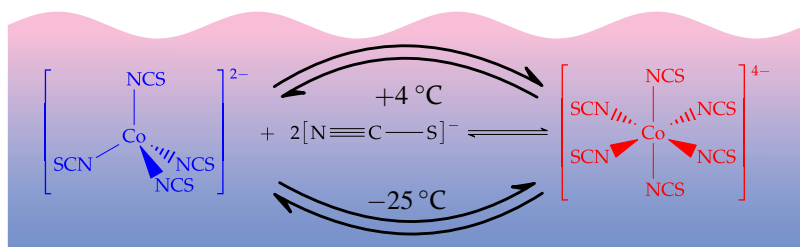
was proposed. This mechanism is corroborated by the vapour phase MS results, which show that when in contact with the metal the trihalide IL evolves molecular iodine, I_2 , and the consistent loss of iodine observed in the post-corrosion samples by XPS. The $[\text{Br}-\text{M}^{\text{I}}-\text{Br}]^-$ structure was inferred based on the fact that after corrosion the bromide ligands are still in a delocalised environment (which was itself inferred from the lack of large shift compared to the neat trihalide). The dissolution of Au^{I} in IL solution is particularly notable because this species is not typically stable in aqueous solution. This reaction had the potential to be more complex than the reaction given in scheme 2; specifically the C2 proton of the imidazolium cation could play a role (potentially forming a carbene species), the imidazolium cation could be acting to stabilise the dissolved metal thus enhancing the corrosion rate, and water could affect the reaction rate. In regards to probing the role of the C2 proton, NMR of $[\text{C}_6\text{C}_1\text{Im}][\text{Br}_2\text{I}]$ after corroding gold and XPS of the C2 methylated $[\text{C}_4\text{C}_1\text{C}_1\text{Im}][\text{Br}_2\text{I}]$ rule out the formation of a carbene species and demonstrate that the C2 proton does not play a significant role in metal corrosion. However, experiments with $\text{Na}[\text{Br}_2\text{I}]$ in aqueous solution showed that whilst aqueous trihalide solutions are able to corrode gold, the rate is far slower than with an IL solvent. The imidazolium cation is likely stabilising the complex formed, probably by forming a solvation shell around the dissolved complex. Corrosion reactions run

under anhydrous and water-saturated showed that water has no effect on the corrosion rate or the species that ultimately dissolves.

From the chemistry of copper salts in aqueous solution, at low pH it is possible for Cu^{II} to undergo a comproportionation reaction with Cu^0 and form Cu^{I} ;¹⁹ which raises the question: is the Cu^{I} seen in the previous chapter the direct result of the corrosion reaction, or was Cu^{II} the actual direct product, which then underwent a fast comproportionation reaction to form the Cu^{I} seen in XPS? In chapter 4, a solution of copper(II) bromide in $[\text{C}_6\text{C}_1\text{Im}]\text{Br}$ was prepared and characterised by XPS, with the sample analysed on molybdenum and on copper metal. On copper, a rapid comproportionation reaction was seen, leading to the reduction of the Cu^{II} in solution to Cu^{I} and a corresponding oxidation and dissolution of the copper metal. This reaction was not seen to occur with the sample on the molybdenum sample holder. Here, the determination of metal oxidation state by XPS was key. The ability to directly observe the oxidation state of the copper in solution allows for the observation of the comproportionation reaction. Exposure of the fully comproportionated sample on copper to air for 32 d leads to the reoxidation of the copper in solution, and the formation of a solid material – the actual identity of this material is not known, due to excessive contamination of the sample. The determination of the oxidation state of the copper in solution was confirmed by measurements of a reference solution made by dissolving both CuBr_2 and CuBr in the halide IL. Scanning electron micrographs of a copper foil post-exposure to the Cu^{II} solution show that etching produces a rough surface, as expected, but that in contrast to etching by the trihalide IL studied in chapter 3 there was a notable absence of etching pitting – a result potentially of importance in applications such as microfabrication.

1 Surface-Induced Changes in the Thermochromic Transformation of an Ionic Liquid Cobalt Thiocyanate Complex

PUBLISHED AS: Surface-Induced Changes in the Thermochromic Transformation of an Ionic Liquid Cobalt Thiocyanate Complex³



1.1 Introduction

When applying thin liquid films, for example, in sensors, chromatography, lubrication, and coating technologies, the interface between the liquid film to its environment becomes increasingly relevant as the films become thinner and thinner. For such systems, it is important to know whether and to what extent the interfacial properties are different from those in the bulk.

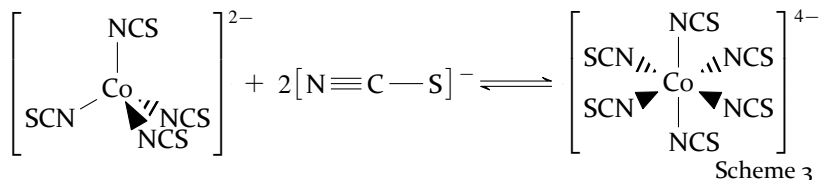
One prominent example of thin liquid film applications is the new and very successful concept of “Supported Ionic Liquid Phase” (SILP) catalysis.⁶ In SILP, a high surface area solid substrate is covered with a thin ionic liquid (IL) film, which typically contains a dissolved transition metal (TM) complex^{15,20–22} as the catalytically active species, with the IL acting as a nonvolatile solvent for both the reactants and the complex. In addition to their solvent characteristics, ILs also have the potential

to provide ionic ligands for the desired complex with concentrations far above those achieved in traditional molecular solvents, reducing potential ligand exchange by other solvated molecules. To optimize such high surface area systems employing dissolved TM complexes, a full understanding of the near-surface region and possible differences in the behaviour of a dissolved complex near the surface as compared to its bulk behaviour is highly desired, which requires surface-sensitive analytics.

Because of their extremely low vapour pressure, the near-surface region of ILs can, in contrast with most of the commonly used molecular solvents, be studied using the powerful techniques of ultrahigh vacuum (UHV) based surface science, such as X-ray photoelectron spectroscopy (XPS). While XPS studies on solid surfaces are restricted to the properties of static transition metal complexes,²³⁻²⁵ investigations in the liquid state also allow for studying dynamical phenomena,^{11,26-30} that is, time- or temperature-dependent processes. Because of its inherent surface sensitivity, XPS provides information on changes of chemical states within the topmost 1–10 nm. This near-surface region can indeed behave quite differently from the bulk, as was recently demonstrated in an XPS study of CO₂ capture using amine functionalised ILs: The specific CO₂/amine chemistry found in the topmost IL layers leads to a much higher uptake capacity in the near-surface region than the bulk³¹

Herein, XPS is applied for the first time to a thermodynamic metal complex equilibrium based on ILs containing the doubly negatively charged tetrathiocyanatocobaltate(II) ([Co(NCS)₄]²⁻) anion, a system introduced by Peppel et al³² Osborne et al³³ reported thermochromatic behaviour of this anion, formed by dissolving cobalt(II) isothiocyanate (Co(NCS)₂) in the IL 1-ethyl-3-methylimidazolium thiocyanate ([C₂C₁Im][SCN]). At room temperature, the complex equilibrium in scheme 3 lies on the left side, as witnessed by the deep blue colour of the tetrahedrally coordinated cobalt anion. Cooling shifts the equilibrium to the right, toward the octahedrally coordinated complex: At around –40 °C, the red octahedral form dominates in the bulk, as shown by UV-vis and IR absorption spectroscopy³³ It should be noted that the transition between the two complexes is accompanied by not only changes in optical absorption but also by changes in magnetic properties³³ and conductivity³⁴ Very recently, it was also demonstrated that the equilibrium is shifted to the right by applying external pressure.³⁴ These

characteristics make this complex system very interesting for sensor applications.



1.2 Methods and Materials

1-Ethyl-3-methylimidazolium thiocyanate ($[\text{C}_2\text{C}_1\text{Im}][\text{SCN}]$, **IL-1**) was purchased from IoLiTec (assay >98 %, halides <2 %) and used without further processing. 1-Ethyl-3-methylimidazolium tetrathiocyanatocobaltate(II) ($[\text{C}_2\text{C}_1\text{Im}]_2[\text{Co}(\text{NCS})_4]$, **IL-2**) was purchased from KCT-Chemie UG and used without further processing. The thermochromatic IL $[\text{C}_2\text{C}_1\text{Im}]_5[\text{Co}(\text{NCS})_4][\text{SCN}]_3$, **IL-3**, was prepared by mixing 1.978 g (11.69 mmol) of **IL-1** and 2.001 g (3.90 mmol) of **IL-2** – a 3 : 1 molar ratio.

To determine the range over which the colour change, and thus equilibrium shift, of the thermochromatic IL takes place, a sample of it was sealed in an evacuated ampoule. The ampoule was wrapped in a thermocouple wire, then immersed in a boiling tube of isopropanol cooled to near its freezing point by liquid nitrogen, figure 1.1. In this setup, a stream of dry nitrogen gas was used to prevent condensation forming on the side of the tube, allowing for a clearer video to be recorded. Upon initial immersion, the temperature of the sample rapidly dropped to ca. $-65\text{ }^\circ\text{C}$.

For XPS measurements, macroscopic samples (ca. 0.03 ml) of each IL were placed on molybdenum samples holders and introduced into the Dual Analyser System for Surface Analysis (the DASSA)³⁵ Before any measurements were taken, water and other volatile components were driven off by heating the ILs to $60\text{ }^\circ\text{C}$ for 2 h in the DASSA's preparation chamber (base pressure 2×10^{-10} mbar).

Once degassed, the XPS samples were studied at room temperature ($24\text{ }^\circ\text{C}$) and subsequently at $-10\text{ }^\circ\text{C}$, $-30\text{ }^\circ\text{C}$, $-60\text{ }^\circ\text{C}$, and $-75\text{ }^\circ\text{C}$, with survey and high-resolution scans at each temperature. As a follow up, a cooling and heating cycle from room temperature to $0\text{ }^\circ\text{C}$ and back

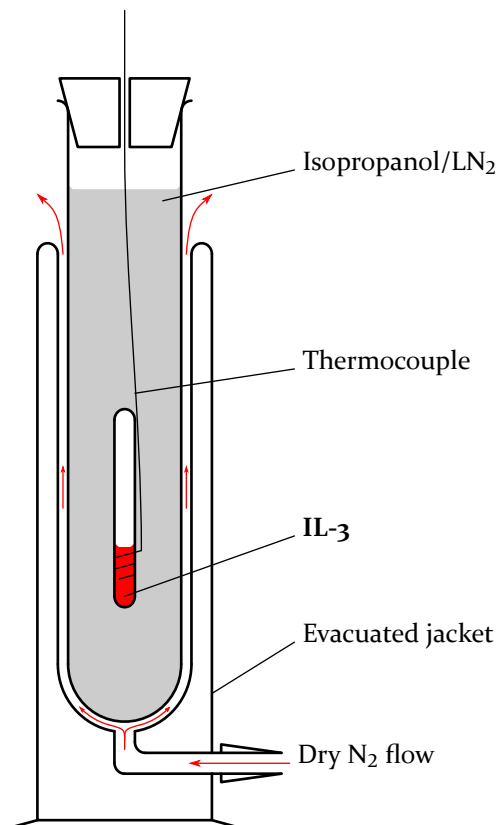


Figure 1.1.: Setup used to monitor the colour change of the thermochromic IL on warming.

was done for the thermochromic IL in 2 °C steps while recording XP spectra. All spectra were taken using a monochromated Al K_α source. High-resolution scans used a pass energy of 35 eV and a dwell time of 1.5 s with an overall energy resolution of 0.4 eV, while survey scans were recorded with a pass energy of 200 eV and a dwell time of 0.5 s. Angle resolved XPS (ARXPS) was done by recording spectra simultaneously with one analyser mounted at 0° (normal emission) and one mounted at 80° (grazing emission), with respect to the surface normal. While

0° electron emission is more bulk sensitive, with an information depth of 7–9 nm (depending on kinetic energy of the excited photoelectrons),^{13,14} emission at 80° is about six times more surface sensitive, with an information depth of 1–1.5 nm.

Because of minor charging effects present even at room temperature, the binding energy values of all spectra were referenced to the N 1s signal of the imidazolium cation (set to 401.82 eV), which is the value measured for **IL-2** at room temperature. The nitrogen signal of the counterion was chosen because the imidazolium cation is expected to be the component least influenced by the complex reaction and provides a sharp and easily distinguishable signal. At temperatures of –60 °C and below, it was sometimes necessary to use an electron flood gun to counteract peak broadening by inhomogeneous charging when sample solidification occurred.

As a cross check, a sample of **IL-3** was placed in a molybdenum reservoir and introduced into a second XPS system, the ESCA chamber.¹⁴ After a degassing step as described above, the sample was scanned at room temperature and 40 °C.

All imidazolium and ligand core levels could be fitted using simple 30 % Lorentzian Pseudo-Voigt functions after Shirley background subtraction. For comparison between the normal emission and 80° spectra, all ARXP spectra were scaled such that the area of the imidazolium N 1s peak was equal to that of the spectra concurrently recorded at 0°.

1.3 Results and Discussion

1.3.1 Bulk Thermochromatic Transition Temperature Range

Frames from the video acquired during the bulk warming experiment are presented in figure 1.2. The colour change (from pink to deep blue) appears to begin at –40 °C and go to completion by –10 °C, with the midpoint around –25 °C. These observations are not significantly different from those of Osborne et al.³³

1.3.2 Composition of the Ionic Liquids Studied

To determine the composition of the ILs, wide-scans and detailed spectra of the relevant core levels are shown in figures 1.3, 1.4, and 1.5, and the corresponding quantitative analysis (taking into account relative sensitivity factors, RSF) is summarised in table 1.1. The spectrum of **IL-1** in

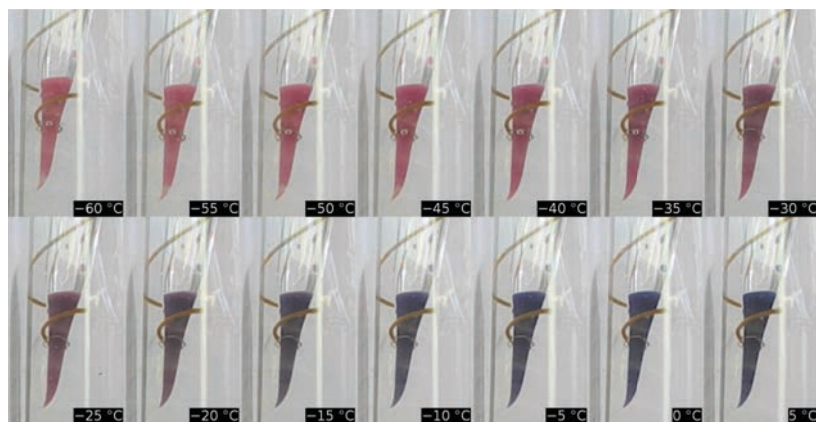


Figure 1.2.: Frames from the video of the colour change of **IL-3** as a function of temperature.

figure 1.3 shows all the expected peaks. Notably, in the C 1s spectra the signal of the alkyl carbon (C_{alkyl} , at ~ 285 eV) is larger than expected. The additional presence of Si 2p and O 1s signals (spectra not shown) indicates a contamination with a surface-active silicone species – this is common, and is typically the result of the ionic liquid (or its starting materials) coming into contact with the silicone grease used on ground glass joints. Note that the excess alkyl carbon and silicon are greatly enriched in the grazing emission scans, consistent with a surface active silicone contaminant, which leads to pronounced attenuation of the IL-related signals; hence, the N 1s signal of the imidazolium ring was used when scaling the 80° spectra. Otherwise, quantification of IL signals, table 1.1, shows stoichiometric composition.

The quantification for **IL-2** (spectra presented in figure 1.4) shows all of the expected elements in the expected amounts. The silicon contamination seen in **IL-1** is not present in **IL-2** – the minimal amount of oxygen present originates most likely from recalcitrant water not driven off during the degassing step.

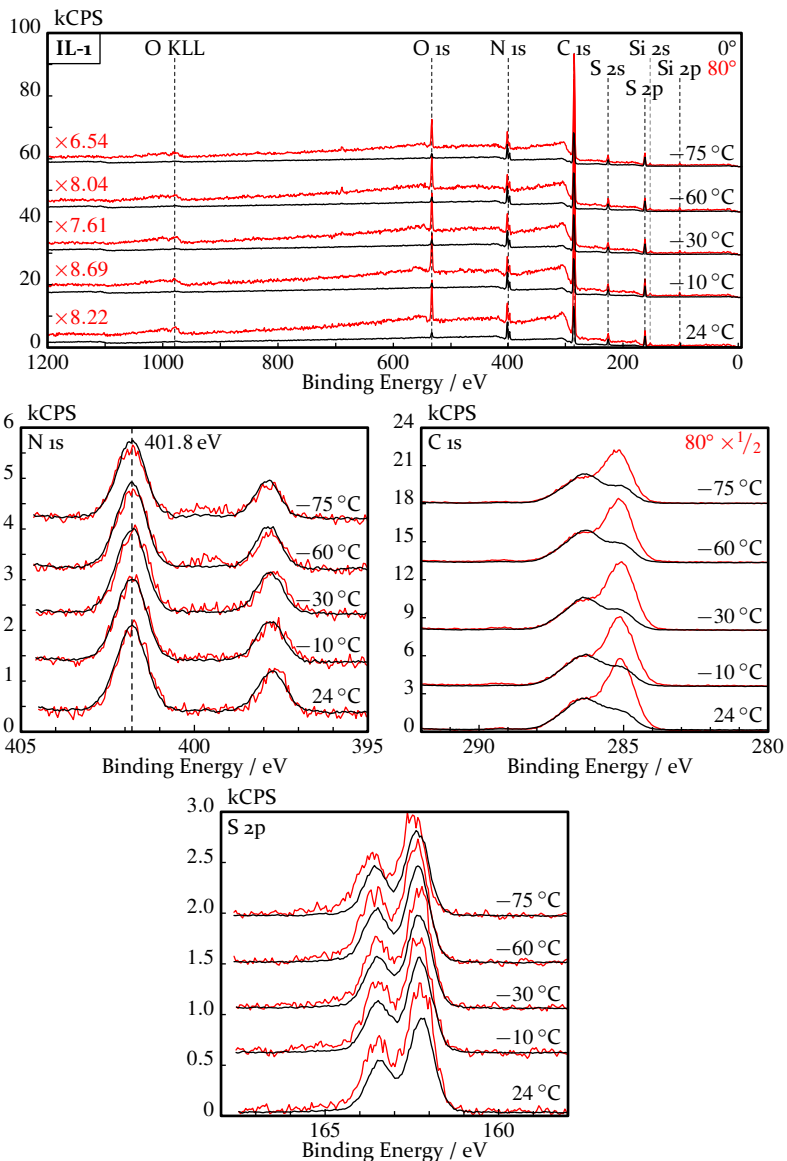


Figure 1.3: Normal (black) and 80° (red, scaled by imidazolium peak area) XPS spectra of IL-1, $[\text{C}_2\text{C}_1\text{Im}][\text{SCN}]$, at 24 °C, -10 °C, -30 °C, -60 °C, and -75 °C.

1 Surface-Induced Changes in an Ionic Liquid Cobalt Thiocyanate Complex

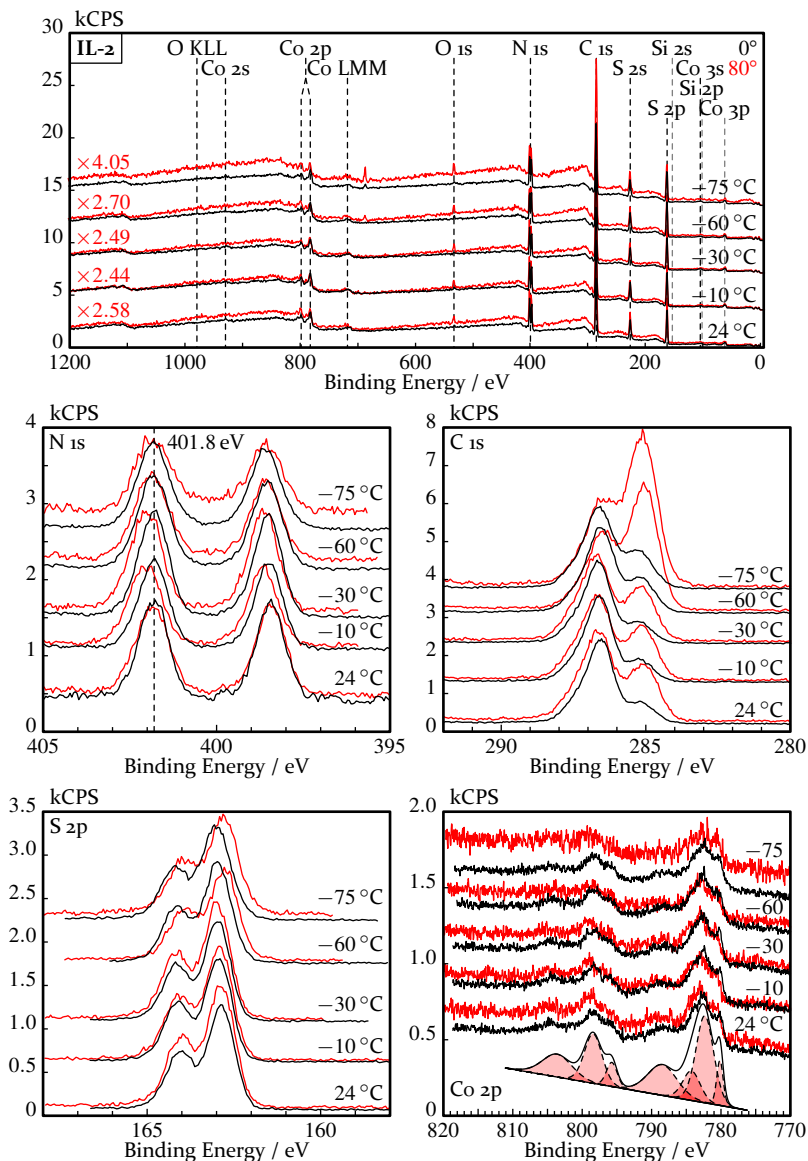


Figure 1.4.: Normal (black) and 80° (red, scaled by imidazolium peak area) XPS spectra of **IL-2**, $[\text{C}_2\text{C1Im}]_2[\text{Co}(\text{NCS})_4]$, at 24 °C, -10 °C, -30 °C, -60 °C, and -75 °C. The fitting of the -10 °C Co 2p spectra at 0° emission angle is also shown.

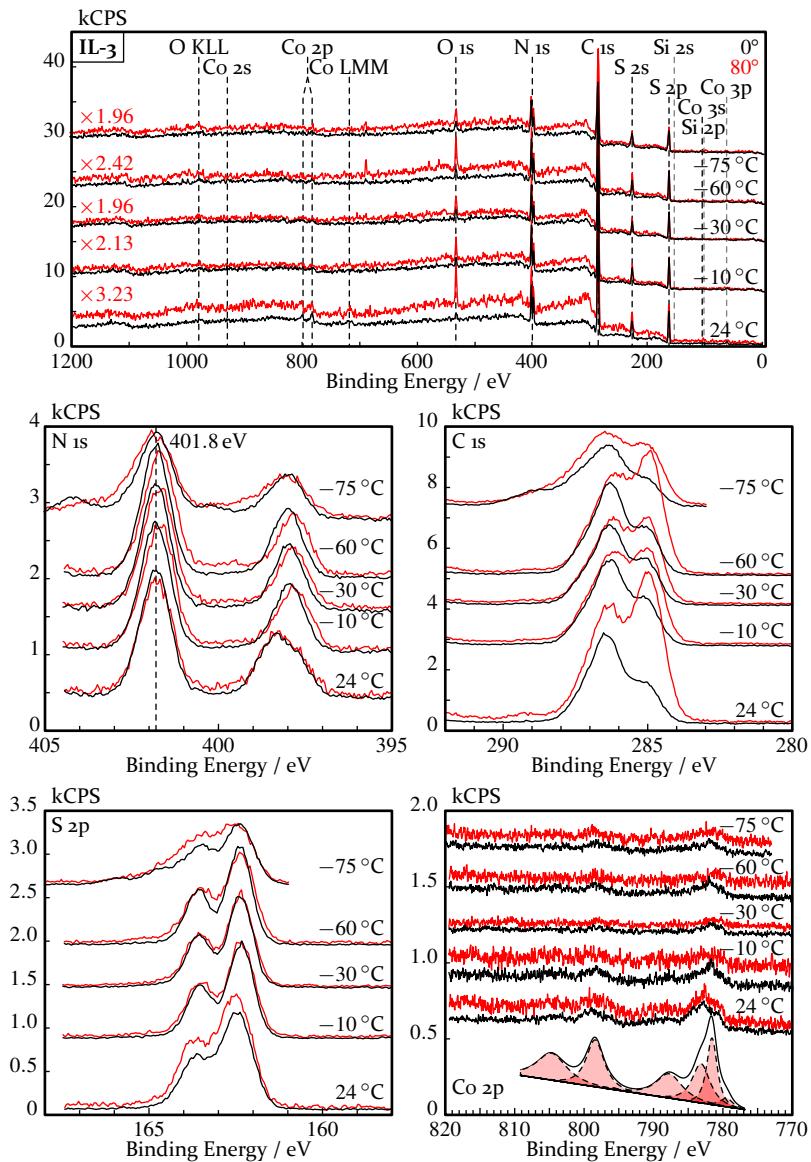


Figure 1.5.: Normal (black) and 80° (red, scaled by imidazolium peak area) XPS spectra of IL-3, $[\text{C}_2\text{C}_1\text{Im}]_5[\text{Co}(\text{NCS})_4][\text{SCN}]_3$, at 24 °C, -10 °C, -30 °C, -60 °C, and -75 °C. The fitting of the -10 °C Co 2p spectra at 0° emission angle.

RSF →	C _{1s}		N _{1s}		S 2p	Co 2p _{3/2}	O 1s	Si 2p
	0.30	alkyl : hetero : NCN	0.46	Im ⁺ : [SCN] ⁻				
IL-1	9.3	2.8 : 4.8 : 1.7	2.9	2 : 0.9	1.0	—	0.5	<0.1
<i>nominal</i>	7	1 : 5 : 1	3	2 : 1	1	0	0	0
IL-2	8.0	1.3 : 5.5 : 1.2	3.9	2 : 1.9	1.9	0.5	0.1	0
<i>nominal</i>	8	1 : 6 : 1	4	2 : 2	2	0.5	0	0
IL-3	9.8	2.5 : 5.8 : 1.4	3.3	2 : 1.3	1.5	0.2	0.5	—
<i>nominal</i>	7.4	1 : 5.4 : 1	3.4	2 : 1.4	1.4	0.2	0	0

Table 1.1.: Quantification of the three ILs studied, based on the 0° emission 24 °C spectra. Values are scaled such that the N_{1s} peak due to the imidazolium ≡ 2.

The quantification of the mixture, **IL-3** (spectra in figure 1.5), also shows excess alkyl carbon (as seen with **IL-1**), and again the alkyl carbon component greatly increases in 80° emission. An excess of oxygen is also present, and in grazing emission an Si 2p signal can be seen in the survey spectra – overall, there is silicone contamination present, but a lesser amount compared to **IL-1**. Unfortunately, a Si 2p region scan was not measured. Neglecting contamination signals, all IL-related elements are present in the expected amounts, to within the accuracy of the technique.

Since the characteristic increase of the S 2p intensity at 80° vs. the more or less unchanged thiocyanate N 1s signal at 0° and 80° are observed for **IL-1** and **IL-3** (both with the surface contamination) and for **IL-2** (without surface contamination), it is believed that this contamination does not affect the conclusions derived below.

1.3.3 XP Spectra of the Thiocyanate Core Levels

N 1s and S 2p normal emission XP spectra of **IL-1**, **IL-2**, and **IL-3** at 24 °C and –10 °C are presented in figure 1.6, for direct comparison – these temperatures are plotted there because the most relevant changes occur in the 24––10 °C range (see below). The full set of spectra can be found above, figures 1.3, 1.4, and 1.5. The imidazolium and thiocyanate N 1s peaks are well-separated – by more than 4 eV. In contrast, the free thiocyanate C 1s signal cannot be distinguished from the imidazolium C_{hetero} peak; moreover, a significant alkyl carbon contamination was detected at 285 eV, and thus, the C 1s region was not used in the following characterisation. The free and cobalt-bound thiocyanate N 1s peaks appear at 397.8 eV and 398.5 eV respectively. The S 2p signal of the free thiocyanate also appears at a lower binding energy (162.2 eV, 2p_{3/2}) compared to the cobalt-bound thiocyanate (162.9 eV). Therefore, with our instrument

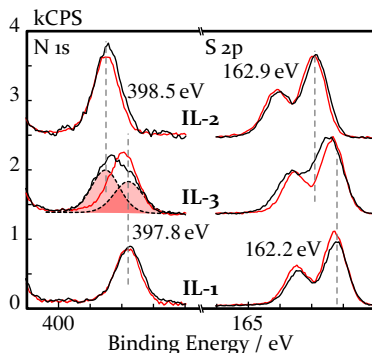


Figure 1.6.: Normal emission N 1s and S 2p regions of the three ILs studied at 24 °C (black) and –10 °C (red). From the top, **IL-2**, **IL-3** and **IL-1**. The deconvolution of the N 1s spectra of **IL-3** at 24 °C is also shown.

resolution of 0.4 eV, the N 1s and S 2p core levels of the two thiocyanate species (free $[\text{SCN}]^-$ and $[\text{NCS}]^-$ bound in the tetrahedral cobalt complex) can be clearly distinguished.

For **IL-1**, the recorded spectra show virtually no changes between 24 °C and -75 °C – figure 1.3. The angle resolved spectra, however, reveal that the free thiocyanate anions are preferentially oriented at the surface – changing the emission angle from 0° to 80°, the sulfur signal shows a ~25% increase in intensity, while the N 1s signal of the anion (at 397.8 eV), increases only by 5–10%. The implication is that the linear free thiocyanate anions in **IL-1** are preferentially oriented within the outermost surface layer, with the sulfur end pointing towards the vacuum and the nitrogen end pointing to the bulk. Similar orientation effects at surfaces have been reported for other IL systems – in most cases, uncharged moieties such as long alkyl chains attached to ionic head groups, as well as CF_3 groups of perfluorinated anions, are consistently reported as pointing preferentially towards the vacuum phase.

¹¹ For $[\text{SCN}]^-$ -based ILs, such strong surface orientation effects have not yet been reported, to the best of our knowledge. One should note that the here observed thiocyanate orientation might extend from the surface layer over several layers further into the bulk, which has been deduced for other IL systems by surface X-ray scattering³⁶ and molecular dynamics simulations;³⁷ such an effect can, however, not be probed with ARXPS.

The ARXPS spectra of **IL-2** at 24 °C also exhibit an increase in the S 2p signal of ~20% in the 80° scans, which is of similar magnitude as observed for **IL-1** – figure 1.4. Again, no temperature dependent changes are observed. Because in the tetrahedrally-coordinated complex no individual orientation of the $[\text{SCN}]^-$ ligands is possible, the observed surface enrichment of sulfur in 80° is attributed to three of the four ligands (that is, one of the tetrahedrons' base planes) being preferentially oriented towards the vacuum. Interestingly, at -60 °C and -75 °C, pronounced surface enrichment of the alkyl carbon contamination occurs concomitantly occurs as shown by the strong increase of the alkyl carbon signal in 80° – figure 1.4 – this may be due to hydrocarbon contamination condensing out of the vacuum at these low temperatures. Similarly, a F 1s signal (likely due to contaminating $[\text{Tf}_2\text{N}]^-$) can be seen in the wide scans of all three ILs at -60 °C and -75 °C.

For both of the neat ILs, cooling does not result in significant changes to peak positions or widths at both normal and grazing emission. After

solidification below $-60\text{ }^{\circ}\text{C}$, charging effects could be observed as signal shifts towards higher binding energy and peak broadening.

The thiocyanate N 1s and S 2p signals of **IL-3** at $24\text{ }^{\circ}\text{C}$ are significantly broader than that of the two neat ILs, as shown by the direct comparison of the spectra taken in 0° (figure 1.6) and in $80\text{ }^{\circ}\text{C}$ (figure 1.5). In particular, the thiocyanate N 1s level reveals two components, which can be described (to within fitting uncertainty) as a superposition of the cobalt-bound thiocyanate in $[\text{Co}(\text{NCS})_4]^{2-}$ at 398.5 eV and of free $[\text{SCN}]^{-}$ at 397.8 eV , at a ratio of $4 : 3$, that is, within the nominal molar ratio expected for the $1 : 3$ **IL-2** : **IL-1** mixture. The room-temperature S 2p spectrum of **IL-3** is also considerably broader than the corresponding spectra of the neat ILs, again due to the presence of species in two different chemical states. Note that due to spin-orbit splitting, the presence of two different species in the S 2p region is less obvious; however, deconvolution by peak fitting is fully in line with the results from the N 1s spectra of **IL-3**. ARXPS at $24\text{ }^{\circ}\text{C}$ again shows an increase in S 2p intensity at 80° (figure 1.5), similar to that of the two neat ILs, indicating that at room temperature the free thiocyanate anions are oriented such that the sulfur end points towards the vacuum and $[\text{Co}(\text{NCS})_4]^{2-}$ anions are present in the outermost layers of **IL-3**.

In contrast with the neat ILs, moderate cooling of **IL-3** to $-10\text{ }^{\circ}\text{C}$, that is, still well above the bulk colour transition temperature of $-25\text{ }^{\circ}\text{C}$, leads to a pronounced narrowing ($\sim 25\%$ decrease in full width at half maximum, FWHM) and intensity loss of the $[\text{SCN}]^{-}$ -related N 1s and the S 2p signals to FWHM values similar to those measured for the neat thiocyanate, with binding energies of 398.0 eV and 162.4 eV , respectively. Interestingly, at $-10\text{ }^{\circ}\text{C}$ and below, the S 2p signal intensity in 80° emission is very close to the one measured in 0° , as is evident from figure 1.5 – which clearly indicates the loss of preferential thiocyanate orientation at the surface. Further cooling, even below the bulk colour transition temperature, does not lead to any further spectral changes until freezing is apparent at $-75\text{ }^{\circ}\text{C}$ (seen as film charging).

From the fine temperature measurements of **IL-3**, shown in figure 1.7, the change in shape of the N 1s thiocyanate signal starts at around $+20\text{ }^{\circ}\text{C}$ and reached the final narrow shape at $+4\text{ }^{\circ}\text{C}$. The spectral changes seen in the $2\text{ }^{\circ}\text{C}$ step cooling and heating cycle are fully reversible. Thus, at (and below) $4\text{ }^{\circ}\text{C}$, the transition from the tetrahedral to the octahedral complex seems to have already occurred in the near-surface region probed by XPS, while in the bulk the transition only occurs at

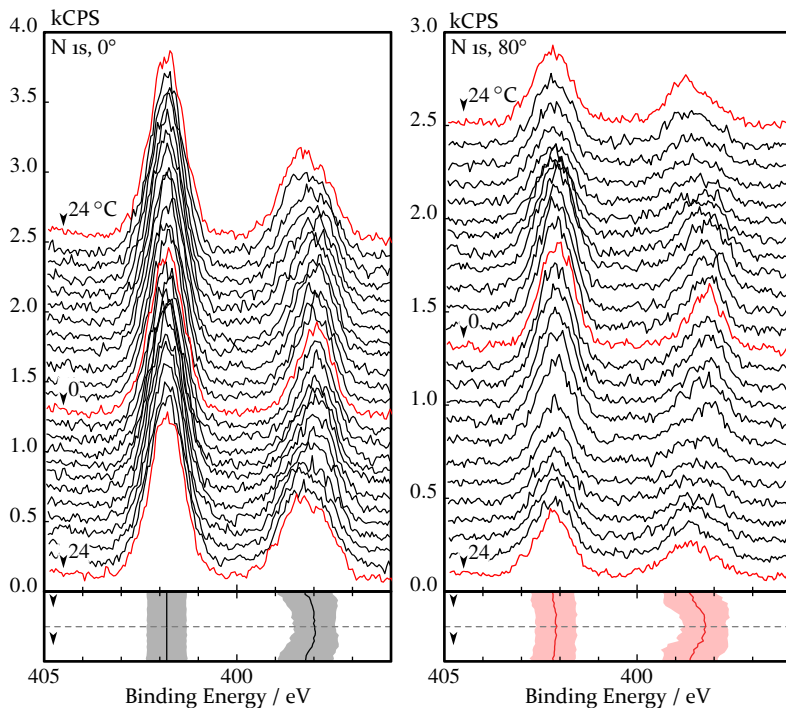


Figure 1.7.: Fine temperature series (2°C steps) measurements of **IL-3** during a cooling and heating cycle, with a schematic representation of peak position and FWHM (bottom). Red spectra were collected at 24°C and 0°C .

significantly lower temperatures. At $+4^{\circ}\text{C}$, beneath the XPS probing depth of 9 nm, free $[\text{SCN}]^{-}$ and $[\text{Co}(\text{NCS})_4]^{2-}$ anions are still present as is clearly shown by the deep-blue colour of the liquid film covering the sample holder. Notably, at -30°C , the **IL-3** film on the sample holder has changed its colour from blue to a pink/red appearance, as witnessed by a visual inspection.

1.3.4 High Temperature Comparison

To rule out considerable errors in the absolute temperature readings of the DASSA thermocouple system, and to eliminate the possibility that pronounced complex equilibrium changes in the near-surface region extend to temperatures above room temperature, a sample of **IL-3** was

placed in a bolt-on reservoir and introduced to the second XPS system (the ESCA). After degassing as described for the DASSA, the sample was measured at room temperature, and then heated to 40 °C.

In the ESCA, non-monochromated Al K α radiation of a SPECS XR-50 X-ray gun, operating at 12.5 kV and 20 mA, was used, leading to broader XP signals than the monochromated Al K α radiation of the DASSA. Spectra were recorded by a VG Scienta R3000, set to a pass energy of 200 eV for wide scans, and 100 eV for detailed region scans (overall energy resolution: 0.8 eV). Background subtraction, peak fitting and charge correction were as described above.

A comparison of the normal emission spectra collected in the ESCA chamber and the DASSA spectra is presented in figure 1.8.

Note that due to the reduced energy resolution of the ESCA system, the deconvolution of the thiocyanate N 1s signal (at around 398 eV) at room temperature into free anion and Co-bound ligand is less obvious, compared to the corresponding DASSA spectrum. On heating to +40 °C, no significant changes in peak shape, position, or width of the thiocyanate related N 1s core levels of **IL-3** are visible – ruling out any significant changes with respect to the room temperature situation. Further, there is no change in the apparent ratio between the imidazolium peak area and the thiocyanate peak area. Figure 1.8 also includes spectra recorded in the ESCA chamber at –10 °C, showing that even with the non-monochromated source, the spectral changes associated with the transition can be seen (namely the narrowing of the thiocyanate signal and an apparent increase in its separation from the imidazolium signal). Note that the change in complex equilibrium position in the near-surface region occurs in the same temperature window as has been discussed in detail for the better resolved DASSA data, representing an independent conformation of the equilibrium shift to the higher temperatures, compared to the bulk transition at –25 °C.

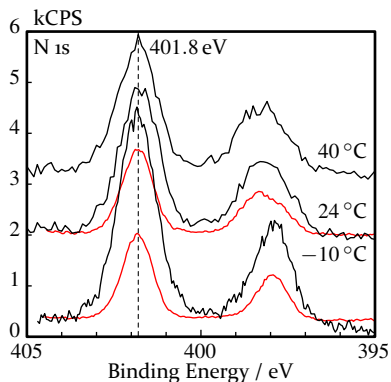


Figure 1.8.: Comparison of normal emission N 1s regions of **IL-3**, measured at 40 °C, 24 °C, and –10 °C, in both the ESCA (black) and DASSA (red) chambers.

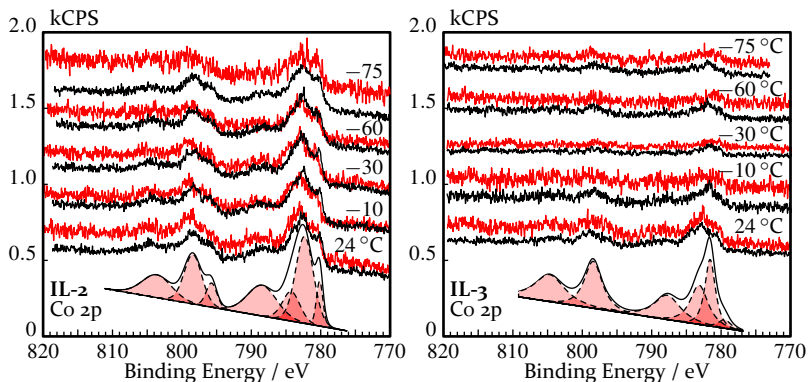


Figure 1.9.: Normal emission (black) and 80° (red, scaled by imidazolium peak area) Co 2p spectra of **IL-2** (left) and **IL-3** (right) at several temperatures. The peak fitting model used to fit the corresponding $-10\text{ }^{\circ}\text{C}$ spectra is also show.

1.3.5 XP Spectra of the Cobalt 2p Core Level

Additional information on the transformation from the tetrahedral to the octahedral cobalt complex can be deduced from the Co 2p regions of **IL-2** and **IL-3**. Figure 1.9 shows the Co 2p spectra of the two cobalt containing ILs. At $24\text{ }^{\circ}\text{C}$, both ILs exhibit spectra of identical shape, with the Co $2p_{1/2}$ branch between 810–795 eV, and the Co $2p_{3/2}$ branch between 795–778 eV; as expected for open-shell Co(II) systems, both branches exhibit multiplet splitting. At $24\text{ }^{\circ}\text{C}$, the lower intensity (by $\sim 40\%$) for **IL-3** is due to the lower cobalt density in the mixture, as compared to **IL-2**.

Whereas **IL-2** does not reveal any changes during cooling, the Co 2p spectral shape of the thermochromatic IL is considerably altered at lower temperatures (see figure 1.9): Whereas at room temperature the Co $2p_{1/2}$ branch of the thermochromatic IL shows one shoulder next to the peak maximum and the Co $2p_{3/2}$ branch shows two shoulders around the peak maximum, the intensity of these shoulders is considerably decreased at $-10\text{ }^{\circ}\text{C}$. This change can most easily be quantified by differential shifts of the maxima in the $2p_{1/2}$ and $2p_{3/2}$ branches by about -0.6 eV and -1.1 eV to lower binding energy, respectively; the difference in shape is more evident in figure 1.10, where the scaled and averaged $-10\text{ }^{\circ}\text{C}$ and $-30\text{ }^{\circ}\text{C}$ spectra are plotted together for direct comparison with the $24\text{ }^{\circ}\text{C}$. The change in apparent spin-orbit splitting an

in overall spectral shape both clearly indicate a change in the complex structure. Because no further spectral changes occur when cooling **IL-3** to $-30\text{ }^{\circ}\text{C}$ and below (figure 1.9), and with film of **IL-3** being fully red at these temperatures, the $-10\text{ }^{\circ}\text{C}$ spectrum shown in figure 1.9 is attributed to the octahedral $[\text{Co}^{\text{II}}(\text{NCS})_6]^{4-}$ complex being predominately present in the near-surface region probed by XPS in normal emission. The observed overall Co 2p shift toward lower binding energies is thus attributed to the increase in the number of negatively charged $[\text{SCN}]^-$ ligands (from 4 to 6) around the Co^{II} core, accompanied by a change in electron redistribution;³³ a reduction to Co^{I} is extremely unlikely because Co^{I} complexes typically can only be stabilised using multidentate or highly protective ligands,³⁸ which is not the case for thiocyanate.

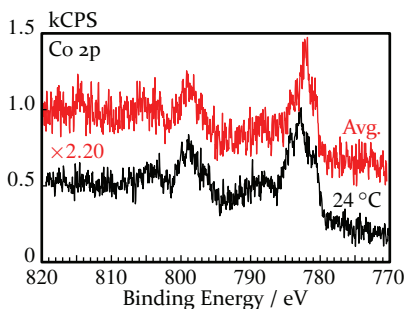


Figure 1.10.: Normal emission spectra of **IL-3** at $24\text{ }^{\circ}\text{C}$ (black) and an average of the $-10\text{ }^{\circ}\text{C}$ and $-30\text{ }^{\circ}\text{C}$ spectra (red).

in density of the Co complex in the near-surface region contributing to the XPS signal. One possible explanation is that in order to be stabilised at temperatures above the bulk transition temperature, the four times negatively charged octahedral $[\text{Co}^{\text{II}}(\text{NCS})_6]^{4-}$ complex with its four imidazolium counter-cations is solvated by additional $[\text{SCN}]^-$ anions. This extended solvation shell configuration would lead to an excess of $[\text{SCN}]^-$ anions (including the corresponding cations) weakly bound to the octahedral complex in the near surface region. A solvation shell with, for example, 8 to 10 weakly bound $[\text{SCN}]^-$ anions (instead of only one as expected from the stoichiometry of a $[\text{C}_4\text{C}_1\text{Im}]_4^+[\text{Co}^{\text{II}}(\text{NCS})_6]^{4-}/[\text{C}_2\text{C}_1\text{Im}]^+[\text{SCN}]^-$ 1 : 1 mixture), would be consistent with the pronounced decrease in the Co 2p signal. The nar-

In addition to the change of shape of the Co 2p spectra of **IL-3**, also observed is a pronounced decrease in the overall Co 2p signal upon cooling (figure 1.9) to $\sim 40\%$ of the original signal at $24\text{ }^{\circ}\text{C}$ (overall intensity, as derived by numerical integration from 770–815 eV after linear background subtraction). Beam damage effects can be ruled out because heating from $-10\text{ }^{\circ}\text{C}$ back to room temperature fully restores the original Co 2p intensity (not shown). The lower Co 2p intensity indicates a decrease

row line widths of the anionic N 1s and S 2p peaks in figure 1.6 at -10°C furthermore indicate that the N 1s and S 2p binding energies for the $[\text{Co}^{\text{II}}(\text{NCS})_6]^{4-}$ and free $[\text{SCN}]^-$ anions (that is, the neat thiocyanate) are very similar. The proposed core-shell structure would also explain why, in contrast with the neat thiocyanate, no pronounced surface orientation of free $[\text{SCN}]^-$ anions is observed below 4°C : because only $[\text{SCN}]^-$ anions weakly bound to the octahedral complex are present in the near-surface region.

1.4 A Thermodynamics Based Explanation for the Near-Surface Behaviour

I propose that the reason for the $\sim 30^\circ\text{C}$ difference between the bulk and near-surface transition temperatures is, in a thermodynamic sense, related to the higher degree of order in the near-surface region of **IL-3** compared to the bulk. In the bulk and in the near-surface region, the forward reaction of the equilibrium $[\text{Co}^{\text{II}}(\text{NCS})_4]^{2-} + 2 [\text{SCN}]^- \rightleftharpoons [\text{Co}^{\text{II}}(\text{NCS})_6]^{4-}$ generally leads to a decrease in entropy (that is, the reaction entropy $\Delta_r S^\ominus$) due to the loss of two free $[\text{SCN}]^-$. From the observed equilibrium shift to the right with decreasing temperature, it can be deduced that the reaction enthalpy, $\Delta_r H^\ominus$, is also negative. From the Gibbs-Helmholtz equation ($\Delta_r G^\ominus = \Delta_r H^\ominus - T \cdot \Delta_r S^\ominus$), the temperature at which a reaction becomes favourable (i. e. $\Delta_r G^\ominus \leq 0$, and consequently the equilibrium constant k becomes > 1) is given by:

$$T_{\text{trans.}} = \frac{\Delta_r H^\ominus}{\Delta_r S^\ominus} \quad (1.1)$$

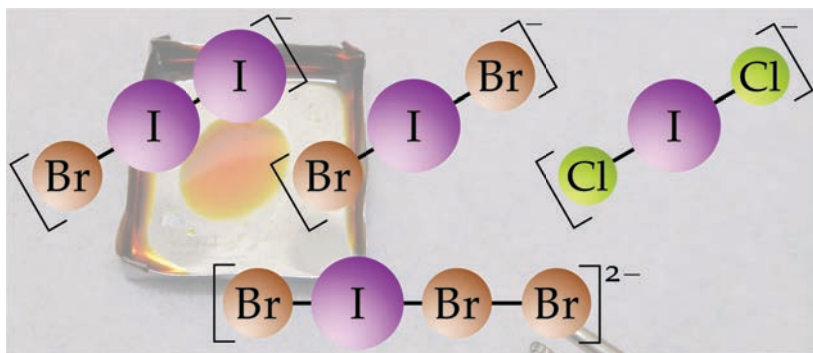
Thus, if in the near-surface region ΔH is more negative or ΔS is less negative, one would expect a transition temperature increase in the near-surface region. There is no reason to assume that the reaction enthalpy is significantly different in the near-surface region compared to the bulk. The magnitude of the reactions' entropy change is, however, quite likely to be significantly different in the bulk and in the near-surface region. It has been shown that at the surface of **IL-3** at room temperature the free thiocyanate ions are preferentially oriented (such ordering extending several molecular layers into the bulk is consistent with previously published results^{36,37}) – that anisotropy means that the forward complexation reaction starts from a 'semi-ordered' state in the near-surface region, which implies that $\Delta_r S_{\text{surface}}^\ominus > \Delta_r S_{\text{bulk}}^\ominus$ (bearing in

mind that both values are negative). Within this thermodynamic picture, $\Delta_r G_{\text{surface}}^{\ominus}$ is always more negative than $\Delta_r G_{\text{bulk}}^{\ominus}$ at any given temperature, leading to $T_{\text{trans., surf.}} > T_{\text{trans., bulk}}$, as was experimentally observed.

1.5 Conclusion

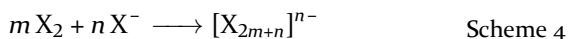
In conclusion, the observed temperature-dependent changes for **IL-3** indicate that a transition from tetrahedrally-coordinated toward octahedrally-coordinated cobalt(II) occurs in the near-surface region at 4 °C, that is, at a temperature ~ 30 °C higher than in the bulk. This higher transition temperature is attributed to a lower entropic barrier – at the semi-ordered surface observed here, the formation of the $[\text{Co}^{\text{II}}(\text{NCS})_6]^{4-}$ anion is a semi-ordered \rightarrow ordered transition, rather than the disordered \rightarrow ordered transition of the bulk. Without support from theory this explanation is only speculation, however it is consistent with the observations reported here. The transition goes along with a pronounced decrease in the density of the complex in the near-surface region – an effective dilution of the complex. This is attributed to the formation of a weakly bound $[\text{SCN}]^-$ secondary solvation shell around the $[\text{Co}(\text{NCS})_6]^{4-}$ anion, with a primary solvation shell of four cations, which leads to an effective dilution of the complex. It is important to note that such surface-induced phenomena could be highly relevant for all concepts where high surface area materials are applied. While such effects are very difficult to discern using bulk analytic methods, this study has demonstrated that for ionic liquid based systems surface-sensitive XPS allows for the study of such changes in detail.

2 XPS of Four Polyhalide Anion Ionic Liquids, and Their Vacuum and Thermal Stability



2.1 Introduction

Polyhalide anions have a long history, but have recently been an active area of interest. In general, polyhalide anions require both halides and neutral halogens, which can then react as follows:



There is a tendency of polyhalides to lose a neutral halogen species to the gas phase, a tendency which decreases as the proportion of halide increases (in terms of scheme 4, less loss of neutral halogen occurs with increasing n/m ratio)³⁹ New synthesis techniques have allowed the number of known polyhalide anions (particularly those of the lighter halides) to expand, and open up several interesting potential applications.³⁹

Some of the new polyhalide synthesis methods and applications depend on the properties of ionic liquids (ILs)^{39,40} The low volatility of ILs is also useful, because it means that they can be subjected to ultra-high vacuum (UHV) conditions – as a consequence, they can be studied by a number of UHV techniques such as X-ray photoelectron spectroscopy (XPS) and vaporous phase mass spectrometry (MS). Men *et al.*⁴¹ have already published an XPS study of two trihalide ionic liquids, with the anions $[\text{Br}_2\text{I}]^-$ and $[\text{I}_3]^-$. They found that the two trihalides studied were both weaker bases than the neat halides Br^- and I^- , and that the trihalide anions had a delocalised electronic structure, with the negative charge shared across the three atoms.

The basicity of an ionic liquid's anion can be determined by several methods – NMR,¹⁸ XPS,^{18,42,43} and the more conventional solvatochromic dyes. These three techniques all probe different, but related, properties: the solvatochromic method probes hydrogen bond acceptance (that is, the Kamlet-Taft β values), NMR probes the interaction strength of the C2-position proton with the anion specifically,¹⁸ and XPS probes the overall degree of charge transfer between the anion and the cation.^{18,44} These three parameters all correlate with overall anion basicity, meaning that one can order ionic solvents according to their anion basicity without without relying on a solvatochromic technique. This is useful if (as is typically the case with polyhalide ILs) the IL has a very intense colouration, and this has been exploited in previous XPS studies of trihalide ILs.⁴¹

For some time now, tribromide salts have been used in organic synthesis as convenient bromination agents.⁴⁵ More recently, tribromide- and trichloride-containing salts, including ionic liquids, have been shown to be not only easier to handle than the base halogens, but also to exhibit other useful properties such as enhanced reactivity and higher yields.^{46–48} Ionic liquid-based polyhalides thus have great potential as 'green' halogenation reagents, due to the extremely low volatility of ionic liquids. They also exhibit stereo-⁴⁹ and regioselectivity,⁸ and the reuseability of some of these agents has been shown.^{8,49,50}

Trihalides and ionic liquids are also used in dye-sensitised solar cells (DSSCs). The classic DSSC uses a $[\text{I}_3]^-/\text{I}^-$ redox couple,^{51–53} and there has been recent interest in $[\text{Br}_3]^-/\text{Br}^-$ based redox couples.⁵⁴ Polyhalide ionic liquids are of interest as components of both liquid and quasi-solid electrolytes.⁷ Understanding the behaviour of polyhalide species in ionic

liquids is therefore an important step in optimising redox couple/electrolyte chemistry.

In this study, the speciation of several polyhalide ionic liquids are investigated by XPS, and their vacuum and thermal stability are also investigated. These investigation will be the basis for understanding the corrosive behaviour of one of these polyhalide ILs towards the group II metals in the next chapter.

2.2 Methods and Materials

2.2.1 Ionic Liquid Synthesis

Three trihalide ionic liquids, $[\text{C}_6\text{C}_1\text{Im}][\text{BrI}_2]$ (**IL-1**), $[\text{C}_6\text{C}_1\text{Im}][\text{Br}_2\text{I}]$ (**IL-2**) and $[\text{C}_6\text{C}_1\text{Im}][\text{Cl}_2\text{I}]$ (**IL-3**), were prepared by mixing a 1-hexyl-3-methyl-imidazolium halide (chloride >99 %, bromide 99 % and iodide >98 %, all purchased from IoLiTec and used without further processing) with either iodine monochloride (ICl, Merck, $\geq 98\%$) or iodine monobromide (IBr, Sigma-Aldrich, 98 %), in a 1 : 1 molar ratio and stirring thoroughly. The polyhalide $[\text{C}_6\text{C}_1\text{Im}]_2[\text{Br}_3\text{I}]$ (**IL-4**), with one molar excess of Br^- , was made in the same way as the trihalide ILs, except the $[\text{C}_6\text{C}_1\text{Im}]\text{Br} : \text{IBr}$ ratio was 2 : 1.

For all three trihalides, the interhalogens rapidly dissolved to form a deep red-brown liquid that was significantly less viscous than the starting halides. $[\text{C}_6\text{C}_1\text{Im}][\text{Cl}_2\text{I}]$ showed a green tint, in addition to its red-brown colour. To prevent any potential photodegradation, exposure to light was minimised throughout all experiments, and the ILs were stored in sealed glass vessels wrapped in aluminium foil.

2.2.2 XPS Analysis

XP spectra were taken of all three trihalides and the dibromodiiodide-based **IL-4**. The samples scanned were prepared by placing several drops of the IL on a molybdenum sample plate, pre-degassing the sample for 24 h at *ca.* 5×10^{-7} mbar in a separate chamber, then transferring the sample to the XP spectrometer chamber (base pressure 1×10^{-10} mbar). Molybdenum was used because it is resistant to corrosion by trihalide ionic liquids, as will be discussed in the following chapter.

To follow progressive loss of volatile halogen species under vacuum, a sample of **IL-2** was introduced to the ESCA chamber, pumped down

overnight, and then analysed intermittently over the course of three days by XPS.

For XPS measurements, the radiation used was non-monochromated Al K_{α} from a SPECS XR 50 X-ray gun, operating at 12.0 kV and 20 mA. The electron analyser used was a VG Scienta R3000, set to a pass energy of 200 eV for wide scans, and 100 eV for detailed region scans. All spectra were taken in normal emission geometry for maximum bulk sensitivity (information depth 7–9 nm depending on kinetic energy^{13,14}). Grazing emission spectra were not possible because of the tendency of the ILs studied to run off the sample holder and drip into the chamber. Data were analysed in CasaXPS. Peaks were fitted with a pseudo-Voigt profile with a 30% Lorentzian contribution (80% for I 3d), and for spin-orbit split peaks the two fitted components were constrained to have equal full width at half maxima and the expected peak area ratio (e. g. 2 : 3 for $d_{3/2} : d_{5/2}$). For all peaks, a Shirley background was used, except for the I 3d peak of ILs **2**, **3** and **4**, where a W-Tougaard background was used. The C 1s peak was fitted with two components, C_{alkyl} at lower binding energy, and C_{hetero} at higher binding energy. The C_{hetero} component was constrained to have a full width at half maxima 1.1 larger than that of the C_{alkyl} component. All spectra were charge-corrected by the C_{alkyl} peak at 284.8 eV.

2.2.3 Mass Spectrometry

Vapour phase mass spectrometry was carried out in a separate, smaller chamber (base pressure 5×10^{-8} mbar), equipped with a Hiden HAL 511 3F mass spectrometer, mass range 2–350 amu. For vapour phase measurements, several drops of the **IL-2**, and in a separate experiment **IL-4**, were put in a molybdenum sample box, made of a single sheet folded into a shallow tray, which was then placed onto the chamber's copper sample head, which was then inserted into the chamber. The copper sample head could be water cooled and heated by a resistive element. Since trihalide ILs react readily with copper, the molybdenum sample tray was checked for leaks before the IL was added, and care was taken to prevent spills. For both MS and XPS measurements, the sample holders used were sonicated in acetone for half an hour, then dried in an oven, before use.

2.3 XPS Results

The relevant XP spectra of the four ILs are presented in figures 2.1 and 2.2 (cation and oxygen regions, and halogen regions, respectively). For comparison, the spectra of the monohalide ILs ($[C_6C_1Im]X$, $X = Cl, Br, I$) used to synthesis **IL-1–IL-4** are also shown. The composition of each IL, as derived from these XPS measurements, is presented in table 2.1; all atomic numbers are normalised to the two nitrogen atoms of the imidazolium cation. No contamination by other halogens could be detected, however there is an excess of alkyl carbon and a significant amount of oxygen contamination. Aside from the $I\ 3d_{5/2}$ core level of **IL-2**, there is little change in the composition over 70 h. The spectra in figure 2.3 show a decrease in $I\ 3d$ intensity that appears to occur mostly between the 13 h scan and the 46 h scan. Otherwise, no significant shifts over the 70 h period occur.

With respect to composition, some alkyl contamination was present in all ILs, with **IL-1** and **IL-2** exhibiting the highest, and **IL-3** and **IL-4** the lowest level of excess alkyl carbon. All polyhalide samples also showed a significant amount of oxygen, up to 1.4 oxygen atoms per imidazolium cation (see table 2.1), which somewhat correlates with the excess of alkyl carbon. Since there is no sign of silicon in the wide scans of any of the ILs, ruling out considerable amounts of surface-enriched polysiloxane contamination that often show up in XPS of IL systems;⁴ the origin of the O 1s signal is not clear yet.

The quantification given in table 2.1 reveals that the amount of bromine is generally close to the expected value, except for **IL-1**, where the amount of bromine is significantly greater than expected. It is notable that all of the bromine containing polyhalide ILs have a bromine peak with a small shake-up peak at around 74.5 eV, which is absent for the monohalide IL. This shake-up peak was included in the quantification. The Cl 2p region used in the quantification of **IL-3** was not wide enough to include the presumably present shake-up feature, figure 2.2. This may explain why the amount of chlorine reported in table 2.1 is lower than expected.

The amount of iodine reported for all the ILs in table 2.1 is lower than expected for all ILs. Examining the spectra, figure 2.2, a small shake-up feature can be seen 4.9–5.2 eV above the main peak. This feature is included in the quantification. The quantification of **IL-2** (after 13 h under vacuum), **IL-3**, and **IL-4** show an amount of iodine is closest to

the expected amount, but **IL-1** shows the most pronounced reduction in iodine indicating an actual loss from the IL into the vacuum. As it will be shown later when discussing the possible speciation of halides in the ILs, the trihalide anion $[\text{BrI}_2]^-$ seems to release most of its iodine in the form of I_2 ; the remainder is bound to bromide, most likely in the form of $[\text{Br}_2\text{I}]^-$ and $[\text{BrI}_2]^-$ co-present with free Br^- .

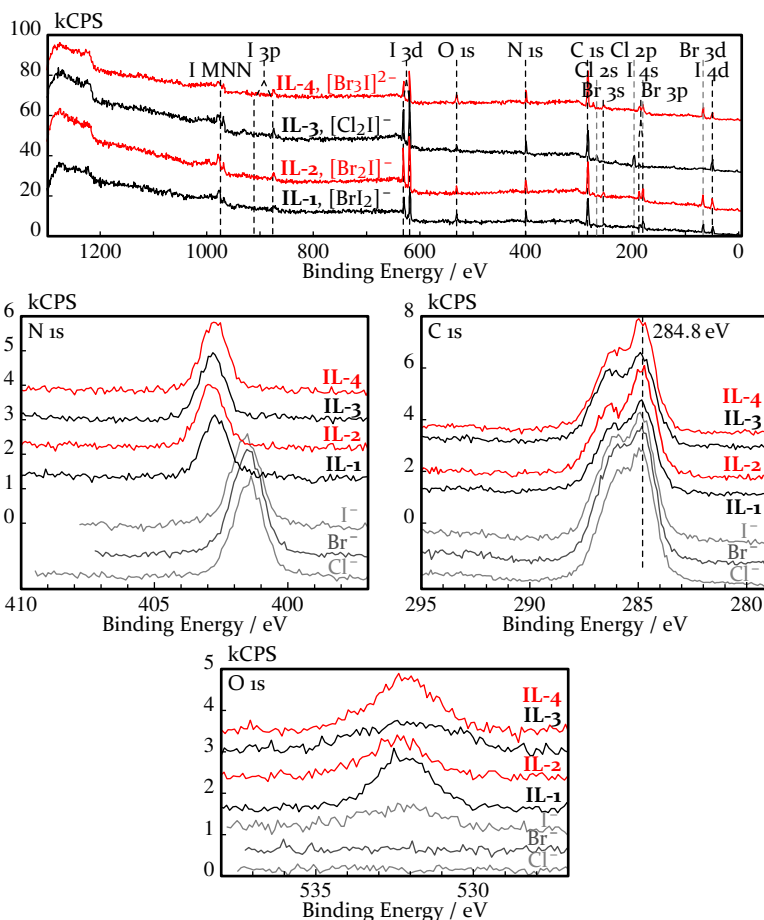


Figure 2.1. Survey and imidazolium-region spectra of the four ILs studied – spectra of **IL-2** correspond to the 13 h spectra in figure 2.3. Neat halide spectra are also presented, in grey. All spectra were charge corrected to $C_{\text{alkyl}} = 284.8$ eV.

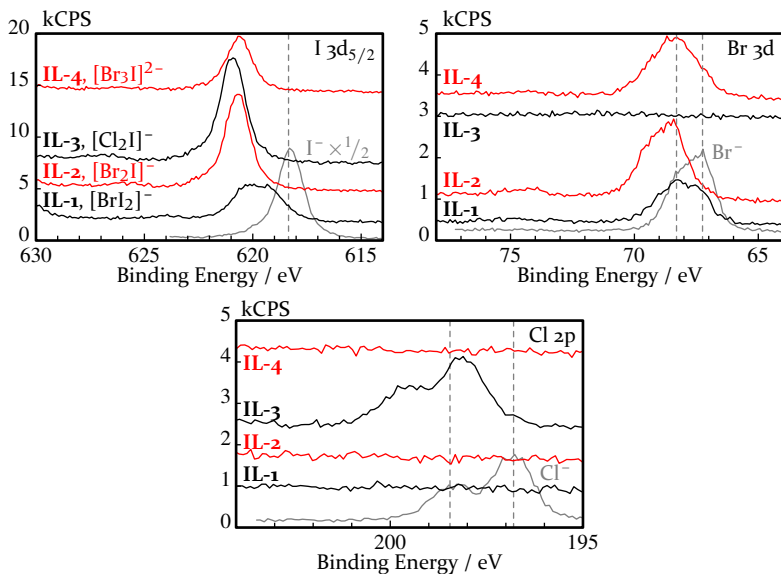


Figure 2.2.: Halogen regions of the four ILs studied, with corresponding neat halide peak (grey) – spectra of IL-2 correspond to the 13 h spectra in figure 2.3.

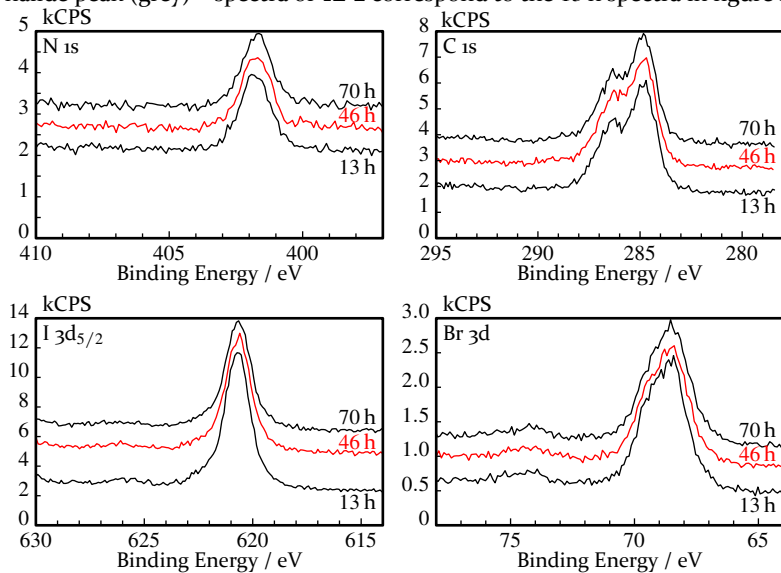


Figure 2.3.: Time dependant region spectra of IL-2 ($[\text{Br}_2\text{I}]^-$) after 13 h, 46 h and 70 h under vacuum.

RSF →	C 1s		O 1s	N 1s	I 3d _{5/2}	Br 3d	Cl 2p	Anion
	alkyl	hetero						
	0.208	0.599	0.364	5.740	0.551	0.573	<i>nominal</i>	
Chloride	10.8	5.9 : 4.9	0	≅2	0	0	1.0	Cl ⁻
Bromide	10.1	5.4 : 4.7	0	≅2	—	1.0	—	Br ⁻
Iodide	10.7	5.8 : 4.9	0.5	≅2	0.9	—	—	I ⁻
IL-1*	12.9	7.3 : 5.6	1.4	≅2	0.5	1.3	0	[BrI ₂] ⁻
<i>nominal</i>	10	5 : 5	0	2	2	1	0	
IL-2 13h	13.5	8.1 : 5.4	1.1	≅2	0.8	1.9	0	[Br ₂ I] ⁻
IL-2 46h	13.8	8.2 : 5.6	1.6	≅2	0.6	1.8	0	
IL-2 70h	13.7	8.3 : 5.4	1.4	≅2	0.6	1.8	0	
<i>nominal</i>	10	5 : 5	0	2	1	2	0	
IL-3*	11.5	6.2 : 5.3	1.0	≅2	0.8	0	1.6	[Cl ₂ I] ⁻
<i>nominal</i>	10	5 : 5	0	2	1	0	2	
IL-4*	11.9	6.8 : 5.1	1.1	≅2	0.4	1.4	0	[Br ₃ I] ²⁻
<i>nominal</i>	10	5 : 5	0	2	0.5	1.5	0	

Table 2.1.: Composition of the trihalide and neat halide ILs, as measured in the ESCA. *Sample was degassed for 24 h before measurement.

2.3.1 XPS Binding Energy Shifts and Polyhalide Lewis Basicity

The spectra presented in figure 2.2 clearly show that the anion signals are all shifted to higher binding energies with respect to the corresponding monohalide – this will be discussed in terms of charge delocalisation in detail in the next section. These charge-delocalised polyhalide anions are expected to coordinate differently to the imidazolium head-groups than the monohalide anions, leading to XPS shifts in the N 1s and C_{hetero} signals of the cationic ring.¹⁸

The comparison of the C_{alkyl}-C_{hetero} peak separation of the trihalides with the neat halides in table 2.2, shows a shift to higher binding energy of 0.1–0.3 eV. Notably, the shift is greatest for **IL-2** and **IL-3**. The N 1s shifts are also on the order of 0.1–0.3 eV, again the shift is greatest for **IL-2** and **IL-3**. Shifts in C_{hetero} and imidazolium N 1s peak positions are known to correlate with anion basicity and Kamlet-Taft hydrogen bond acceptor ability (β value)^{18,42,43} – larger shifts indicate a lower basicity (that is, a lower β value). In the case of **IL-2**, both the C_{alkyl} and imidazolium N 1s shifts are the same (within reasonable uncertainty) to those of [C₈C₁Im][Br₂I] as reported by Men et al.⁴¹ In the case of both **IL-2** and **IL-3** the clear implication is that the [Br₂I]⁻ and [Cl₂I]⁻ anions are less basic than the corresponding mono-halides. In the case of **IL-1** and **IL-4**, the apparent basicity is between those of the trihalide

IL	Anion	Binding Energy / eV				
		C _{hetero}	N 1s	Cl 2p _{3/2}	Br 3d _{5/2}	I 3d _{5/2}
	Cl ⁻	286.2	401.5	196.8	—	—
	Br ⁻	286.3	401.5	—	67.2	—
	I ⁻	286.3	401.6	—	—	618.3
1	[BrI ₂] ⁻	286.4	401.6	—	67.3, 68.3*	619.2, 620.4
2	[Br ₂ I] ⁻	286.5	401.8	—	68.3	620.7
3	[Cl ₂ I] ⁻	286.5	401.7	198.1	—	620.9
4	[Br ₃ I] ²⁻	286.4	401.6	—	67.7, 68.4*	620.6

Table 2.2.: C_{hetero} peak position, N 1s peak positions, and halogen peak positions of the trihalide and neat halide ILs. *See text for details.

and the halides – the implication is that either the degree of charge delocalisation is not as great as for the two trihalides, leading to a greater degree of charge transfer, or more likely a mixture of poly- and weakly-coordinated-monohalide anions is present in both ILs. As is evident from figure 2.2, and will be discussed next, **IL-1** exhibits two components in the I $3d_{5/2}$ and in the Br $3d$ region while **IL-4** shows a broadening in these regions.

2.3.2 Halogen Speciation

The spectra of all four trihalide ILs (figure 2.2) show halogen peaks significantly shifted from the monohalides – these shifts are quantified in table 2.2. The shifts of the two halogen signals of **IL-2** compared to the mono-bromide and mono-iodide are +1.2 eV and +2.4 eV respectively. These values match those previously reported for $[\text{C}_8\text{C}_1\text{Im}][\text{Br}_2\text{I}]$ by Men et al.⁴¹ – who attributed these shifts to delocalisation of the negative charge over all three halogen atoms. Delocalisation would also tend to introduce shake-up features – these can be seen in both the I $3d_{5/2}$ and the Br $3d$ spectra, figure 2.2. The positions of the Br $3d$ shake-up feature (74.4 eV) and the I $3d_{5/2}$ shake-up feature (625.7 eV) match those reported by Men et al.⁴¹ Most significantly, XPS shows only one I $3d_{5/2}$ peak and one spin-orbit split Br $3d$ doublet. The full width at half maximum of the iodine peak is virtually identically (within 0.1 eV) to that of the corresponding monohalide peaks and the full width at half maximum of the bromine peak is only 0.2 eV wider than that of the monohalide), hence the chemical environments of the each halide atom within the trihalide anion must be very uniform. For **IL-2**, our results thus confirm the anion speciation proposed by Men et al.⁴¹ for $[\text{C}_8\text{C}_1\text{Im}][\text{Br}_2\text{I}]$, with iodine located in the centre of a linear anion complex between two bromides: $[\text{Br}-\text{I}-\text{Br}]^-$.

A similar conclusion can be drawn for **IL-3**. From the data in table 2.2, it can be seen that the Cl $2p_{3/2}$ peak has shifted to higher binding energy by +1.3 eV compared to the mono-chloride, and that the single I $3d_{5/2}$ peak has shifted by 2.6 eV – similar to the shifts of the corresponding halogen peaks reported above for **IL-2**. No shake-up peak is visible in the Cl $2p$ detailed spectra (figure 2.2), however this is likely because the scan window was not wide enough. A small shake-up peak is seen in the I $3d_{5/2}$ detailed scan, at 626.8 eV, which is a larger peak-to-shake-up separation than the one observed for $[\text{Br}_2\text{I}]^-$. As with **IL-2**, the I $3d_{5/2}$ and Cl $2p$ region spectra of **IL-3** show a single (spin-orbit

split in the case of Cl 2p) peak with a full width at half maximum virtually identical to that of the monohalide ($I\ 3d_{5/2}$ difference <0.1 eV, Cl 2p difference 0.1 eV). Therefore, the chemical environments of each halide atom must be very uniform, as with **IL-2**. From these observations, it is concluded that the anion present is the dichloro- analogue of the charge-delocalised anion present in **IL-2** – namely, $[Cl-I-Cl]^-$.

Both the dibromiodide and dichloriodide anions are known and have been studied by X-ray crystallography¹⁶ – $[Br-I-Br]^-$ as the caesium salt, and $[Cl-I-Cl]^-$ as quaternary ammonium, piperazinium and triethylenediamine salts. In general, the bond lengths (including symmetry) and the bond angles of these polyhalide anions are dependent on the cation present.^{16,17}

Identifying the polyhalide species present in **IL-4** is more difficult. By nominal composition, two species are present, the $[Br_2I]^-$ anion and the monohalide Br^- . However given the ability of polyhalide species to form more complex higher-order species, it is more likely that the excess mono-halide is involved in the formation of one or more polyhalide species, which is expected to lead to a superposition of more than two shifted bromide components in XPS. The $I\ 3d_{5/2}$ peak of **IL-4** is virtually (within 0.1 eV) as wide as that observed in the case of **IL-2**, while the peak maxima are very close in binding energy position (table 2.2). The shake-up structure seen at 625.9 eV (figure 2.2) indicates that charge delocalisation is also present for the iodine in **IL-4** (note that the shake-up structure is very small due to the lower overall iodine content of **IL-4** compared to the other trihalide ILs). The implication of this is that iodine is in one, delocalised, electronic environment, albeit one that is slightly different to that probed in **IL-2**. The shift of the Br 3d doublet is on the order of that observed for **IL-2**, however quantifying peak positions is somewhat more difficult. An assumptive fitting can be made with two doublets, constrained by a fixed spin-orbit-splitting of 1.05 eV, as measured for the monobromide IL, for **IL-2** and

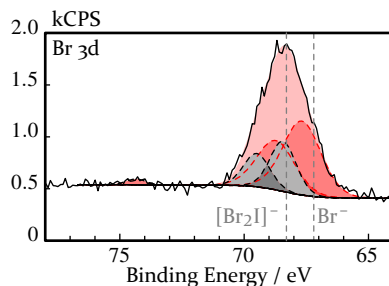


Figure 2.4.: Br 3d region of **IL-4** ($[Br_3I]^{2-}$), with two component doublets and a shake-up peak fitted. The Br $3d_{5/2}$ peak position of the neat bromide and **IL-2** are indicated.

bromine compounds in general⁵⁵ – figure 2.4. If this is done, the Br $3d_{5/2}$ components of the two doublets reside at 67.7 eV and 68.4 eV, the latter being close to the position observed for **IL-2** and the former is not far from the monobromide position. Note that the spin-orbit-split doublet seen at the lower binding energy is considerably broader and larger in intensity than the other doublet.

For **IL-4**, it is tempting to speculate that a linear anionic species such as $[\text{Br}-\text{I}-\text{Br}-\text{Br}]^{2-}$ is formed, with the two Br side atoms being relatively close to the monobromide with respect to electronic structure. In terms of distributing the two negative excess charges over this proposed linear structure of the dianion, our XPS results would be consistent with the greatly simplified picture $[\text{Br}^{0.3-}-\text{I}^{0.3-}-\text{Br}^{0.7-}-\text{Br}^{0.7-}]$, instead of a more or less equal charge distribution of $[\text{Br}^{0.5-}-\text{I}^{0.5-}-\text{Br}^{0.5-}-\text{Br}^{0.5-}]$. Although polyhalide monoanions tend to form primarily with an odd number of halogen atoms,¹⁶ even numbered linear dianion species such as $[\text{I}_4]^{2-}$ and $[\text{Br}_8]^{2-}$ are also known.^{17,39} The existence of larger polyhalide anions, perhaps even an extended polymeric system, cannot be ruled out – similar extended polybromide systems have been reported previously in ionic liquids.^{39,40} Without support from theory or other experimental techniques, such as far-infrared spectroscopy or crystallography, the speciation cannot be definitively identified, but the likely speciation is as $[\text{Br}_3\text{I}]^{2-}$.

The species nominally present in **IL-1** is $[\text{I}-\text{I}-\text{Br}]^-$, which is known from X-ray crystallography.¹⁶ However, the loss of approximately 75% of the iodine signal, as noted above in table 2.1, makes this speciation on its own impossible. Apparently, this trihalide anion is relatively unstable

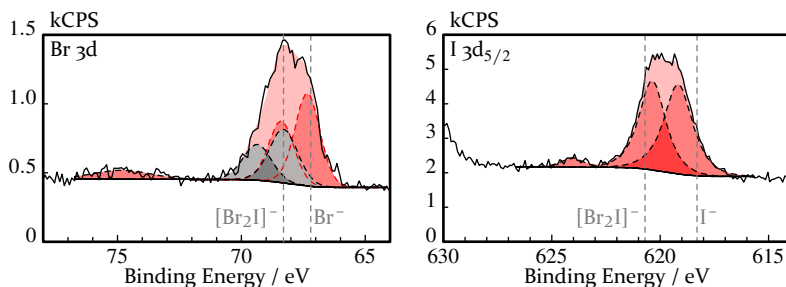


Figure 2.5: Br $3d$ and I $3d_{5/2}$ region of **IL-1** ($[\text{Br}_2\text{I}]^-$), with two components and a shake-up peak fitted. The Br $3d_{5/2}$ and I $3d_{5/2}$ peak positions of the neat halides and of **IL-2** are given.

under vacuum conditions. Most likely, molecular iodine is pumped away. From the remaining iodine content of **IL-1** (table 2.1), an overall I : Br ratio of 1 : 2.6 can be derived by XPS. In comparison with the spectra of **IL-2**, the presence of iodine in two chemical environments in **IL-1** is evidenced by the two I $3d_{5/2}$ components shown in figure 2.2, and more clearly in figure 2.5. Also, a small shake-up structure at around 624.0 eV can be seen, figure 2.5. The higher BE peak is at 620.4 eV, a position similar to that recorded for **IL-2** (620.7 eV, table 2.2). Based on the relative peak areas (not including the shake-up), the two species are present in a 1.0 : 1.0 ratio – which fits with the anion $[I-I-Br]^-$ being present, with the central iodine atom being in a similarly reduced state to that in **IL-2**, whereas the outer iodine is more negatively charged (that is, closer to I^-). However, as noted above, the overall stoichiometry does not fit with $[I-I-Br]^-$ as the sole anion – the implication is that there isn't only a single trihalide anion present, and there may be free I^- present.

Fitting the Br $3d$ spectrum with a similar two doublet model to that applied to **IL-4** gives a reasonable fit, with the positions of the fitted Br $3d_{5/2}$ peaks at 67.3 eV and 68.3 eV, table 2.2. The position of the lower binding energy peak is very close to that of the monobromide, while the higher binding energy peak is at a position similar to that noted for **IL-2**; the two species (seen at lower and higher binding energy) are present in a 1.5 : 1 ratio, respectively. The implication is most of the bromine is present as the mono-halide, and a smaller amount is present as some form of delocalised species, in combination with the iodine. It appears that this IL contains a mixture of $[Br_2I]^-$, Br^- , and I^- , but as with **IL-4**, determining the actual speciation requires either theory or other experimental techniques – it should be born in mind that the loss of iodine, and to a lesser extent bromine, likely occurs during pump-down.

2.4 Mass Spectrometry Results

The mass spectra recorded are presented in figure 2.6, along with a background spectra of the chamber. The mass spectra recorded at room temperature for both ILs show no significant release of iodine or bromine above background levels. When **IL-2** is heated to 40 °C, a large increase in the I^+ mass signal (at 127 amu) is observed. This release is not accompanied by an increase in the bromine mass peaks. For **IL-4** only

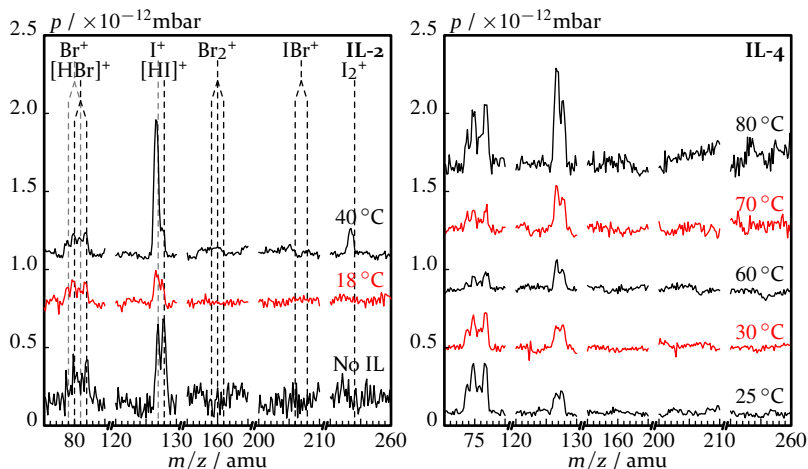


Figure 2.6.: Mass spectra of **IL-2** ($[\text{Br}_2\text{I}]^-$), and **IL-4** ($[\text{Br}_3\text{I}]^{2-}$) in a molybdenum pan at several temperatures. A spectrum of the empty chamber at room temperature (labelled No IL) is also included.

a minor increase of the I^+ signal is observed up to 60°C , showing an increase in stabilisation due to excess bromide. A significant increase in I^+ and $[\text{I}_2]^+$ can only be clearly detected at 80°C , whereas no $[\text{HBr}]^+$ or $[\text{Br}_2]^+$ mass peaks can be seen at any temperature.

For iodine, the most prominent peak in a mass spectrum is the I^+ mass signal, which is approximately $100\times$ larger than the $[\text{I}_2]^+$ signal.⁵⁶ The $[\text{I}_2]^+$ mass peak is seen for **IL-2** at 40°C , and for **IL-4** at 80°C . For bromine, the most prominent peaks are those associated with the $[\text{Br}_2]^+$ mass peaks, which are approximately $10\times$ as intense as the Br^+ peaks⁵⁷ – it is notable that in the background and the **IL-4** 80°C spectra, no $[\text{Br}_2]^+$ mass peaks can be seen. It is known that IBr can be detected as $[\text{IBr}]^+$, although the cracking pattern is uncertain due to the decomposition of IBr before it can enter the spectrometer.⁵⁸ The implication is that Br_2 and IBr are not being released, and the bromine seen in the mass spectra at around 80 amu is likely due to previous contamination of the copper sample head. For both ILs, it can be concluded that heating caused the release of iodine, but not bromine. The loss of iodine can be understood thermodynamically as a consequence of the stability of the bromide anion versus the iodide anion. It is known that in general bromine (Br_2) will oxidise iodide (I^-), to form bromide (Br^-) and iod-

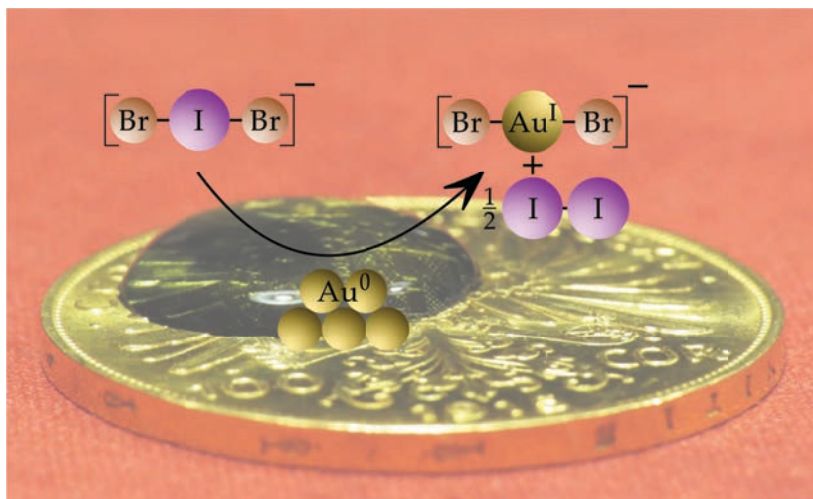
ine (I_2),⁶ so it is not unexpected that iodine is the preferred product of the decomposition of the trihalide $[Br_2I]^-$. Mechanistically, the interconversion of polyhalide species has been reported in both aqueous and polar organic solution⁵⁹ – such interconversion likely exists in ionic liquid solution as well, and provides a mechanism for neutral halide production. The higher temperature at which **IL-4** starts to off-gas iodine is consistent with the previously observed trend of decreasing tendency to loose halogen with increasing halide to halogen ratio.³⁹

2.5 Conclusion

Four interhalide polyhalide ionic liquids have been synthesised, $[C_6C_1Im][BrI_2]$, $[C_6C_1Im][Br_2I]$ and $[C_6C_1Im][Cl_2I]$, $[C_6C_1Im]_2[Br_3I]$, and have investigated the speciation of each by XPS. It has been shown that all of the polyhalide species are very weak bases and show low cation-anion coordination, as evidenced by a low degree of interionic charge-transfer observed in XPS. It has also been shown that the trihalide anion $[Br_2I]^-$ is generally stable under vacuum at room temperature, but there is a noticeable loss of iodine over the course of 70 h, and that the thermal stability (in terms of halogen off-gassing, as measured by vapour-phase MS) can be increased by the addition of a molar excess of bromide, to form the supposed polyhalide species $[Br_3I]^{2-}$. Conversely, it was shown that the trihalide in the IL $[C_6C_1Im][BrI_2]$ is not vacuum stable, rapidly releasing iodine during pump-down for XPS analysis. It has also shown that the off-gassed halogen is not the initial interhalide used to make the trihalide ILs, rather that it is iodine. This is evidence that polyhalide interconversion observed in aqueous and polar organic solution also occur in ionic liquid solution.

3 Reactions of a Polyhalide Ionic Liquid with Copper, Silver, and Gold

PUBLISHED AS: Reactions of a Polyhalide Ionic Liquid with Copper, Silver, and Gold⁵



3.1 Introduction

Ionic liquids are a quite new class of salts that are often liquid well below 100 °C. They exhibit unique physico-chemical properties such as extremely low vapour pressures, wide electrochemical windows, and unusual solvation characteristics, to name only a few, which makes them candidates for many applications.⁶⁰ ILs are mostly comprised of organic

cations and organic or inorganic anions that are covalently bound molecular entities. More unusual are ILs that are based on polyhalide anions such as triiodide $[I_3]^-$, due to the associated $I^- + I_2 \rightleftharpoons [I_3]^-$ equilibrium.⁵⁹

Polyhalide anions have a long history in aqueous systems, but have only recently been an active area of interest in the case of ILs. New synthesis techniques have allowed for an expansion of the number of known polyhalide anions (particularly those of the lighter halides), and several interesting potential applications involving polyhalide ILs have emerged.^{39,40} Tribromide salts have been used in organic synthesis as convenient bromination agents for some time now⁴⁵. Tribromide- and trichloride-containing ILs exhibit enhanced reactivity and higher yields in halogenation reactions.⁴⁶⁻⁴⁸ Moreover, they also exhibit stereo-⁴⁹ and regioselectivity,⁸ and the reuseability of some of these agents has been shown.^{8,49,50} In addition, IL-based polyhalides have great potential as 'green' halogenation reagents due to their low volatility making them easier to handle than the base halogens. Another field of application for trihalide ionic liquids is related to the electrolyte in dye-sensitised solar cells (DSSCs). The 'classic' DSSCs based on IL electrolytes make use of the $[I_3]^-/I^-$ redox couple⁵¹⁻⁵³. Recently, $[Br_3]^-/Br^-$ based redox couples have also come into focus in this context⁵⁴. Polyhalide ionic liquids are of interest as components of both liquid and quasi-solid electrolytes.⁷ Understanding the behaviour of polyhalide species in ionic liquids is therefore an important step in optimising redox couple/electrolyte chemistry. Moreover, understanding the corrosive nature of polyhalide-containing electrolytes in contact with metal electrodes – often made from precious metals and/or carbonaceous electrodes decorated with metal electrocatalysts – is crucial for understanding the long-term stability issues of DSSC devices. It is known that iodine is corrosive to metallic grid contracts such as silver when water and air are present.⁶¹

Further, wet-chemical metal dissolution plays an important role when etching gold microstructures in microelectronic devices by use of aqueous I_2/I^- trihalide systems, or when employing cyanide-based chemistry for gold leaching, to name only two examples. The latter approach has the disadvantage of high toxicity and disposal issues, the former suffers from volatile iodine formed during the etching process – a recent review of gold etching for microfabrication was recently published by Green.⁶² The recovery of scrap metals is a related potential application:

Li et al. have recently applied several trichloride ILs to the dissolution of various metals,⁶³ and found that they are good oxidative solvents for a range of metals, however the imidazolium cation is halogenated by $[\text{Cl}_3]^-$. This is a potential issue in scrap metal recovery because any halogenated organic materials produced during the metal recovery process would have to undergo special processing before ultimate disposal.

One of the key properties of ILs is their low volatility, which allows for investigations under ultra-high vacuum (UHV) conditions such as X-ray photoelectron spectroscopy (XPS). Over the last decade, XPS studies on a large number of non-trihalide IL systems have been successfully carried out proving the strength of this surface-sensitive technique – for reviews, see Steinrück¹¹ and Maier et al.¹² XPS has also recently been applied to trihalide ionic liquid systems by Men et al.⁴¹ Using a conventional laboratory XPS setup, the authors showed for imidazolium-based $[\text{Br}_2\text{I}]^-$ and $[\text{I}_3]^-$ ILs that the vapour pressure was low enough to perform XPS, and that beam damage effects are negligible when restricting X-ray exposure. By analysing binding energy shifts and shake-up loss features present, Men et al. clearly showed that $[\text{Br}_2\text{I}]^-$ and $[\text{I}_3]^-$ are weakly-coordinating anions with a very low basicity. The negative charge on the anions is delocalised over the trihalide complexes forming an extended π -system. For $[\text{Br}_2\text{I}]^-$, the authors found the central iodine atom sitting in the linear $[\text{Br}-\text{I}-\text{Br}]^-$ complex to be less electronegative than its bromine neighbours.⁴¹

For their XPS studies, Men and co-workers placed small IL droplets onto a stainless steel sample holder. Initial efforts by our group to investigate similar trihalide ILs, in the form of thin films spread on polycrystalline gold plated stainless steel (our standard inert support), were stymied by the fact that the brownish IL films quickly darkened first and then lightened under UHV. Once these sample holders were removed from the chamber, it was found that the gold plating had been striped away, figure 3.1. Moreover, these IL samples on gold gave an in-

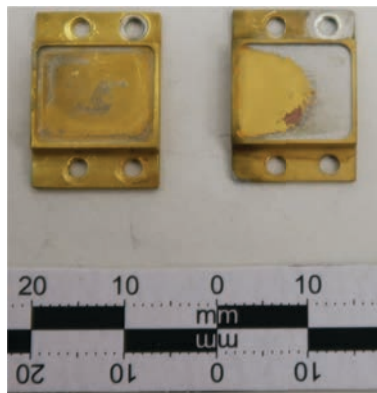


Figure 3.1: Two gold plated sample holders after attempts to measure the ILs in the ESCA.

creased background pressure compared to conventional ILs, which gave a first indication of a corrosion reaction between the IL and gold yielding volatile by-products.

In order to elucidate the effect of trihalide ILs on noble metals, a systematic investigation of the group 11 metals (Au, Ag, and Cu) was carried out. The three metals of the same group have been chosen as they are relevant electrode contact materials in DSSCs and in electronic devices in general. They were exposed to two imidazolium-based ILs with the trihalide anion dibromiodide $[\text{Br}_2\text{I}]^-$, namely 1-hexyl-3-methylimidazolium dibromodiodide ($[\text{C}_6\text{C}_1\text{Im}][\text{Br}_2\text{I}]$) and 1-butyl-2,3-dimethylimidazolium dibromiodide ($[\text{C}_4\text{C}_1\text{C}_1\text{Im}][\text{Br}_2\text{I}]$). The latter was chosen to elucidate the potential role of metal carbene formation. It will be demonstrated that our corrosion procedure is a simple way to synthesise IL systems with a high content of gold(I), silver(I), and copper(I) species, which are stable against exposure to ambient conditions and water. In contrast to extensive studies of transition metals, aluminium, and steel alloys corroded by ionic liquids,^{64–66} to the best of our knowledge this is the first systematic investigation on etching group 11 metals with a trihalide ionic liquid.

3.2 Methods and Materials

3.2.1 IL Synthesis

The room temperature trihalide ionic liquid $[\text{C}_6\text{C}_1\text{Im}][\text{Br}_2\text{I}]$ was prepared by mixing 1-hexyl-3-methylimidazolium bromide ($[\text{C}_6\text{C}_1\text{Im}]\text{Br}$, purity 99 %, purchased from IoLiTec and used without further processing, highly viscous liquid at room temperature) with iodine monobromide (IBr, 98 %, Sigma-Aldrich) in a 1 : 1 molar ratio. After mixing both ingredients, a deep red-brown liquid with a considerably lower viscosity than $[\text{C}_6\text{C}_1\text{Im}]\text{Br}$ was obtained. IL exposure to daylight was avoided in order to prevent any photochemical reactions that might occur.

To investigate whether carbene formation plays a role in the reaction, a non-carbene forming trihalide counterpart, $[\text{C}_4\text{C}_1\text{C}_1\text{Im}][\text{Br}_2\text{I}]$, which is methylated at the 2-position of the imidazolium ring). This IL was prepared by mixing 1.314 g (5.634 mmol) of dry 1-butyl-3-dimethylimidazolium bromide ($[\text{C}_4\text{C}_1\text{C}_1\text{Im}]\text{Br}$, 99 %, IoLiTec, used without further processing, melting point around 90 °C) with 1.175 g (5.681 mmol)

of IBr – a 1 : 1 molar ratio. After the IL was weighed out, it was briefly stored in an evacuated bell jar while the IBr was weighed out, to minimise moisture adsorption. When the two ingredients were mixed in a mortar, the IL initially liquefied, and a deep red-brown liquid was obtained. The mixture was then placed in an evacuated bell jar to remove absorbed water from the hygroscopic compound, leading to solidifications after several minutes under vacuum. After re-grinding again, the obtained deep orange powder exhibited a melting point in the range of 40–50 °C.

1-ethyl-3-methylimidazolium tetrabromoaurate(III) ([C₂C₁Im][AuBr₄]) was also synthesised as an analogous Au^{III} compound, which served as an XPS binding energy reference: A 50 mL 2-neck flask, fitted with a septum and a reflux condenser, was charged with 454.6 mg (0.98 mmol) of AuBr₃ (99.9 %, Sigma-Aldrich) and 193.7 mg (1.01 mmol) of 1-ethyl-3-methylimidazolium bromide ([C₂C₁Im]Br, >97 %, Sigma-Aldrich). With a syringe, 20 mL of dry acetonitrile was added through the septum and the initial suspension was refluxed overnight. After cooling, the deep red solution was syringe filtered (0.45 µm, cellulose) and transferred to a 50 mL flask. The solvent was evaporated by means of a rotary evaporator, yielding 616.8 mg (95.1 %_{wt} of the total starting mass) of a dark red solid. The material was analysed with Inductively Coupled Plasma Optical Emission Spectrometry (ICP-OES) revealing an Au content of 30.3 %_{wt} (nominal content 31.4 %_{wt}).

3.2.2 Metal Foil Corrosion

To investigate the effect of the trihalide ILs on group 11 metals, 15 × 20 mm foils of polycrystalline copper (0.1 mm thickness, ≥99.99 %, MaTecK), silver (0.125 mm, 99.9 %, ChemPUR, pre-treated with fine silicon carbide paper), gold (0.1 mm, >99.99 %, MaTecK) and molybdenum (0.1 mm, 99.95 %, MaTecK) were rinsed with acetone, dried, and weighed and then immersed in ~1 ml of [C₆C₁Im][Br₂I] in a glass boiling tube under air. The tubes were closed (but not sealed), and then heated to 40 °C for 6 h in a water bath. A second gold foil was also subjected to a more extended exposure to the [C₆C₁Im][Br₂I]. The foil was initially exposed to [C₆C₁Im][Br₂I] at 40 °C for about 11 h, then left in the IL without heating for a further 10 h period. A third gold foil of mass 619.8 mg was also corroded by [C₄C₁C₁Im][Br₂I] using the same procedure, except that the corrosion experiment was carried out at 50 °C, due to the higher melting point of the C₂-methylated IL. For each corro-

sion experiment, the boiling tubes were gently shaken occasionally. At the end of the exposure period, a few drops of the liquid were removed from the tubes and placed on a molybdenum sample holder, forming a thin layer for XPS analysis. The metal foils were removed from the tubes, rinsed with acetone, dried, and weighed again. In addition, a 0.1 mm thick gold foil together with a 1 mm thick gold wire were half- and fully-immersed into $[\text{C}_6\text{C}_1\text{Im}][\text{Br}_2\text{I}]$ at room temperature for about 17.5 h. These samples were studied with scanning electron microscopy (SEM).

Two further corrosion experiments were performed to elucidate the roll of water in the gold corrosion process using 'dry' $[\text{C}_6\text{C}_1\text{Im}][\text{Br}_2\text{I}]$, and 'wet' $[\text{C}_6\text{C}_1\text{Im}][\text{Br}_2\text{I}]$: In the dry IL experiment, 2.072 g (4.56 mmol) of $[\text{C}_6\text{C}_1\text{Im}][\text{Br}_2\text{I}]$ was dried by heating to 50 °C in a continuously evacuated Schlenk flask for 24 h. After this, a gold foil section (mass 609 mg) was added and the vessel purged with nitrogen (Linde, 5.0) before being sealed against air contact. For the wet IL experiment, 1.933 g (4.26 mmol) of the IL was added to a Schlenk flask, followed by 543 mg (30.1 mmol, 0.5 ml) of deionised water. Despite agitating for several minutes, the two liquids were not miscible, with the water forming a layer above the IL. This layer was initially a slight red-brown colour. A gold foil (526 mg) was then placed into this bi-layered system and fully immersed in the IL phase. The Schlenk flask was then stoppered. Both Schlenk flasks were held in a water bath at 40 °C for 6 h. Samples of the ILs after reaction was taken for XPS analysis and the masses of the remaining gold foils were measured.

3.2.3 NMR Analysis

The IL from the extended gold corrosion experiment and a sample of the same batch of the neat $[\text{C}_6\text{C}_1\text{Im}][\text{Br}_2\text{I}]$ IL was subjected to ^1H - and ^{13}C -NMR. The spectra acquired were recorded without co-solvent but with an acetone standard as a sealed insert.

3.2.4 Scanning Electron Microscopy

Two samples of corroded gold were prepared for microscopic examination – one section of gold foil (0.1 mm, >99.99 %, MaTecK) that was only partly submerged in the IL, and a section of gold wire (\varnothing 1.0 mm, Heraeus) that was fully immersed. After rinsing with acetone, both of these samples were exposed to the IL together for 17 h and 35 min

at room temperature. The gold samples were then rinsed in acetone, and mounted onto standard sample stubs for SEM imaging. The EHT voltage used was 20.00 kV, and the probe current was set to 400 pA.

3.2.5 XPS Analysis

Before and after reaction, XPS analysis was performed for all IL samples. They were placed on a pre-cleaned molybdenum sample holder by spreading into a thin liquid film of about 0.1 mm thickness at the bottom of a reservoir of dimensions $14 \times 20 \times 0.5$ mm milled into the sample holder. Details of the sample holder construction can be found in appendix B. The sample holder was introduced to a fast-entry load lock (base pressure 5×10^{-7} mbar) and pumped down overnight before being transferred to the main section of the UHV system for XPS analysis (base pressure better than 1×10^{-10} mbar).

In contrast to most IL samples, which were measured at room temperature, the spectra involving the IL $[\text{C}_4\text{C}_1\text{C}_1\text{Im}][\text{Br}_2\text{I}]$ were collected at 45 °C and 55 °C. The higher temperatures were necessary to melt these IL samples to avoid charging. A type K thermocouple was used to monitor the temperature of the heated samples, with the thermocouple controller regulating the voltage of the heating filament. During measurements, the relative temperature was maintained to within ± 0.1 °C; absolute sample temperature values were within ± 5 °C³⁰.

In the XPS system, the radiation source was the non-monochromated Al K_α anode of a Specs XR-50 dual anode source, operating at 12.00 kV and 20 mA emission current. All spectra were recorded in normal emission, in order to integrate over the maximum probing depth (7–9 nm, depending on the kinetic energy^{13,14}) with a Scienta R3000 concentric hemispherical analyser in constant pass energy mode, using 200 eV pass energy for wide spectra and 100 eV for detailed spectra. For the latter, the overall instrument energy resolution was 0.9 eV – for more details on the XPS system see Lovelock et al.⁶⁷

Data collected were analysed with CasaXPS and charge-corrected such that the aliphatic carbon peak is at 284.8 eV. Note that for the systems studied here, only minor charge corrections, on the order of ± 0.1 eV, had to be applied. Peaks in the XP spectra that were associated with non-metal elements were fitted with a pseudo-Voigt profile with a 30 % Lorentzian contribution. Doublets due to spin-orbit splitting (such as I 3d) were fitted with two peaks constrained to have equal full width at half maxima and the expected peak area ratio (*e.g.* 2 : 3 for

$d_{3/2}$: $d_{5/2}$). Metal peaks were fitted similarly, except the pseudo-Voigt profile had an 80 % Lorentzian contribution. Shirley backgrounds were used. Carbon 1s spectra were fitted with model with a two peak model, C_{alkyl} and C_{hetero} . The C_{hetero} peak was constrained to a full width at half maximum of $1.1 \times$ the width of the C_{alkyl} peak.

3.2.6 Vapour Phase Mass Spectrometry

To test for volatile components during metal corrosion under vacuum conditions, gas phase spectra of $[C_6C_1Im][Br_2I]$ in contact with copper and with molybdenum were recorded in a separate small system for mass spectrometry (the Mass Spectrometry Chamber, MSC, base pressure 5×10^{-8} mbar). Copper and molybdenum were chosen as the extreme cases of most and least reactive metals with $[C_6C_1Im][Br_2I]$, respectively. The MSC is a small UHV chamber equipped with a copper sample head (inserted into the chamber from below) that can be directly cooled and heated, and a quadrupole mass spectrometer (QMS, Hiden HAL 511 3F with cross ionisation source, 2–550 amu, for full details see Deyko et al.⁶⁸). Between experiments, the sample head was cleaned with fine sand paper to remove any corrosion, and then rinsed thoroughly with acetone.

In the on-copper experiment, a drop of $[C_6C_1Im][Br_2I]$ was spread onto a 10×10 mm reservoir milled into the copper sample head (previously cleaned with acetone). Immediately after, the sample head was loaded into the MSC and pump-down started. As discussed later, the pump-down took longer than expected for non-reactive ILs, so mass spectra were collected during to investigate potential off gassing. Another set of spectra were taken once pump-down was complete.

In the on-molybdenum experiment, a drop of $[C_6C_1Im][Br_2I]$ was spread in a molybdenum foil boat (cleaned by ultrasonication in acetone), then loaded into the MSC and pumped down. For this IL, the pump-down rate was normal, hence no mass spectra were collected during pump-down. Once pump-down was complete, mass spectra were collected at room temperature and 40 °C.

3.3 Bulk Metal Corrosion Results

When immersing the copper, silver, and gold foils into the IL $[C_6C_1Im][Br_2I]$, it was noted that the IL initially dark red-brown IL turned black within

	Au	Au-21h	Ag	Cu	Mo
Initial / mg	480	528	384	267	329
Final / mg	245	198	196	62.5	328
Δ / mg	235	330	188	205	1
Δ / $\text{g}\cdot\text{dm}^{-2}\cdot\text{d}^{-1}$	18.9	6.89	12.3	13.8	~ 0
Δ / $\mu\text{m}\cdot\text{min}^{-1}$	0.068	0.025	0.082	0.106	~ 0
Δ / mmol	1.19	1.68	1.74	3.22	~ 0
IL / mg	1783	1935	1854	1874	1998
IL / mmol	3.93	4.26	4.08	4.13	4.40
Metal : Im	0.30 : 1	0.39 : 1	0.43 : 1	0.78 : 1	0 : 1
Metal % _{mol}	23	28	30	44	0

Table 3.1.: Change in mass of the metal foils after immersion in $[\text{C}_6\text{C}_1\text{Im}][\text{Br}_2\text{I}]$ at 40°C for 6 h. In the case of Au-21h, the Au foil was kept in the IL at 40°C for 11 h, then left for a further 10 h at room temperature.

minutes and became more viscous over time. This darkening process occurred much faster for the copper foil than for the gold and silver foils. For the molybdenum foil, no colour change was noted.

All the group 11 metal foils (gold, silver, and copper) showed considerable mass loss after exposure to $[\text{C}_6\text{C}_1\text{Im}][\text{Br}_2\text{I}]$ for six hours at 40°C (table 3.1). Converting the mass loss to metal mmol, copper was dissolved to the largest extent (3.22 mmol per 4.1 mmol initial IL, that is, nominally a 0.78 : 1 ratio) compared to gold (0.30 : 1) and silver (0.43 : 1). For the extended exposure gold foil (labelled Au-21h in table 3.1), the slightly increased gold mass loss after the extended exposure showed that maximum amount of gold dissolution had not yet been reached after 6 h; nevertheless, the 6 h exposure will be discussed here in most cases for consistency. In contrast to the group 11 metals, molybdenum showed virtually no mass loss.

Visual inspection of the metals before and after corrosion (figure 3.2) revealed a clear change of the copper, silver, and gold foils: instead of the shiny smooth surface, tarnished patches were seen on copper and silver; in the case of copper, the apparent greenish patina is consistent

3 Reactions of a Polyhalide Ionic Liquid with Copper, Silver, and Gold

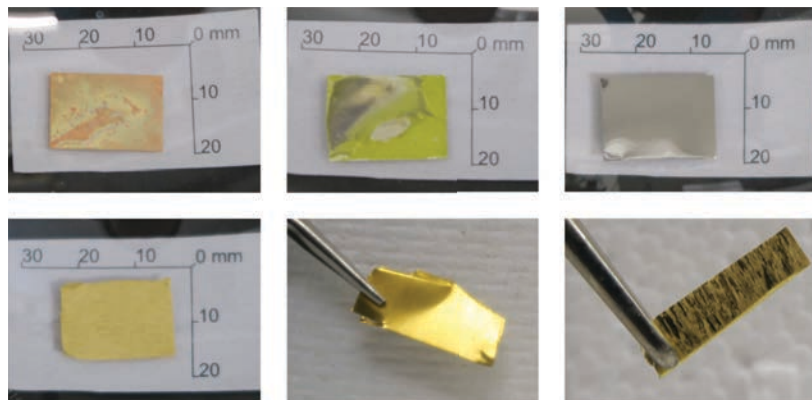


Figure 3.2.: Metal samples after immersion in $[\text{C}_6\text{C}_1\text{Im}][\text{Br}_2\text{I}]$ for 6 h – from top left to bottom right, copper, silver, gold, clean gold foil, and corroded gold foil.

with the formation of copper halide salts. Gold did not show any colour changes, but was clearly etched – the elongated grain structure typical of a rolled polycrystalline foil became apparent after the immersion in the trihalide IL. In contrast to the group 11 metals, molybdenum exhibited no visual changes of the surface; both negligible mass loss and the unchanged surface appearance indicate that no corrosion of the molybdenum foil took place.

The SE micrographs give a better microscopic view of reacted gold foil – figure 3.3 shows the micrographs of partly immersed foil. Whereas the unexposed part of the foil revealed a smooth and flat appearance, the immersed part displayed a rough surface with etching grooves and pits on the μm scale. Moreover, the exposed Au wire, figure 3.4, clearly revealed a decrease in diameter by roughly -7% (from $\varnothing 0.99$ mm to $\varnothing 0.92$ mm), with the formerly smooth surface becoming rough and decorated with etching pits on the μm scale.

From the mass losses summarised in table 3.1, it is clear that the three group 11 metals are susceptible to considerable bulk corrosion by $[\text{C}_6\text{C}_1\text{Im}][\text{Br}_2\text{I}]$, leading to an IL solution with metal content well above $20\%_{\text{mol}}$. In order to compare with common dissolution rates, such as metal loss per exposed surface area per unit time (typically reported as $\text{mg}\cdot\text{dm}^{-3}\cdot\text{d}^{-1}$ and change in foil height per unit time (typical units $\mu\text{m}\cdot\text{min}^{-1}$), the corresponding values are also given in table 3.1.

Note in the case of the most noble metal gold, the 6 h etching rate is in the same order of magnitude as typical wet-chemical etching rates of $0.1\text{--}1\ \mu\text{m}\cdot\text{min}^{-1}$ employing aqueous I_2/I^- or alkaline cyanide etching process.⁶²

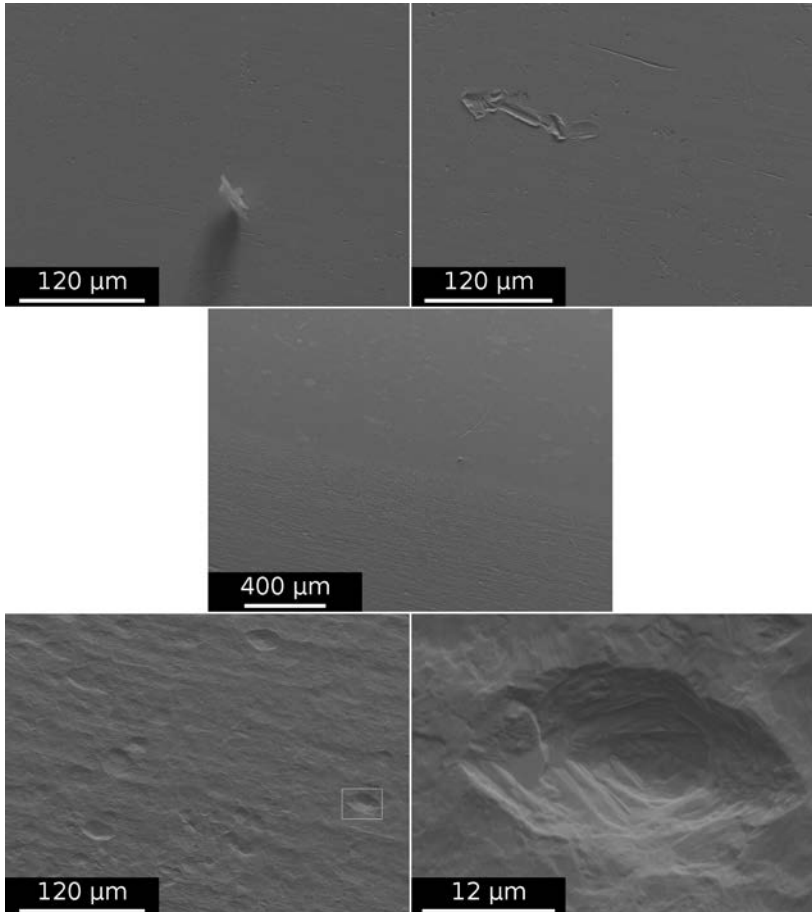


Figure 3.3.: SEM micrographs a partly submerged gold foil, uncorroded section (top) and corroded section (bottom). Centre image is the border between the corroded and uncorroded regions.

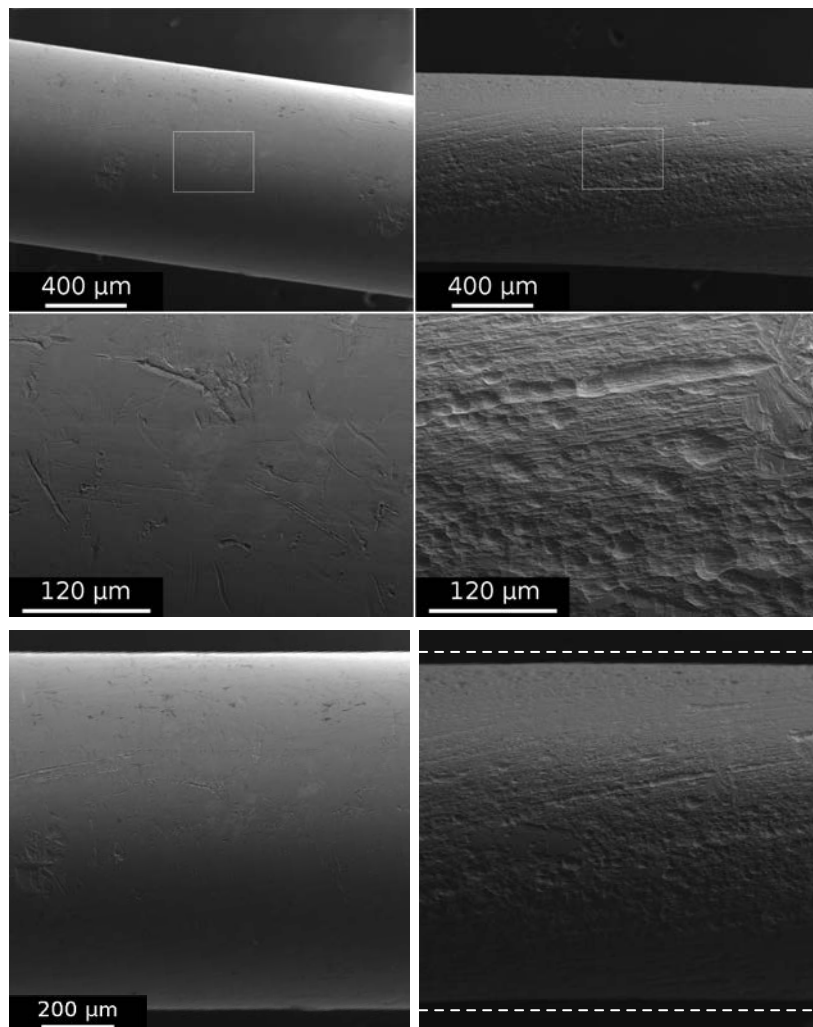


Figure 3.4.: SEM micrographs of two gold wires, one uncorroded (left) and one after exposure to the trihalide IL (right).

Due to the high metal contents in the IL solutions obtained after reaction, metal core level signals were expected to be clearly detectable in XPS. After the 6 h corrosion experiments, the solutions were placed onto

a molybdenum XPS sample holder and transferred to the XPS system. The chemical nature of the dissolved metal species as deduced from XPS will be discussed in detail in a later section. Concerning concentration values derived from XPS intensities, in direct comparison with the mass loss values shown in table 3.1, the quantification of metal content will be discussed in the following. For quantification, the measured XPS intensities are converted in table 3.2 into number of atoms, taking the corresponding relative sensitivity factors (RSF) into account. The signals of all atoms are normalised to the nitrogen signal originating solely from the imidazolium cation (that is, two nitrogen atoms per cation). For the group 11 metals, metal-to-imidazolium ratios between 0.4 and 0.5 to one were found in XPS, whereas no molybdenum signals were found for the Mo sample, confirming negligible corrosion for this metal. Striking in table 3.2 is the reduced content of trihalide-iodide, particularly in the case of the copper corrosion experiment. Apparently, the group 11 metal corrosion goes along with a loss of iodine. One should note that apart from IL and metal signals, minor amount of oxygen and an excess of carbon were also detected; these are discussed in the next section.

All in all, the mass losses of the foils after 6 h of immersion in the polyhalide IL as well as the quantification of the XP signals of the remaining solutions reveal consistently that for the group 11 metals gold, silver, and copper, a considerable amount of metal was dissolved into the IL whereas molybdenum was virtually unaffected. In the next section, the XP spectra of the neat trihalide IL $[C_6C_1Im][Br_2I]$ and the solutions remaining after the corrosion experiments will be discussed in detail.

3.4 XPS of Neat $[C_6C_1Im][Br_2I]$ Before and After Reacting With Cu, Ag, Au, and Mo

As described above, $[C_6C_1Im][Br_2I]$ quickly changed its colour from dark brown to black in contact with the group 11 foils in the course of the corrosion experiments. During degassing in the load lock vacuum, the films lightened considerably, with the silver and gold ILs turning a lighter red-brown colour than the initial IL, and the copper IL became more or less fully transparent. Survey XP spectra, IL-, and metal-related detailed core level scans of the neat degassed $[C_6C_1Im][Br_2I]$ trihalide IL and for the IL solutions after the 60 h corrosion experiments with Au, Ag, Cu, and molybdenum foils are shown in figures 3.5 and 3.6. The

3 Reactions of a Polyhalide Ionic Liquid with Copper, Silver, and Gold

C_{alkyl} peak at 284.8 eV served as an internal reference for the binding energies, as has been done earlier.⁶⁷

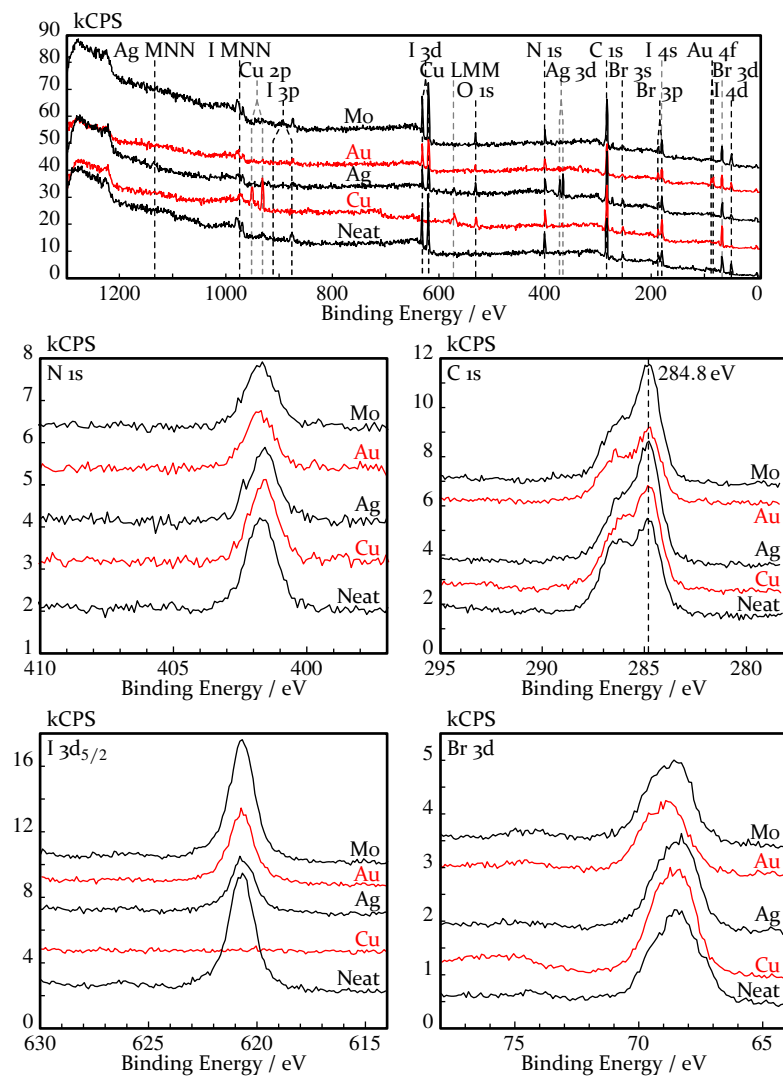


Figure 3.5.: Survey and IL region spectra for the ILs used in the metal corrosion testing.

3.4 XPS of Neat $[C_6C_1Im][Br_2I]$ Before and After Reacting With Cu, Ag, Au, and Mo

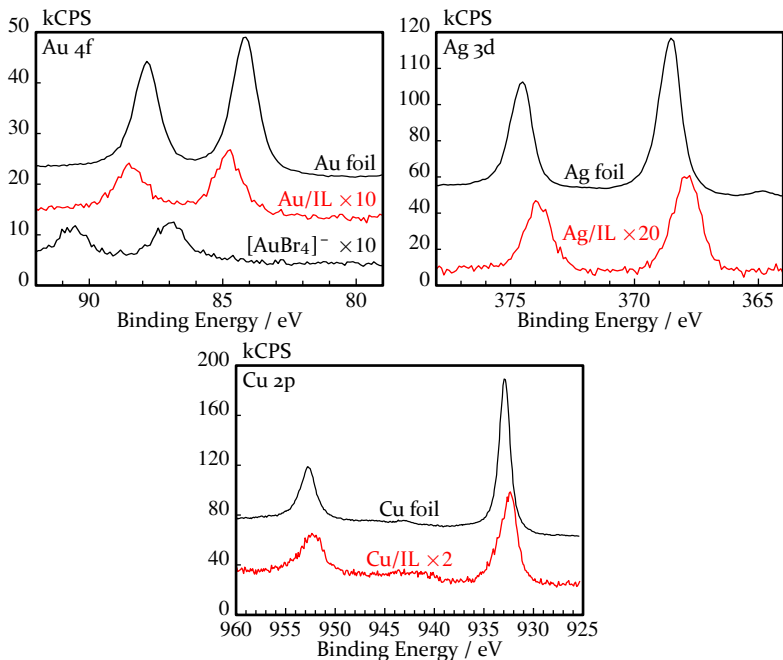


Figure 3.6.: Metal region spectra for the ILs exposed to metals at 40 °C, and sputtered metal foils.

Figure 3.5 shows the survey spectra and the IL-related detailed core level spectra. In the C 1s region, the deconvoluted peaks originate from the five terminal carbon atoms of the alkyl chain at 284.8 eV (C_{alkyl}) and from the five carbon atoms directly attached to a nitrogen atom at 286.5 eV (C_{hetero}). The integrated area of the two carbon signals of the neat IL reveal a $C_{\text{alkyl}} : C_{\text{hetero}}$ ratio of 1.1 : 1.0, which matches the expected 5 : 5 ratio to within the accuracy of our method ($\pm 10\%$). The anion-related signals of the neat IL show a single iodine peak in the I $3d_{5/2}$ region at 620.7 eV, and in the Br $3d_{3/2,5/2}$ region at around 68.5 eV (note that due to the small spin-orbit splitting of the Br 3d signals, the reported binding energy values refer to the peak maxima). Notably, the I $3d_{5/2}$ and the Br 3d signals of $[C_6C_1Im][Br_2I]$ are considerably shifted to higher binding energy (by +2.4 eV and +1.1 eV), as compared to the analogous monohalide ILs $[C_6C_1Im]I$ and $[C_6C_1Im]Br$, respectively (see chapter 2 for details). These shifts to higher binding

energy mainly relate to the delocalisation of the negative charge over the trihalide anion as compared to the monohalide anions, and have already been discussed by Lovelock et al.⁴¹ From XPS binding energy shifts and Kamlet-Taft solvent parameter measurements, the authors showed that the trihalide anion $[\text{Br}_2\text{I}]^-$ is an extremely weakly-coordinating anion with a very low basicity. In our measurements, this is reflected by the larger binding energy separation if the C_{alkyl} and C_{hetero} peaks for $[\text{C}_6\text{C}_1\text{Im}][\text{Br}_2\text{I}]$ as compared to the $[\text{C}_6\text{C}_1\text{Im}]\text{Br}$ and $[\text{C}_6\text{C}_1\text{Im}]\text{I}$ monohalide ILs (see the C 1s spectra in figure 3.7). A detailed explanation of the significance of the separation is given by Cremer et al.¹⁸ In short, a more strongly coordinating anion such as bromide allows for greater partial electron transfer to the imidazolium ring, leading to a lower positive charge, and thus, a shift of the C_{hetero} peak to lower binding energies. Hence, the large $\text{C}_{\text{hetero}}-\text{C}_{\text{alkyl}}$ peak separation found for $[\text{C}_6\text{C}_1\text{Im}][\text{Br}_2\text{I}]$ confirms the low coordination strength of the $[\text{Br}_2\text{I}]^-$ anion as already proposed by Men et al.⁴¹

Furthermore, the I 3d and Br 3d signals from the $[\text{Br}_2\text{I}]^-$ polyhalide anion are found at considerably higher binding energies than the ones

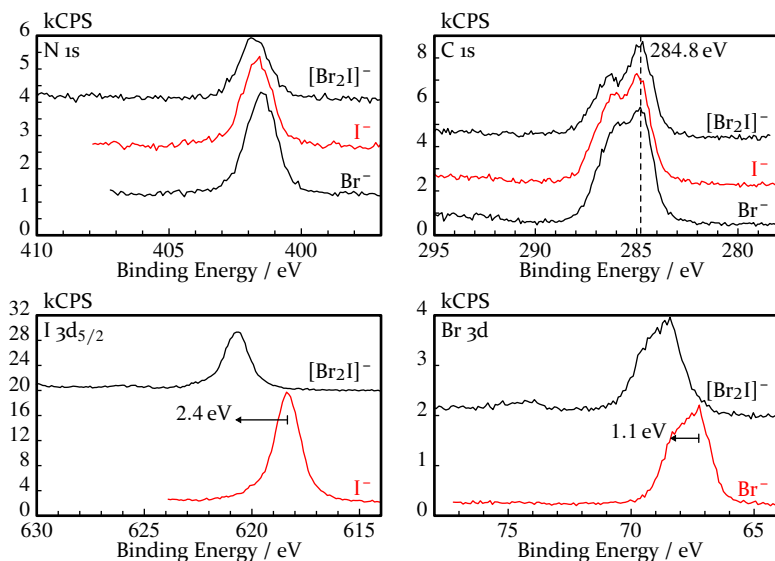


Figure 3.7.: Comparison of the monohalides $[\text{C}_6\text{C}_1\text{Im}]\text{I}$ and $[\text{C}_6\text{C}_1\text{Im}]\text{Br}$, and the trihalide $[\text{C}_6\text{C}_1\text{Im}][\text{Br}_2\text{I}]$.

from the monohalide ILs: the trihalide I 3d_{5/2} peak is shifted by +2.4 eV and the Br 3d_{5/2} peak by +1.1 eV to higher binding energy, compared to [C₆C₁Im]I and [C₆C₁Im]Br, respectively, fully in line with the results from Men et al.⁴¹ These upwards shifts reflect the spreading of the negative charge across the three centres in the trihalide anion, in contrast to its localisation in the I⁻ and Br⁻ anions in [C₆C₁Im]I and [C₆C₁Im]Br, respectively.

Quantification of the XP intensities of neat [C₆C₁Im][Br₂I] leads to an overall good agreement with the nominal composition (table 3.2) apart from iodine content, which was found to be too low. For the neat IL, an atomic composition of iodine : bromine : nitrogen of 0.5 : 1.7 : 2.0 was found instead of 1 : 2 : 2 (in the case of the Mo foil corrosion, a slightly higher iodine content with an atomic ratio of 0.7 : 2.0 : 2.0 was found). This is attributed, as least partly, to some uncertainty in the atomic sensitivity factor used here for the I 3d_{5/2} core level quantification (note that an I : N ratio of 0.85 : 2.0 was found by XPS quantification in the case of [C₆C₁Im]I). Note that some of the intensity of the I 3d_{5/2} line is lost to a broad shake-up feature around 626 eV, due to their delocalised charge distribution⁴¹ – this shake-up feature was included in the quantification. Since the focus of this work lays on the metal corrosion, more detailed investigations have to be carried out in the future to elucidate this aspect.

The XP spectra after the 6 h corrosion experiment using the Mo foil show no Mo signals (e. g. Mo 3d around 230 eV), which corroborates the negligible mass loss found for the IL-exposed Mo foil (table 3.1). The only changes are a moderate decrease of the [C₆C₁Im][Br₂I] signals, which goes along with an increase in C_{alkyl} signal and the appearance of an O 1s peak at 530 eV. These additional C_{alkyl} and O signals are attributed to the appearance of non-volatile contaminants in the near-surface region after the corrosion experiment, possibly originating from residual glassware contamination and/or adsorption from lab air. Such contaminants have been reported to be surface-active,¹⁴ and therefore show up in XPS even at very low bulk concentrations.

Next, the IL derived spectra in figure 3.5 are discussed, taken after the 6 h corrosion experiments of the gold, silver, and copper foils at 40 °C. The most striking difference compared to the situation with molybdenum is the reduction in I 3d_{5/2} intensity (see the I 3d_{5/2} region in figure 3.5 and table 3.2). For the Au and the Ag solutions, the I 3d_{5/2} intensity decreased by -40 % and -50 %, respectively, compared to the

	C 1s	O 1s	N 1s	I 3d _{5/2}	Br 3d	Cu 2p	Ag 3d	Au 4f
RSF →	0.208	0.599	0.364	5.740	0.551	8.69	4.460	3.756
<i>nominal</i>	10	0	2	1	2	0	0	0
[Br ₂ I] ⁻	11.7	0.2	≡ 2	0.5	1.7	—	—	—
Cu	14.4	1.2	≡ 2	<0.1	2.2	0.5	—	—
Ag	16.5	1.3	≡ 2	0.3	1.9	—	0.4	—
Au-6h	15.2	0.6	≡ 2	0.5	2.1	—	—	0.4
Au-21h	15.7	1.4	≡ 2	0.4	2.0	—	—	0.4
Mo	17.3	1.4	≡ 2	0.7	2.0	—	—	—

Table 3.2.: Composition of [C₆C₁Im][Br₂I] before and after the bulk corrosion experiments (6 h at 40 °C) listed in table 3.1. The nominal composition of [C₆C₁Im][Br₂I] is also given.

signal of neat $[C_6C_1Im][Br_2I]$. In the case of copper, where the amount of metal dissolution was found to be highest (table 3.1), I 3d intensity was almost entirely absent. It is thus evident that during the reaction of the group 11 metals with the IL, iodine from the $[Br_2I]^-$ is consumed. Since no precipitate was found, a neutral iodine-containing species is apparently formed, that desorbs under vacuum conditions. Because the Br 3d intensity did not decrease (and thus, no neutral IBr had formed), it was most likely molecular iodine, I_2 , that was pumped away. As tested in a separate UHV system, gas phase mass spectra indeed showed the release of I_2 from $[C_6C_1Im][Br_2I]$ when the IL was in contact with copper (discussed below). It is important to note that the Br 3d peaks shown in figure 3.5 also did not exhibit significant changes in binding energy or peak shape after exposure to Cu, Ag, and Mo (compared to before corrosion); only after Au corrosion, the Br 3d signals are slightly shifted by +0.3 eV to higher binding energy. Thus, the formation of free bromide (Br^-) during corrosion can be ruled out due to the absence of monohalide Br^- signals in the Br 3d region at lower binding energies.

Direct evidence for the dissolution of Au, Ag, and Cu is obtained from the survey spectra in figure 3.5 and the detailed metal spectra in figure 3.6. In contrast to molybdenum, where no metal signals could be detected in the IL, the XP spectra of the IL solutions after the corrosion experiments with Au, Ag and Cu clearly show the corresponding metal signals. The detailed spectra in figure 3.6 cover the most prominent metal core levels, that is Au $4f_{5/2,7/2}$ between 92–79 eV, Ag $3d_{3/2,5/2}$ between 388–364 eV, and Cu $2p_{1/2,3/2}$ between 960–925 eV. For comparison, XP spectra of Au^0 , Ag^0 , and Cu^0 in the form of freshly sputtered metal foils are also depicted in figure 3.6.

Both the Au^0 reference and the dissolved Au species show the typical spin-orbit split Au $4f_{5/2,7/2}$ doublet. While the Au $4f_{7/2}$ level of the Au foil, that is, Au^0 , is found at 84.1 eV, for the IL solution after corrosion it is shifted to higher binding energy by +0.7 eV, to 84.8 eV. This binding energy position is consistent with an Au^I species.⁶⁹ To rule out Au^{III} being present in the solution, the tetrabromaurate IL analogue $[C_2C_1Im][Au^{III}Br_4]$ was also measured, which showed a much higher shift of +2.8 eV to higher binding energy, that is, to 86.9 eV (figure 3.6). Notably, the widths of the Au 4f signals of the gold foil and of the IL solution are virtually identical, which is an indication that the Au^I metal ion in solution is present in a uniform chemical environment.

The clean silver foil exhibits a sharp Ag 3d doublet, with the Ag 3d_{5/2} level at 368.6 eV. For the IL solution after corroding the silver foil, a shift of the Ag 3d_{5/2} level to lower binding energy by -0.7 eV (to 367.9 eV) with no loss features is observed, which is indicative of the formation of an Ag^I species.^{70,71} Similarly, the copper 2p doublet of the Cu corrosion solution is also shifted to lower binding energies by -0.6 eV (with Cu 2p_{3/2} at 932.3 eV) with respect to the clean copper foil (with Cu 2p_{3/2} at 932.9 eV). The magnitude of the shift to lower binding energies and the absence of pronounced shake-up structures – which should be present for a Cu^{II} species – is fully in line with the formation of a Cu^I species.⁷²

3.5 Vapour Phase Mass Spectrometry

Upon contact with the copper, the [C₆C₁Im][Br₂I] foil turned black within less than one minute. In contrast to conventional non-trihalide ILs, the decrease in pressure was observed to be much slower than is typical for ILs (typically after 30 min a pressure of $\sim 1 \times 10^{-5}$ mbar is easily obtained with this setup). After 2.5 h from the start of pump down, the chamber eventually reached a pressure below 1×10^{-5} mbar

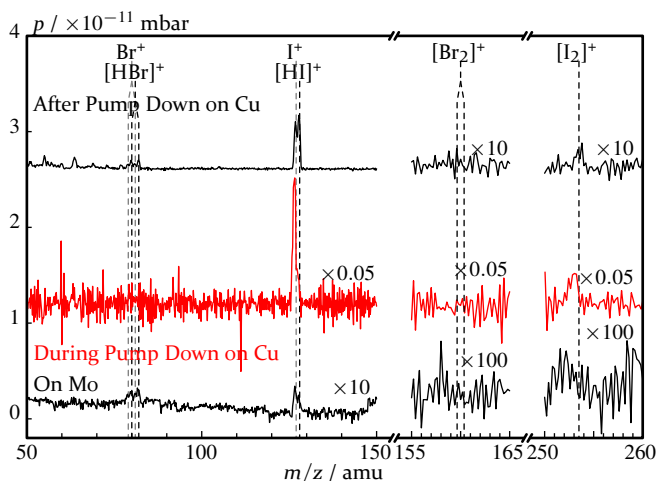


Figure 3.8. Mass spectra of [C₆C₁Im][Br₂I] on the copper sample head and in a molybdenum sample holder.

that allowed the start of the QMS in a very insensitive detection mode – that is, the secondary electron multiplier was set to a low acceleration voltage – for safety reasons (note that the signal-to-noise ratio is thus very low for low intensity signals), and gas phase mass spectra were taken (see figure 3.8). Visual inspection 24 h later at a chamber pressure of $\sim 1 \times 10^{-7}$ mbar revealed that the colour of several patches of the IL film on the copper plate had considerably lightened compared to the black colour at the beginning. A mass spectrum after the 24 h of degassing (taken in a high sensitivity mode with a much better signal-to-noise ratio) is also shown in figure 3.8, along with a mass spectrum of a $[\text{C}_6\text{C}_1\text{Im}][\text{Br}_2\text{I}]$ film spread on a molybdenum foil (taken after a pump down of about 2 h in the same high sensitivity mode). Note that the individual spectral regions in figure 3.8 are multiplied by very different scaling factors for direct comparison on a linear scale. During pump-down the sample off-gassed a significant amount of iodine, which can be seen as I^+ and I_2^+ mass signal peaks. The I^+ peak is significantly more prominent than the $[\text{I}_2]^+$, as expected for gas phase I_2 due to cracking inside the ionisation source of the QMS.⁵⁶ The intensity of these I_2 -related signals decreased by about two orders of magnitude after 24 h of pumping. In addition to the $[\text{I}_2]^+$ and I^+ signals, HI^+ was also detected, which is attributed to a reaction with residual H_2 and H_2O in the gas phase background of the MSC system and in the QMS ionisation source: similar $[\text{HI}]^+$ signals along with the expected $[\text{I}_2]^+$ and I^+ were also detected when dosing small amounts of I_2 vapour into the chamber via a dosing valve (see below).

Notably, no significant amount of gas phase Br_2 could be detected during this experiment, neither in the $[\text{Br}_2]^+$ region (which is the most prominent signal for gas phase Br_2 ⁵⁷), nor in the Br^+ region, figure 3.8. The same holds true for $[\text{BrI}]^+$, which was not detected either (spectra not shown).

For the drop of $[\text{C}_6\text{C}_1\text{Im}][\text{Br}_2\text{I}]$ spread on an Mo foil, the pump-down time in this case was similar to conventional ILs, so the QMS could be started after about 2 h in the high-sensitivity mode. The mass spectra collected at room temperature and at 40°C (not shown) did not exhibit significant I_2 -related signals in the gas phase; the small $\text{I}^+ / [\text{HI}]^+$ peak is assigned to background contamination from the previous experiments, because it is visible without a sample loaded.

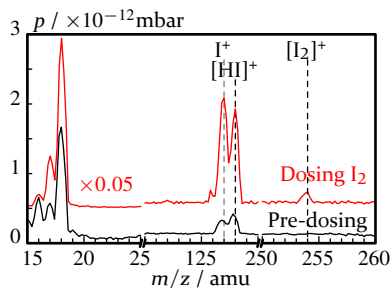


Figure 3.9: Vapour phase mass spectra of the MSC chamber background (1.0×10^{-8} mbar) and of the MSC with iodine dosed to a total pressure of 1.1×10^{-7} mbar.

At a background pressure of 1.0×10^{-8} mbar (the lower limit of the cold-cathode pressure gauge) survey and region scans of the chamber's residual gas were taken, then the needle valve was opened, and iodine dosed to a total pressure of 1.1×10^{-7} mbar. As shown in figure 3.9, both the iodine and hydrogen iodide peaks increase – this is consistent with the formation of HI being due to a reaction between iodine vapour and water vapour or hydrogen in the mass spectrometer's ionisation chamber.

To rule out that the $[\text{HI}]^+$ signal at 128 amu was related to the investigated reaction, pure I_2 vapour was also tested in the MSC. For this purpose, a glass vial, charged with iodine, was attached to the MSC via a needle valve and cooled with liquid nitrogen. For the initial pump-down of the MSC, the valve between the iodine source and the chamber was left fully open until the chamber reached a pressure of 4.0×10^{-1} mbar, at which point the needle valve was closed, the li-

3.6 Additional Gold Corrosion Experiments

As shown above, a considerable amount of metal in the form of Au^{I} , Ag^{I} , and Cu^{I} species is dissolved by the trihalide IL at the expense of iodine. Whereas Ag^{I} and Cu^{I} species are stable oxidation states in aqueous systems (e.g. forming stable precipitates with dissolved halide anions), Au^{I} is metastable and prone to disproportionation to Au^{III} and Au^0 in water without stabilizing ligands⁷³ Moreover, gold is the most noble – and thus, most unreactive – metal in the series. Hence, further gold foil corrosion experiments were carried out to elucidate a) the effect of additional water, b) the role of the proton in the (2)-position of the imidazolium ring, and c) the replacement of the imidazolium cation by an inorganic cation. The results of these experiments are summarised in the following.

3.6.1 The Effect of Water

When carrying out the gold corrosion experiment under anhydrous (and inert atmosphere) and water saturated conditions for 6 h at 40 °C, no significant differences in the amount of gold dissolved is found, and also no significant differences in the XPS spectra (see table 3.3 and figure 3.10) compared to the results described above. The corrosion rate (table 3.3) is also not significantly different from corrosion under ambient conditions. This indicates that neither water nor oxygen are necessary for (nor inhibitory of) the corrosion of gold in contact with $[C_6C_1Im][Br_2I]$.

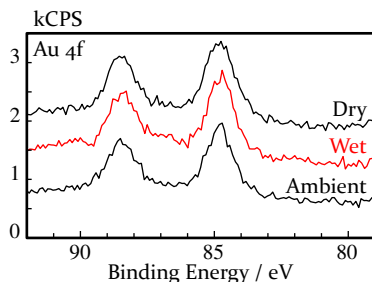


Figure 3.10.: Au 4f spectra of $[C_6C_1Im][Br_2I]$ after exposure to a gold foil under dry, water saturated, and ambient conditions.

	Dry	Wet	Amb.	Meth.
Initial / mg	609	526	480	620
Final / mg	361	287	245	445
Δ / mg	248	238	235	175
Δ / $g \cdot dm^{-2} \cdot d^{-1}$	15.7	17.5	18.9	10.9
Δ / mmol	1.26	1.21	1.19	0.887
IL / mg	2072	1933	1783	1422
IL / mmol	4.56	4.26	3.93	3.23
Metal : Im	0.28 : 1	0.28 : 1	0.30 : 1	0.27 : 1

Table 3.3.: Change in mass of gold foils after corrosion by dry $[C_6C_1Im][Br_2I]$, water saturated $[C_6C_1Im][Br_2I]$, and $[C_4C_1C_1Im][Br_2I]$, with the ambient condition $[C_6C_1Im][Br_2I]$ results from table 3.1 for comparison. The corrosion rate calculations were done as in table 3.1, with the surface area derived from the mass and the foil thickness (0.1 mm).

3.6.2 Possible Carbene Formation

Stable Au^I-imidazole-carbene complexes are well known in the literature, e. g. in the context of Au^I homogeneous catalysis.^{74,75} To rule out that the corrosion process found here requires or involves the formation of a stable Au^I-carbene (that most likely would occur by abstracting the most acidic proton, the one in the (2)-position of the imidazolium ring), ¹H- and ¹³C-NMR of the IL before and after Au corrosion were measured, figure 3.11. The acetone insert can be seen at around 2 ppm in the ¹H spectra, and at around 30 ppm in the ¹³C spectrum. Peak assignments for the ¹H and ¹³C spectra are from Marincola et al.⁷⁶ and Deyko et al.⁷⁷, respectively – in the proton spectra the (2)-position proton can be seen at around 7.8 ppm, and in the carbon spectra the (2)-position carbon

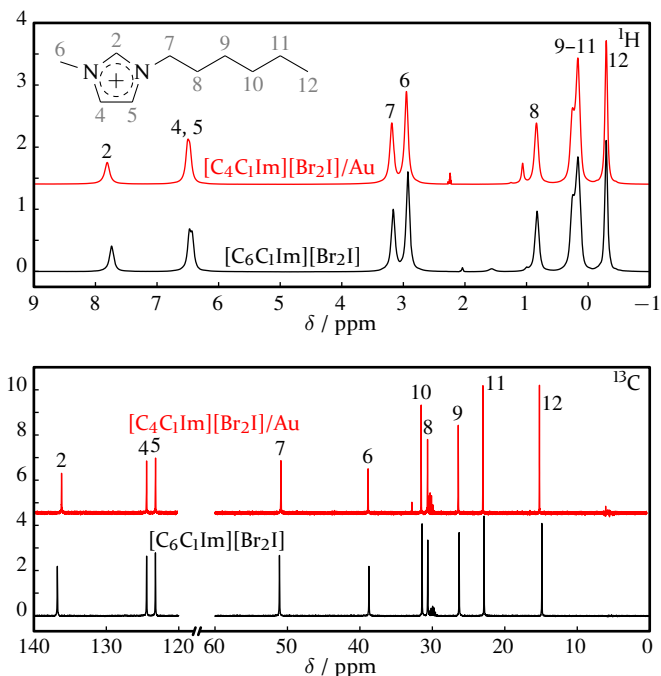


Figure 3.11. ¹H- and ¹³C-NMR of neat [C₆C₁Im][Br₂I] and [C₄C₁Im][Br₂I] reacted with gold. The ¹H-NMR are shifted to aligned with the terminal methyl peak of the neat trihalide (+0.20 ppm).

can be seen at around 137 ppm. These NMR spectra did not reveal any significant changes due to the gold corrosion. In particular, the signal intensity of the (2)-proton at 7.8 ppm does not decrease, which should not be the case for carbene formation.

Additionally, a trihalide homologue was tested, $[\text{C}_4\text{C}_1\text{C}_1\text{Im}][\text{Br}_2\text{I}]$, that was methylated in the (2)-position to prevent proton abstraction. Due to the ILs higher melting point, the corresponding corrosion experiment was carried at 50 °C. The foil mass loss results are given in table 3.3. The mass loss of the gold foil after 6 h was about 30% less than that of the non-methylated IL, which might be related to the higher viscosity of $[\text{C}_4\text{C}_1\text{C}_1\text{Im}][\text{Br}_2\text{I}]$ even at 50 °C; the molar amount of gold dissolved per mole of $[\text{C}_4\text{C}_1\text{C}_1\text{Im}][\text{Br}_2\text{I}]$ employed, however, was independent of the methylation. Comparing the XP spectra of the methylated IL to that of the unmethylated IL, figure 3.12, no difference in peak shape or position is observed. Overall, the efficiency of Au corrosion was found to be very similar for $[\text{C}_6\text{C}_1\text{Im}][\text{Br}_2\text{I}]$ and $[\text{C}_4\text{C}_1\text{C}_1\text{Im}][\text{Br}_2\text{I}]$.

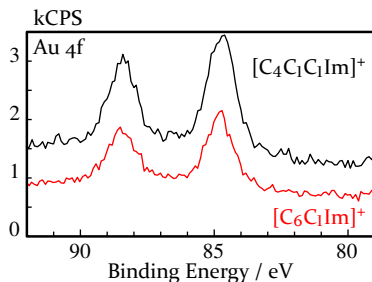


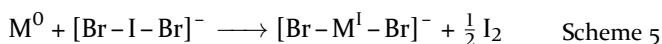
Figure 3.12.: Au 4f spectra of $[\text{C}_4\text{C}_1\text{C}_1\text{Im}][\text{Br}_2\text{I}]$ after exposure to a gold foil, and the spectra of $[\text{C}_6\text{C}_1\text{Im}][\text{Br}_2\text{I}]$ after exposure to a gold foil for comparison.

3.6.3 Imidazolium vs. Sodium Counter Ion

Finally, whether the trihalide anion is able to dissolve gold without an imidazolium counter ion being present was tested. For this purpose, a saturated solution of an aqueous $\text{Na}[\text{Br}_2\text{I}]$ system was prepared by dissolving 25 mmol of NaBr and 13 mmol of IBr into 3.2 ml of deionised water (note that an excess of Br^- was provided to stabilise Au^{I} against disproportionation into Au^0 and Au^{II}). 305 mg of gold foil were then immersed for 24 h at room temperature in this highly concentrated solution. After rinsing and drying the remaining gold foil, a mass loss of 12 ± 1 mg was found, that is about 0.06 mmol of Au dissolved, proving that gold is moderately soluble under these circumstances. Note that about 1 ml of $[\text{C}_6\text{C}_1\text{Im}][\text{Br}_2\text{I}]$ or $[\text{C}_4\text{C}_1\text{C}_1\text{Im}][\text{Br}_2\text{I}]$ is able to dissolve at least ten times more gold within 6 h.

3.7 Conclusion

It has been shown by weight loss and XPS experiments that the trihalide ILs $[\text{C}_6\text{C}_1\text{Im}][\text{Br}_2\text{I}]$ and $[\text{C}_4\text{C}_1\text{C}_1\text{Im}][\text{Br}_2\text{I}]$ are able to effectively dissolve the group 11 metals copper, silver, and gold by forming M^{I} metal ions at the expense of iodine; this is in contrast to the situation with molybdenum, which is not attacked by the trihalide IL. Based on these experimental results, the following reaction mechanism of a group 11 metal M^0 with a $[\text{Br}_2\text{I}]^-$ anion is highly plausible:



with the iodine of the trihalide anion oxidising the metal atom to the +1 oxidation state. The reduced radical eventually recombines with another iodine radical to form dissolved I_2 , which is later removed under vacuum conditions due to its high vapour pressure. As will be shown in chapter 4, in the case of copper there is a fast comproportionation reaction between Cu^0 and Cu^{II} forming Cu^{I} , so it cannot be ruled out that Cu^{II} is initially formed during corrosion only to undergo a subsequent comproportionation. It is proposed that the M^{I} ion is stabilised by the two Br^- anions arranged in a linear fashion forming a $[\text{Br}-\text{M}^{\text{I}}-\text{Br}]^-$ anion complex, which is known, e. g. for Au^{I} -halide systems^{74,75}

This reaction mechanism explains our XP metal signals that correspond to oxidation state +1 in solution, the selective decrease of the iodine signals in XPS, and the release of iodine into the gas phase in the course of the reaction. The colour change from deep brown to black upon the immersion of the Cu, Ag, and Au foils into the trihalide IL is attributed to the formation of I_2 that remains dissolved under ambient pressure, but is lost under vacuum. The latter process is evidenced by gas phase analysis and by the decolouration of the IL film on the sample holder after degassing. In the case of copper, the black colour likely also comes from the formation of $\text{Cu}^{\text{II}}\text{Br}_2$ that then undergoes a comproportionation reaction with metallic copper to form a Cu^{I} species. According to the proposed reaction mechanism, the amount of bromine remains essentially constant, as confirmed by XPS. The fact that the Br 3d XP signals from the trihalide IL before and after corrosion do not exhibit new signals at different binding energy – which should be visible as significant peak shape changes – clearly supports the proposed idea that the bromine atoms remain in the anionic $[\text{Br}-\text{M}^{\text{I}}-\text{Br}]^-$ complex with the negative charge delocalised. The formation of free bromide (Br^-)

and free iodide (I^-) anions can be ruled out by XPS because of their very different binding energy positions.

For the most inert metal, Au, experiments with both a carefully dried IL under dry N_2 and in the presence of excess water, showed no significant differences in the corrosion efficiency, ruling out a significant influence of water. Moreover, the similar corrosion rate of gold by $[C_4C_1Im][Br_2I]$ compared to the non-methylated $[C_6C_1Im][Br_2I]$, and the lack of significant spectral changes in the cation-related XPS peaks reveals that the imidazolium C2 proton is not involved. This conclusion was confirmed by NMR of the $[C_6C_1Im][Br_2I]$ IL after gold corrosion, which showed no indication of a Au^I -carbene complex. Finally, the poor ability of a highly concentrated $Na[Br_2I]$ aqueous solution to corrode metallic gold indicates that the imidazolium cation is not an innocent counter-cation but plays an important role in the dissolution of the anionic M^I complex. The imidazolium cation is not unique in this respect, as Li et al. have demonstrated.⁶³

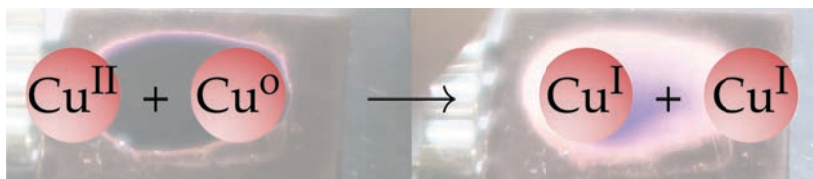
In particular, the fact that the trihalide ionic liquids oxidise gold to a stable +1 oxidation state, even in the presence of excess water, is noteworthy. Au^I is known to be relatively unstable in aqueous solution unless there is a sufficient concentration of halide ions and a low enough pH to maintain a stable complex, and will disproportionate to Au^0 and Au^{III} otherwise.^{78,79} It is tempting to speculate that there is a stabilising solvation shell provided by the imidazolium cations around the $[AuBr_2]^-$ complex, making the imidazolium trihalide IL suitable for the corrosion process. This ability is apparently not unique to the imidazolium cation, according to the results of Li et al.⁶³ Here, further experimental evidence such as crystal structure investigations and tests using ILs with other cations are needed, which is, however, out of the scope of this study.

The lack of molybdenum mass loss in our corrosion experiments, the lack of molybdenum signals in XPS, and the lack of volatile I_2 in the gas phase clearly demonstrate that the less noble metal molybdenum is virtually inert against attack by the trihalide IL. Most likely, the surface of this refractory metal becomes rapidly passivated on contact with the trihalide IL preventing further dissolution. To elucidate the nature of molybdenum passivation, more experiments are foreseen in the future.

To conclude, we believe that our study could be quite relevant for future applications. The most obvious one would be using the investigated trihalide ILs as an etching medium for microfabrication and even

as a leaching medium to dissolve precious group 11 metals from metal waste, e. g. electronic devices. For metal recovery from electronic waste, $[\text{Br}_2\text{I}]^-$ may be more suitable than $[\text{Cl}_3]^-$, since the dibromiodide is apparently a less powerful halogenating agent, meaning that less halogenated organic waste is likely to be formed. One could also envisage recovering the metals by appropriate electrochemical processes. Due to their low vapour pressure, the handling of the trihalide ILs promises to be safer than that of oxidising halogens or using CN-based aqueous chemistry. Finally, the formation of stable and water-insensitive Au^{I} complexes in an ionic liquid medium may also opens new possibilities for Au^{I} catalysis.

4 Comproportionation of Copper(II) Bromide in the Ionic Liquid 1-hexyl-3-Methylimidazolium Bromide



4.1 Introduction

In chapter 3, no evidence of the trihalide IL dissolving copper as a copper(II) species could be detected in XPS. However, from the measurements presented, it is not possible to rule out the initial formation of a copper(II) species that then undergoes a comproportionation reaction with the copper foil to form a copper(I) species:



Such a comproportionation reaction is well known in aqueous solution^{19,80} – for example, acidic aqueous copper(II) chloride is a copper etchant used in printed circuit board manufacture.⁸⁰ One of the advantages of copper(II) chloride over other etchants is that the Cu^{II} needed for the etching process can be easily regenerated by one of several methods.⁸⁰ The comproportionation reaction central to this process has been studied by electrochemical means in both aqueous solution^{19,81} and in deep-eutectic solvents.^{82,83} These studies also demonstrate that the reaction can be reversed.

In applying XPS to the study of oxidation state changes of transition metals, it is necessary to have some method of distinguishing different

oxidation states. In the case of copper, there are three oxidation states commonly encountered: Cu^0 , Cu^{I} and Cu^{II} . In this study, we are concerned with distinguishing between Cu^{I} and Cu^{II} . These two oxidation states can be distinguished by their differing peak positions, the different peak FWHM, and the relative intensities of their shake-up structures. Cu^0 and Cu^{I} both give rise to fairly narrow peaks, with the Cu^{I} peak appearing at *ca.* 0.5 eV lower binding energy than Cu^0 and exhibiting nearly no shake-up.⁷² Distinguishing copper(II) and copper(I) is made easy by the fact that the Cu^{II} peak is significantly broader (by a factor of ~ 3), appears at a higher binding energy (by ~ 1.5 – 2.5 eV), and has a large shake-up feature.⁷²

4.2 Methods and Materials

To study the potential comproportionation reaction, an ionic liquid solution (called the Cu^{II} solution in the following) was prepared by mixing 0.962 g of copper(II) bromide (CuBr_2 , 99 %, Alfa Aesar) with 2.118 g of 1-hexyl-3-methylimidazolium bromide ($[\text{C}_6\text{C}_1\text{Im}]\text{Br}$, purity 99 %, purchased from IoLiTec and used without further processing) to form a solution with a nominal $1 \text{ Cu}^{2+} : 2 [\text{C}_6\text{C}_1\text{Im}]^+$ molar ratio. A second solution containing both Cu^{II} and Cu^{I} (called the $\text{Cu}^{\text{I}}/\text{Cu}^{\text{II}}$ solution in the following), used to demonstrate that the two oxidation states can be distinguished by XPS, consisted of 6.604 g of $[\text{C}_6\text{C}_1\text{Im}]\text{Br}$ mixed with 2.240 g of copper(II) bromide and 0.479 g of copper(I) bromide (CuBr , ≥ 98 %, Honeywell). This is nominally a $1 \text{ Cu}^+ : 3 \text{ Cu}^{2+} : 8 [\text{C}_6\text{C}_1\text{Im}]^+$ ratio. Both solutions were shaken vigorously to mix the ingredients.

For the initial XPS analysis, a drop of the each solution was smeared onto a reservoir of dimensions $14 \times 20 \times 0.5$ mm milled into a molybdenum sample holder. The sample was pumped down overnight in the ESCA load lock, and then subjected to XPS analysis.

For the comproportionation reaction study, a thin (*ca.* 0.1 mm) layer of the Cu^{II} solution was spread over a section of copper foil (0.1 mm thickness, >99.99 %, MaTeck). Immediately after putting the IL on the foil, the sample was introduced into the chambers load lock and pump-down began. After a two hour pump-down period (about as fast as was possible), the sample was transferred to the Sample Preparation Chamber. The scan was started less than 5 min after transfer to the main chamber.

To test for long-term stability of the Cu^{II} solution on copper in air, the sample was removed from the vacuum chamber, and left covered but exposed to the air for 32 d. The sample was then pumped-down overnight and subjected to XPS analysis again.

Spectra were collected in normal emission and were analysed with CasaXPS. They were charge-corrected such that the C_{alkyl} peak appeared at 284.8 eV. For fitting the non-metal peaks, Shirley backgrounds and 30% Lorentzian pseudo-Voigt peaks were used. For the C 1s spectra, a model with two peaks (C_{alkyl} and C_{hetero}) was applied, with the full width at half maximum of the C_{hetero} peak constrained to $1.1 \times$ that of the C_{alkyl} peak. For the copper peaks, a W-Tougaard background and 80% Lorentzian pseudo-Voigt peaks were used. The Tougaard background was chosen to better capture the intensity of the Cu $2p_{3/2}$ shake-up structure. For both metal and non-metal spin-orbit doublets, the components were constrained to have the same full width at half maximum and the expected peak area ratio (e. g. 2 : 3 for $d_{3/2} : d_{5/2}$).

To compare the etching caused by the trihalide IL $[\text{C}_6\text{C}_1\text{Im}][\text{Br}_2\text{I}]$ to that caused by the Cu^{II} solution prepared above, two copper foils were cleaned with P4000 grit carbide paper before being rinsed with acetone. The two foils were then placed in either the Cu^{II} solution prepared above or the $[\text{C}_6\text{C}_1\text{Im}][\text{Br}_2\text{I}]$, discussed in chapter 3, such that half of the foil was in contact with the solution. After 16 h, the foils were taken out and rinsed with acetone, then mounted on aluminium sample stubs for scanning electron microscopy (SEM). The foil corroded by the trihalide was subsequently sonicated in acetone for 5 min, and again mounted and subjected to SEM. The SEM parameters used were an EHT voltage of 15 kV and an I_{probe} of 20 pA.

4.3 Visual Changes

Initially, both of the solutions had a deep, nearly black, purple colour. On molybdenum, this colour appeared unchanged for at least a week in both vacuum and in lab air. On copper, there was a progressive loss of colouration, eventually leading to a near-colourless liquid with diffuse wisps or patches of purple. The initial loss of colour was quickly obvious, but full loss of colour took several days for both solutions.

The Cu^{II} solution, which was spread over the copper foil with a glass rod, showed an initial rapid loss of colour apparent in the thinner sections of the IL. This initial loss of colour was apparent after the 2 h

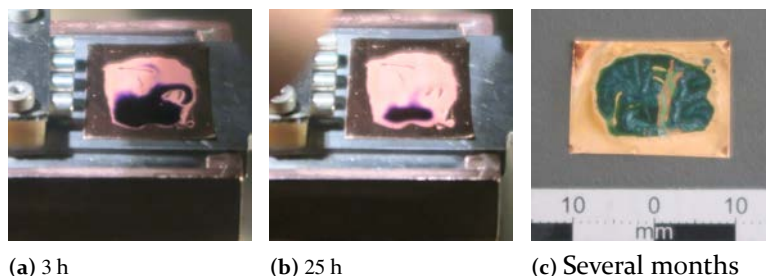


Figure 4.1.: Photographs (taken through a chamber window) of the Cu^{II} solution 3 h, 25 h after being placed on a copper foil, and after several months in air. Note that the appearance (in (a) and (b)) of the dark border and lighter central patch covered with liquid was only due to lighting conditions.

pump-down (figure 4.1 shows the sample after the 1 h scan sequence), and progressed over the course of several days, figure 4.1.

Over the 32 d exposure to air, the sample initially (over the course of 2–5 d) formed small black specks, then formed a dirty turquoise coloured solid. This colouration persisted for a number of months, figure 4.1.

4.4 XP Spectra of the Cu^{II} Solution

The XP spectra of the Cu^{II} solution are shown in figures 4.2 (non-metal signals) and 4.3 (metal signals). The N 1s region of the solution on molybdenum (figure 4.2) shows a small anomalous extra peak at 398.7 eV – correlated with an extra peak seen in the survey spectra at approximately 232 eV, this extra peak originated from a Mo $3p_{3/2}$ signal. The extra N 1s peak at 398.7 eV is thus attributed to a contamination from the (non-sputtered) molybdenum sample holder. The C 1s spectra shows an excess of alkyl carbon, table 4.1, indicating some hydrocarbon contamination, which most likely also stems from the sample holder. The separation of the C_{alkyl} and C_{hetero} peaks is 1.6 eV for all three scans. There is also a major amount of oxygen present, seen as two peaks at 530.6 eV and 532.3 eV, which correspond to native molybdenum oxide⁵⁵ and recalcitrant water respectively. The amount of bromine present is within the expected range, table 4.1. Interestingly, the Br 3d spectra of

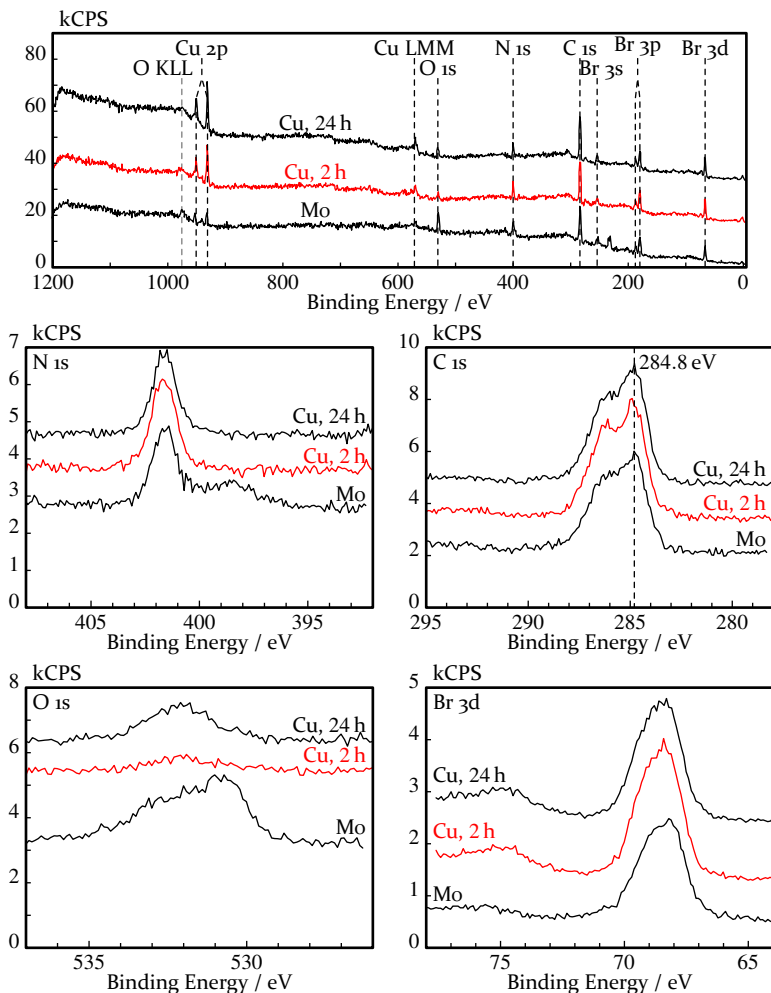


Figure 4.2.: Non-metal peaks and survey spectra of the Cu^{II} solution on a molybdenum support and on copper foil (2 h and 24 h after introduction to the XPS chamber).

the Cu^{II} solution on copper show a satellite structure at ~ 75 eV, similar to that seen for the trihalide anion $[\text{Br}-\text{I}-\text{Br}]^-$ in the IL $[\text{C}_6\text{C}_1\text{Im}][\text{Br}_2\text{I}]$ (section 2.3.2, chapter 2), and for the trihalide IL used to corrode a

4 Comproportionation of Copper(II) Bromide in an Ionic Liquid

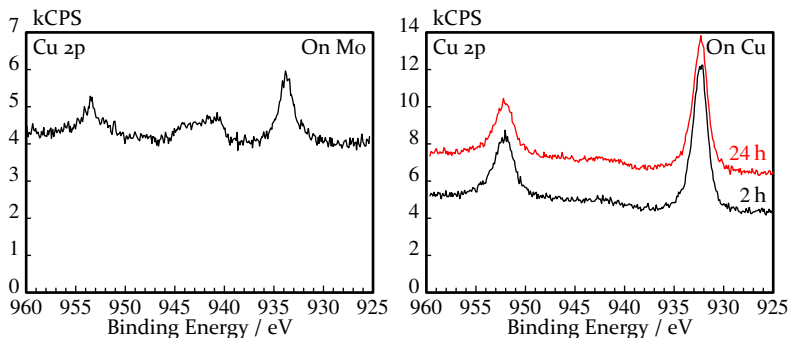


Figure 4.3.: Metal peaks of the Cu^{II} solution, on molybdenum (left) and on copper (right).

copper foil (figure 3.5, chapter 3). For the trihalide IL, this satellite structure was explained as a consequence of charge delocalisation over the $[\text{Br}-\text{I}-\text{Br}]^-$, and this explanation would seem to apply here, with the Cu^{I} cation (but apparently not the Cu^{II} cation) forming a charge-delocalised complex with the bromide anions.

The Cu 2p spectra of the Cu^{II} solution on Mo, figure 4.3, shows the expected spin-orbit doublet and shake-up structure (the shake-up structure of the $2p_{1/2}$ branch is outside the scan window). The $2p_{3/2}$ branch appears at 933.7 eV. There is no other set of peaks apparent, indicating that all copper is present in the copper(II) oxidation state.

The Cu 2p spectra of the Cu^{II} solution on the copper foil (figure 4.3) shows only a spin-orbit doublet after 2 h. In addition, there is a peak shift (compared to the solution on molybdenum) of -1.4 eV to 932.3 eV. There are no significant differences between the 2 h scan and the scan at 24 h, figure 4.3. The shift to lower binding energy and the lack of a shake-up structure are both indicative of the formation of a Cu^{I} species – which is the expected product of the $\text{Cu}^{\text{II}}/\text{Cu}^0$ comproportionation reaction – and the lack of further spectral changes after 2 h shows that the reaction is largely complete after after 2 h.

	C 1s	alkyl : hetero	O 1s	N 1s	Br 3d	Cu 2p _{3/2}	Cu ^{II}
RSF →	0.208		0.599	0.364	0.551	5.77*	%
1:2 Nominal	10	5 : 5	0	≡ 2	2	0.5	100
Mo, Overnight	13.6	7.5 : 6.1	2.8	≡ 2	2.1	0.3	105
Cu, 2 h	11.3	5.2 : 6.1	0.3	≡ 2	1.8	0.5	0
Cu, 24 h	12.8	7.2 : 5.6	1.0	≡ 2	2.0	0.6	0
Cu, Air Exposed	20.6	12.5 : 6.0 + 2.0 [†]	4.8	≡ 2 + 1.3 [‡]	2.3	1.8	103

Table 4.1.: Composition of the ILs studied, as measured by XPS. Values are normalised such that N 1s due to imidazolium is ≡ 2. *RSF is $\frac{2}{3} \times$ of the measured value for Cu 2p. [†]Suspected carbonyl carbon signal. [‡]Extra peak, not counted as an imidazolium peak for normalisation.

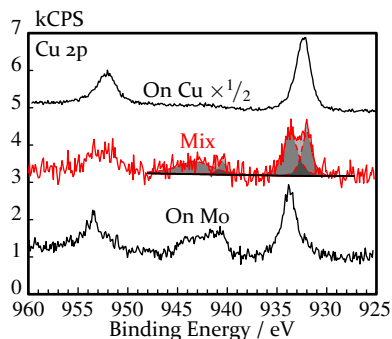


Figure 4.4.: Cu 2p spectra of of the Cu^{II} solution on Mo and Cu (black), and the $\text{Cu}^{\text{I}}/\text{Cu}^{\text{II}}$ solution on Mo (red).

differences between the two oxidation states are similar to those reported for solid copper salts,⁷² as expected.

The quantification in table 4.1 reveals that the total amount of copper present on molybdenum is lower than expected – 0.3 atoms as opposed to the expected 0.5 atoms – note that the quantification in table 4.1 includes the $\text{Cu } 2p_{3/2}$ shake-up structure. The amount present doubles on contact with the copper foil, as expected from the comproportionation reaction (which when complete should result in 1.0 atoms), but it does appear that there is still a systematic under-estimation of the amount of copper present. The cause of this under-estimation is unclear.

The visual changes, increase in the amount of copper in solution, and more significantly the spectral differences between the Cu^{II} solution before (on Mo) and after contact with copper, are clear evidence that the comproportionation reaction given in scheme 6 has occurred, resulting in a solution containing only Cu^{I} . Further, the fact that the reaction is largely complete (i. e. no significant amounts of Cu^{II} can still be detected) after only 2 h illustrates that this is a relatively fast reaction. The lack of any significant spectral change after 24 h confirms that the reaction is mostly complete after only 2 h – the continued visual changes noted above are most likely due to Cu^{II} being a strong colour-centre, meaning that even low concentrations below the detection limit of XPS can lead to visible colouration.

To confirm the XPS systems ability to differentiate between Cu^{I} and Cu^{II} in ionic liquid solution, figure 4.4 shows a comparison of the Cu 2p of the Cu^{II} solution and the $\text{Cu}^{\text{I}}/\text{Cu}^{\text{II}}$ solution. The main $2p_{3/2}$ peaks are separated by 1.6 eV in the scans of the $\text{Cu}^{\text{I}}/\text{Cu}^{\text{II}}$ solution, compared to the 1.4 eV shift observed for the Cu^{II} solution on Mo and Cu. The shake-up observed for the Cu^{II} solution on Mo is also seen for the $\text{Cu}^{\text{I}}/\text{Cu}^{\text{II}}$ solution. XPS can easily distinguish between Cu^{II} and Cu^{I} in IL solution, and the spectral

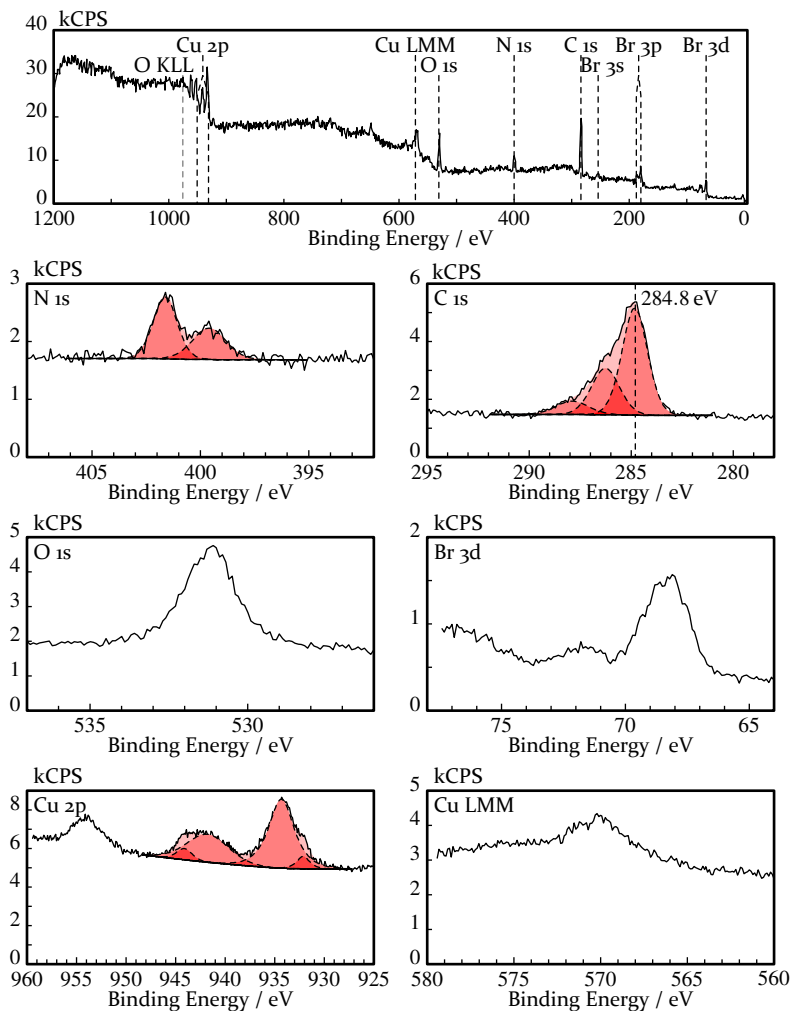


Figure 4.5.: Region and wide spectra of the Cu^{II} solution on copper after 32 d in air.

XPS reveals clear evidence that the Cu^{II} solution undergoes a rapid comproportionation reaction when in contact with metallic copper (leaving Cu^{I} in solution), and no significant changes occur over a 24 h under vacuum. To test if the post-comproportionation solution will re-

oxidise in air, the Cu^{II} solution on the copper foil was removed from the vacuum chamber and left in air for 32 d. Aside from the visual changes noted above, we observe several spectral and compositional changes after 32 d in air. In the C 1s region, a third carbon peak appeared at 287.9 eV, figure 4.5, and the amount of alkyl carbon greatly increased (from 7.2 atoms to 15.5 atoms, table 4.1). There is also an additional N 1s peak at a (399.6 eV, cf. 398.7 eV for the Mo 3p_{3/2} peak seen in the on-Mo scans), and with a significant intensity (table 4.1). The position of the imidazolium peak is the same as measured for the Cu^{II} solution on copper and molybdenum (401.6 eV for all scans). The O 1s signal also changes – it greatly increased in intensity and shifted to a lower binding energy of 531.2 eV, compared to 531.9 eV for the 2 h on-copper sample. Changes are also apparent in the Br 2p peak, there is a shift to lower binding energy of –0.3 eV, and a small satellite feature at 71.7 eV. The Cu 2p region shows a large shake-up feature, and a 2p_{3/2} peak position of 934.3 eV, which is 0.6 eV higher than that of the Cu^{II} solution on molybdenum (933.7 eV).

The copper peaks clearly show that in air, the Cu/IL solution (and likely the copper foil underneath) has significantly oxidised. The colour is similar to basic copper carbonate (Cu^{II}₂(OH)₂CO₃), and it is known that metallic copper will form a basic copper carbonate patina, albeit on a much longer time scale than 32 d. However, the formation of a carbonate is not supported by the spectra: the new carbon peak is at a binding energy significantly below the typical carbonate range (289–291.5 eV⁵⁵) – the peak position is closer to that of a typical carbonyl species (287.1–288.1 eV⁵⁵) or an amine species (285.2–288.4 eV⁵⁵). Combined with the large increase in the amount of alkyl carbon seen after 32 d, it is concluded that the new carbon peak is likely the result of carbonaceous contamination. Although the O 1s peak is within the expected range for a carbonate (530.5–531.5 eV⁵⁵), the lack of a corresponding carbonate C 1s peak rules out this possibility. The peak position is consistent with a hydroxide species, or with dissolved water.⁵⁵ The nitrogen contamination could be due to the carbonaceous contamination noted above (it is in the right range for a neutral amide or nitrogen in an organic matrix⁵⁵), but this cannot be confirmed from these measurements.

From the changes in the Cu 2p spectra, it is clear that the copper re-oxidised in air. What is less clear is which of the other changes are due to contamination and which are due to the reaction with air – there-

fore any conclusions about the chemical processes occurring on contact with air should be treated with caution. Any more definite conclusions would require repeating the experiment under more well-defined conditions.

4.5 SEM of Corroded Copper Foil

The scanning electron micrographs of the copper foil partly immersed in the Cu^{II} solution are given in figure 4.6, and show that there is a clear difference between the corroded and uncorroded sections (labelled A and C in figure 4.6, respectively). Whereas the uncorroded section appears quite smooth, with scratches (made by the carbide paper during cleaning) being the only significant surface features visible, the corroded section clearly has a rough texture. No etching pits are apparent. It is also apparent that there is an intermediate section (labelled B in figure 4.6) between the corroded and uncorroded sections – this is the meniscus line, where only a very thin film of the IL was present. This area appears to be slightly less rough than the corroded section, indicating that in this region, the corrosion did not progress as quickly as the fully immersed section.

Figure 4.7 shows the scanning electron micrographs of the copper foil extensively corroded by $[\text{C}_6\text{C}_1\text{Im}][\text{Br}_2\text{I}]$. As with the foil corroded by the Cu^{II} solution, there is a clear difference between the exposed and unexposed sections in terms of surface roughness. The unexposed section is still quite smooth, with the same scratch lines as were seen before, whereas the exposed section shows significant roughness, with many etching pits apparent. Note that etching pits were also observed when a gold foil was exposed to the trihalide IL, figure 3.3 in chapter 3. Note that the trihalide IL was aggressive enough to completely dissolve a section of the copper foil, and in the micrographs presented in figure 4.7 the adhesive carbon pad can be seen.

Examining the micrographs of the unexposed section, we see a large variance in secondary electron yield – the position of this variance corresponds with the position of the patina visible on the foil, even after sonication (figure 4.7). It appears that iodine, formed during the etching reaction, evaporated from the IL and reacted with the clean copper surface not in contact with the IL.

From these micrographs, it is clear that the trihalide IL is a more aggressive etchant than the Cu^{II} solution, but also that the volatility of the

iodine produced by the trihalide IL during etching is a potential issue, as is the etching pitting.

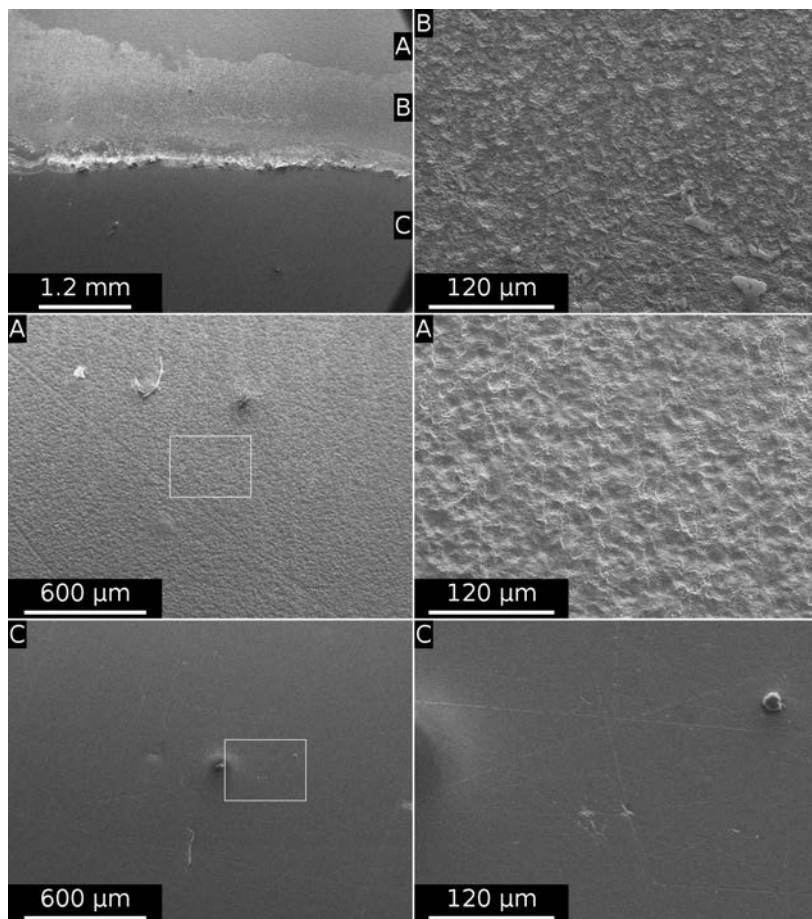


Figure 4.6.: SEM micrographs of a copper foil partly immersed in the Cu^{II} solution, with the corroded (A), partly-corroded (B), and uncorroded (C) areas indicated.

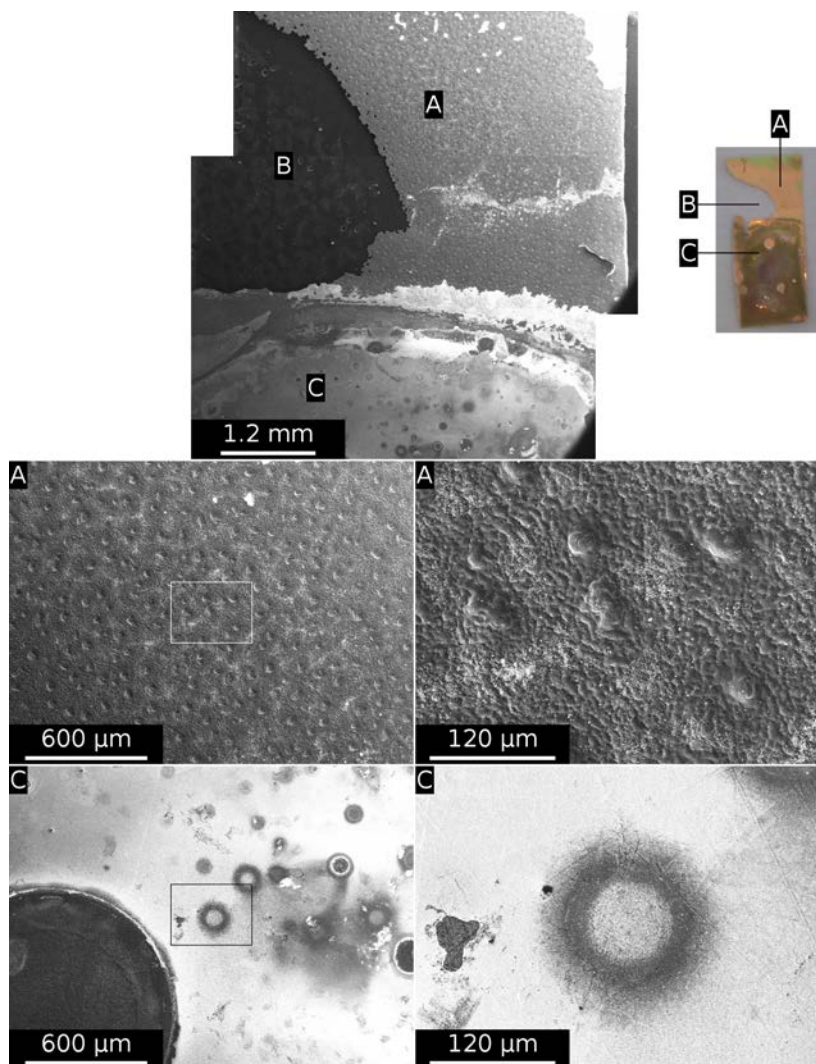


Figure 4.7.: SEM micrographs of a copper foil partly immersed in $[\text{C}_6\text{C}_1\text{Im}][\text{Br}_2\text{I}]$ taken post-sonication, with magnified views of the corroded (A), and uncorroded (C) sections. The adhesive carbon pad (B) is visible through the foil. A photograph of the foil post-sonication is also shown.

4.6 Conclusion

A solution of $\text{Cu}^{\text{II}}\text{Br}_2$ in $[\text{C}_6\text{C}_1\text{Im}]\text{Br}$ was prepared, and characterised by XPS on both molybdenum and copper. On copper, the rapid (ca. 2 h) comproportionation reaction $\text{Cu}^{\text{II}} + \text{Cu}^0 \longrightarrow 2\text{Cu}^{\text{I}}$ was observed, resulting in the complete conversion of the Cu^{II} salt to a Cu^{I} salt. Visually, this reaction was accompanied by a loss of colour, which is expected since Cu^{II} is a strong chromophore and Cu^{I} is generally colourless. This reaction was not observed on molybdenum. The XP spectra of a solution of $\text{Cu}^{\text{II}}\text{Br}_2$ and $\text{Cu}^{\text{I}}\text{Br}$ in $[\text{C}_6\text{C}_1\text{Im}]\text{Br}$ confirmed that the species detected in the scans of the Cu^{II} solution on copper is a Cu^{I} species. SEM examination of a copper foil etched by the Cu^{II} solution shows an increase in surface roughness (consistent with etching taking place), and a notable absence of etching pits, especially when compared to a copper foil similarly etched by the trihalide IL $[\text{C}_6\text{C}_1\text{Im}][\text{Br}_2\text{I}]$. Additionally, the effect of air on a sample on copper that had undergone the comproportionation reaction was probed by XPS. Although a large amount of contamination prevents any detailed conclusions, we have also shown that when left in air, the Cu^{I} solution formed after the comproportionation reaction will reoxidise to form a Cu^{II} -containing solution. Visual changes are apparent, with the air-exposed sample turning a turquoise colour.

5 Summary

In this thesis, studies involving ionic liquids (ILs) in the context of IL-transition metal reactions were reported on: the thermochromatic transformation of a cobalt thiocyanate-containing IL, the characterisation of polyhalide ionic liquids, the corrosion of group 11 metals by trihalide ILs, and the comproportionation of copper metal and Cu^{II} salts in solution. X-ray photoelectron spectroscopy (XPS) was the main technique used in all of these studies, but other techniques such as mass spectrometry (MS) and scanning electron microscopy (SEM) were also used.

In chapter 1, the thermochromatic complex-ligand equilibrium of a cobalt thiocyanate-based IL was studied. One major finding was that, in the near-surface region, the transition temperature is approximately 30°C higher than in the bulk. Angle-resolved XPS showed that the free thiocyanate anions at the surface of the thermochromatic IL orient themselves pointing outwards, towards the vacuum. It was proposed that this surface-ordering was the main reason for the higher transition temperature: in the bulk, the transition

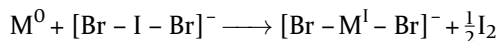


is a disorder \rightarrow order transition, whereas in the near-surface region it's a semi-order \rightarrow order transition. In the near-surface region, the entropy change associated with this transformation is thus lower in absolute value, resulting in the lower transition temperature. Additionally, an apparent dilution of the cobalt complex accompanying the coordination number increase was observed, which was attributed to the formation of a weakly bound secondary solvation shell of $[\text{SCN}]^-$.

Before investigating the corrosion of metals by trihalide ionic liquids, a study of several polyhalide ILs was made and was reported in chapter 2. Four polyhalide ILs were prepared by mixing $[\text{C}_6\text{C}_1\text{Im}]\text{X}$ ($\text{X} = \text{Cl}^-$,

Br^- , I^-) with dihalogens: $[\text{C}_6\text{C}_1\text{Im}][\text{BrI}_2]$, $[\text{C}_6\text{C}_1\text{Im}][\text{Br}_2\text{I}]$, $[\text{C}_6\text{C}_1\text{Im}][\text{Cl}_2\text{I}]$, and $[\text{C}_6\text{C}_1\text{Im}][\text{Br}_3\text{I}]$. All were found to be weakly basic, seen in XPS as a low degree of charge transfer leading to higher binding energy positions for the C_{hetero} and imidazolium N 1s peaks. The anion $[\text{Br}_2\text{I}]^-$ was found to be generally stable under vacuum, although a noticeable loss of iodine was found after 70 h; the vacuum stability could be increased by adding one molar excess of bromide, to form the new polyhalide species $[\text{Br}_3\text{I}]^-$. XPS showed that while iodine was lost, bromine was not; mass spectrometry confirmed that the halogen species off-gassed was molecular iodine, I_2 , and not the starting interhalogen or bromine. The implication is that the polyhalide interconversion equilibria that occur in aqueous and organic solution⁵⁹ also occur in IL solution. The diiod-obromide IL was found to be vacuum-unstable, rapidly losing iodine under vacuum.

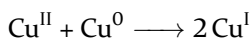
With the IL $[\text{C}_6\text{C}_1\text{Im}][\text{Br}_2\text{I}]$ characterised, the corrosion of the group 11 metals copper, silver, and gold was reported on in chapter 3. $[\text{C}_6\text{C}_1\text{Im}][\text{Br}_2\text{I}]$ was found to effectively dissolve all three of these metals, as confirmed by both XPS and mass loss measurements. SEM of gold after corrosion revealed etching groves and pits. At the same time, molybdenum was found to be corrosion-resistant. From the XPS measurements, all of the group 11 metals dissolved as M^1 species, however for copper an initial formation of a Cu^{II} species followed by a rapid comproportionation to Cu^1 could not be ruled out. XPS also showed that iodine was lost on corrosion, whilst bromine wasn't. This was confirmed by vapour-phase MS, which showed that molecular iodine is the only halogen species off-gassed during corrosion. Further, the peak shifts observed in XPS for the bromide present is consistent with the formation of the linear complex $[\text{Br}-\text{M}-\text{Br}]^-$, where the charge of the bromide ligands is delocalised across the complex. From these results, the corrosion mechanism



was proposed. Experiments where gold was corroded by dried or water-saturated trihalide IL showed that water has no effect on the corrosion rate or corrosion product. Additional corrosion experiments with $[\text{C}_4\text{C}_1\text{C}_1\text{Im}][\text{Br}_2\text{I}]$ showed that methylating the imidazolium cation at the C_2 position did not change the corrosion product, and corroborating NMR measurements of the $[\text{C}_6\text{C}_1\text{Im}]^+$ -based trihalide IL rule out

carbene formation in the course of the gold corrosion process. However, the imidazolium cation does still play a role in corrosion. Exposing gold to a saturated aqueous solution of Na[Br₂I] revealed some corrosion, however, at a considerably lower rate than that seen for the trihalide IL. It appears that the imidazolium does stabilise the metal complex formed on dissolution. Imidazolium-based cations are not unique in this regard, as Li et al. have recently demonstrated metal corrosion (including group 11 metals) by tetraalkylammonium, phosphonium, pyridinium, and pyrrolidinium based ILs.⁶³

As stated above, the experiments carried out in the trihalide corrosion chapter could not rule out the formation of an intermediate Cu^{II} species that subsequently undergoes a fast comproportionation reaction. Such a reaction was the subject of chapter 4, where a solution of CuBr₂ in [C₆C₁Im]Br in contact with metallic copper was studied by XPS. The comproportionation reaction



was observed on copper, and no analogous reaction was seen on molybdenum. This reaction was fast, running to near-completion within about 2 h. Reference measurements with a mixed Cu^I/Cu^{II} solution demonstrated the large differences between the XP spectra of the two oxidation states. An SEM comparison of copper foils corroded by the CuBr₂ in IL solution and by [C₆C₁Im][Br₂I] revealed that whilst both are effective at dissolving the copper, the Cu^{II} solution was less aggressive, and unlike the trihalide IL, did not lead to the formation of etching pits, or the staining of non-immersed parts by iodine vapours.

The use of ILs as oxidative solvents for transition metals is still a relatively new concept. Although corrosion in ionic liquids and molten salts has been of interest in the past, using ionic liquids (particularly polyhalide-based ILs) as enchants or leachants is a new approach where not much work has been published. Considering the results presented in this thesis and by Li et al.⁶³, it appears that in general trihalide ILs are oxidative solvents for a range of transition metals, however not all trihalides are equal. In the Li publication, trichloride was found to halogenate imidazolium cations [C₄C₁Im]⁺ and [C₁₀C₁Im]⁺ whereas in this study, no halogenation of the imidazolium cation was observed. This suggests that the [Br₂I]⁻ anion used here is less a powerful halogenating agent than the [Cl₃]⁻ anion, however it is still able to oxidise the noble metal gold. For certain applications (such as metal recovery from

scrap) the chlorination of organic material may be undesirable, since chlorinated organic material would need to undergo special processing for disposal, thus dibromiodide may be advantageous.

In IL solution, it appears that the presence of the outer surface generally has an impact on the first few nanometres: in chapter 1, a notable dilution of the cobalt complex in the near-surface region was observed on formation of the $[\text{Co}[\text{NCS}]_6]^{4-}$ complex, and in chapter 3, the amount of copper in solution as measured by XPS was lower than would be expected from the mass change measurement. A reduced amount of metal dissolved in the near-surface region was also observed for the solutions made in chapter 4; note that for the corrosion experiments, the net mass loss is not necessarily the same as the mass of metal that ultimately dissolved in solution, and that this uncertainty was avoided in chapter 4 because the copper salt was directly weighed out. Conversely, for the gold corrosion experiments, XPS reported slightly more gold than one would have expected from the mass change measurements. It is tempting to speculate that these findings indicate a near-surface effect, where-by light transition metal ions preferentially deplete from the surface while heavy metal ions show surface enrichment in IL solutions. However, larger and more systematic studies are required to support this concept.

6 Zusammenfassung

In Rahmen dieser Doktorarbeit wurden Untersuchungen an ionischen Flüssigkeiten (ILs) im Zusammenhang mit IL-Übergangsmetallreaktionen durchgeführt. Insbesondere wurden die thermochromatische Umwandlung einer Kobaltthiocyanat-haltigen IL, die Charakterisierung von Polyhalogenid ILs sowie die, Korrosion von Metallen der Gruppe 11 durch Trihalogenid-ILs und Komproportionierung von Kupfermetallen und Cu^{II} -Salzen in Lösung behandelt. Alle Untersuchungen wurde mittels Röntgenphotoelektronenspektroskopie (XPS) durchgeführt, welche durch andere Techniken wie Massenspektrometrie (MS) und Rasterelektronenmikroskopie (SEM) ergänzt wurde.

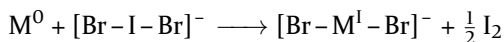
In Kapitel 1 wurde das thermochromatische Komplex-Liganden-Gleichgewicht einer auf Kobaltthiocyanat basierenden IL untersucht. Eine wichtige Erkenntnis ist, dass die Übergangstemperatur im oberflächennahen Bereich um etwa $30\text{ }^{\circ}\text{C}$ höher liegt als im Volumen. Winkelaufgelöstes XPS zeigte, dass sich die freien Thiocyanatanionen der thermochromatischen IL an der Oberfläche in Richtung des Vakuums orientieren. Es wurde geschlussfolgert, dass diese Oberflächenordnung der Hauptgrund für die höhere Übergangstemperatur ist: im Volumen ist der Übergang



ein Unordnungs/Ordnungs-Übergang. In der oberflächennahen Region ist es jedoch ein Übergang von einer Semiordnung zur vollständigen Ordnung. Die mit dieser Umwandlung einhergehende Entropieänderung ist somit niedriger, was zu einer niedrigeren Übergangstemperatur führt. Zusätzlich wurde eine Verdünnung des Kobaltkomplexes beobachtet, die mit der Erhöhung der Koordinationszahl einhergeht, was auf die Bildung einer schwach gebundenen sekundären Solvationschale von $[\text{SCN}]^-$ zurückgeführt wird.

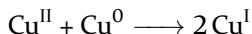
Bevor die Korrosion von Metallen durch Trihalogenid IL untersucht wurde, wurden in Kapitel 2 mehrere Polyhalogenid-ILs untersucht. Vier Polyhalogenid-ILs wurden durch Mischen von $[C_6C_1Im]X$ ($X = Cl^-$, Br^- , I^-) mit Dihalogenen hergestellt: $[C_6C_1Im][BrI_2]$, $[C_6C_1Im][Br_2I]$, $[C_6C_1Im][Cl_2I]$ und $[C_6C_1Im][Br_3I]$. Die Bindungsenergien der Kohlenstoffatome mit einem Hetero-Nachbaratom und des Imidazolium Stickstoffatoms wurden bei höheren Bindungsenergien detektiert, was auf einen geringeren Ladungsübergang und somit schwache Basizität aller hergestellten ILs schließen lässt. Das Anion $[Br_2I]^-$ war im Allgemeinen unter Vakuum stabil, obwohl nach 70 h ein merklicher Verlust an Jod festgestellt wurde. Die Vakuumstabilität konnte durch Zugabe eines ein-molaren Überschusses an Bromid erhöht werden, wobei eine neue Polyhalogenid-Spezies, $[Br_3I]^-$, gebildet wurde. XPS zeigte, dass der Bromanteil konstant blieb, während sich die Jodmenge verringerte. Massenspektrometrie bestätigte, dass die ins Vakuum übergehende Halogenspezies molekulares Jod, I_2 , und nicht BrI oder Br_2 waren. Das für wässrige und organische Lösungen⁵⁹ bekannte Polyhalogenid-Umwandlungsgleichgewicht tritt offensichtlich auch in IL-Lösung auf. Der rasche Verlust von Jod in der UHV Kammer zeigt, dass Diiodobromid IL im Vakuum instabil ist.

Mit der zuvor charakterisierten IL $[C_6C_1Im][Br_2I]$ wurde in Kapitel 3 die Korrosion der Metalle der Gruppe 11, Kupfer, Silber und Gold, studiert. $[C_6C_1Im][Br_2I]$ löste alle drei Metalle effektiv, was sowohl durch XPS- als auch durch Masseverlustmessungen bestätigt wurde. SEM-Messungen von Gold nach dem Korrosionsexperiment zeigten das Ätzen von Rillen und Mulden/Furchen. Im Gegensatz dazu wurde festgestellt, dass Molybdän korrosionsbeständig ist. XPS-Messungen zeigten, dass sich alle Metalle der Gruppe 11 als M^I -Spezies lösen. Die schnelle Komproportionierung von einer anfänglich gebildeten Cu^{II} - zu einer Cu^I -Spezies konnte nicht ausgeschlossen werden. XPS zeigte auch, dass Jod durch Korrosion verloren ging, während Brom erhalten blieb. Dies wurde durch Dampfphasen-MS bestätigt, das zeigte, dass molekulares Jod die einzige Halogenspezies ist, die während der Korrosion detektiert wurde. Die in XPS beobachtete Peakverschiebung für das vorhandene Bromid ist konsistent mit der Bildung des linearen Komplexes $[Br-M-Br]^-$, wobei die Ladung der Bromidliganden über den gesamten Komplex verteilt ist. Daraus ergibt sich der folgende Korrosionsmechanismus:



Experimente, bei denen Gold durch "wasserfreie" oder wassergesättigte Trihalogenid ILs korrodiert wurde, zeigten, dass Wasser keinen Einfluss auf die Korrosionsrate oder das Korrosionsprodukt hat. Zusätzliche Korrosionsexperimente mit $[\text{C}_4\text{C}_1\text{C}_1\text{Im}][\text{Br}_2\text{I}]$ ergaben, dass die Methylierung des Imidazolium-Kations an der C2-Position das Korrosionsprodukt nicht veränderte. Zusätzliche NMR-Messungen der auf $[\text{C}_6\text{C}_1\text{Im}]^+$ basierenden Trihalidid-IL bestätigten das Ausbleiben einer Carbenbildung im Verlauf des Goldkorrosionsprozesses. Dennoch spielte das Imidazoliumkation eine wichtige Rolle bei der Korrosion. Das Aussetzen von Gold gegenüber einer gesättigten wässrigen Lösung von $\text{Na}[\text{Br}_2\text{I}]$ führt zu etwas Korrosion, jedoch mit einer erheblich geringeren Rate als durch die Trihalogenid IL. Es wird vermutet, dass während des Korrosionsvorganges das Imidazoliumkation den gebildeten Metallkomplex stabilisiert. Imidazoliumkationen sind in dieser Hinsicht nicht einzigartig, da Li et al. kürzlich Metallkorrosion (einschließlich Metalle der Gruppe 11) durch Tetraalkylammonium-, Phosphonium-, Pyridinium- und Pyrrolidinium-basierte ILs⁶³ nachgewiesen haben.

Wie bereits erwähnt, konnten die in Kapitel 3 beschriebenen Experimente zur Trihalogenidkorrosion die Bildung einer intermediären Cu^{II} -Spezies mit anschließender schneller Komproportionierung nicht ausschließen. Eine solche Reaktion wurde in Kapitel 4 beschrieben, in welchem eine Lösung von CuBr_2 in $[\text{C}_6\text{C}_1\text{Im}]\text{Br}$ in Kontakt mit metallischem Kupfer mittels XPS untersucht wurde. Die Komproportionierungsreaktion



wurde für Kupfer beobachtet, wohingegen für Molybdän keine analoge Reaktion beobachtet wurde. Diese Reaktion verlief schnell und war innerhalb von 2 h fast vollständig abgeschlossen. Referenzmessungen mit einer gemischten $\text{Cu}^{\text{I}} / \text{Cu}^{\text{II}}$ -Lösung zeigten große Unterschiede zwischen den XP-Spektren der beiden Kupferoxidationszustände. Ein SEM-Vergleich von Kupferfolien, die durch CuBr_2 in IL-Lösung und durch $[\text{C}_6\text{C}_1\text{Im}][\text{Br}_2\text{I}]$ korrodiert wurden, belegte, dass beide beim Lösen des Kupfers wirksam sind. Jedoch war die Cu^{II} -Lösung weniger aggressiv und führte im Gegensatz zur Trihalogenid-IL nicht zur Bildung von Ätzgruben oder zur Anfärbung nicht eingetauchter Teile durch Joddämpfe.

Die Verwendung von ILs als oxidative Lösungsmittel für Übergangsmetalle ist noch ein relativ neues Konzept. Obwohl Korrosion in ionischen Flüssigkeiten und geschmolzenen Salzen in der Vergangenheit

von Interesse war, ist die Verwendung von ionischen Flüssigkeiten (auf Polyhalogenidbasis) als Ätzmittel oder Auslaugungsmittel ein neuer Ansatz, zu dem nur wenige Publikationen vorliegen. Die Ergebnisse dieser Arbeit und jener von Li et al.⁶³ zeigten, dass Trihalogenid-ILs im Allgemeinen oxidative Lösungsmittel für eine Reihe von Übergangsmetallen sind, jedoch besitzen nicht alle Trihalogenide die gleiche Stärke. In der Arbeit von Li et al. wurde gezeigt, dass das Trichlorid-anion Imidazoliumkationen wie $[C_4C_1Im]^+$ und $[C_{10}C_1Im]^+$ halogeniert, während in dieser Arbeit keine Halogenierung des Imidazoliumkations beobachtet wurde. Dies legt nahe, dass das hier verwendete $[Br_2I]^-$ -Anion ein weniger starkes Halogenierungsmittel als das $[Cl_3]^-$ -Anion ist, es jedoch immer noch in der Lage ist, das Edelmetall Gold zu oxidieren. Für bestimmte Anwendungen (wie Metallrückgewinnung aus Metallschrott) kann die Chlorierung von organischem Material unerwünscht sein, da chlorhaltiges organisches Material zur Entsorgung einer speziellen Behandlung unterzogen werden müsste, so dass Dibromjodid vorteilhafter wäre.

In IL-Lösungen scheint die Zusammensetzung der äußeren Oberfläche im Allgemeinen einen Einfluss auf die ersten Nanometer zu haben: In Kapitel 1 wurde eine bemerkenswerte Verdünnung des Cobaltkomplexes im oberflächennahen Bereich bei der Bildung des $[Co[NCS]_6]^{4-}$ -Konzentrats beobachtet, und in Kapitel 3 war die durch XPS gemessene Menge an Kupfer in Lösung niedriger als bei der Masseverlustmessung zu erwarten wäre. Auch in Kapitel 4 wurde eine geringere Menge des gelösten Metalls an der Oberfläche detektiert. Für diese Messungen wurden sowohl IL als auch die Kupfersalze direkt abgewogen, was eine sehr genaue Bestimmung der Volumenstöchiometrie ermöglichte. Andererseits ergaben die XPS-Messungen der Goldkorrosionsexperimente etwas mehr Gold als man von den Massenverlustmessungen erwartet hätte. Auch in diesem Fall wäre es möglich, dass Oberflächeneffekte eine Rolle spielen könnten: leichte Übergangsmetallionen scheinen bevorzugt von der Oberfläche abgereichert zu sein, wohingegen Schwermetallionen in IL-Lösungen eine Oberflächenanreicherung zeigen. Um dieses Konzept zu unterstützen, sind jedoch umfangreichere und systematischere Studien erforderlich.

A Preliminary investigations of High-Gold Content Ionic Liquids

A.1 Introduction

As was reported in chapter 3, Au^I solutions with a high gold content were obtained by corroding gold foils with dibromiodide ILs for 6 h at 40 °C. A prolonged exposure time (21 h in total) led to an increase in Au^I content indicating that equilibrium was not reached after 6 h. In addition to the foil experiments, initial corrosion studies using gold powder instead of gold foils were preformed (section A.2). As will be shown here by XPS analysis (section A.3), the increase in surface area due to the use of gold powder allowed a considerable increase in the amount of Au^I in solution to be achieved, close to the full conversion of the [Br-I-Br]⁻ anions of the starting trihalide ILs to [Br-Au^I-Br]⁻ anions (referred to as “saturated ILs” in the following). With these saturated ILs, preliminary experiments were carried out with respect to spontaneous gold plating onto metallic copper and zinc (section A.4), reaction with Cu^IBr for potential recovery of metallic gold via disproportionation of Au^I (section A.5), catalytic activity (section A.7), and an electrochemical characterisation by cyclic voltammetry (section A.8), along with a first characterisation by thermal gravimetric analysis and infrared spectroscopy (sections A.9 and A.10, respectively). These studies are far from being complete, but could serve as starting points for further investigations in the future.

A.2 IL Synthesis

The trihalide ionic liquid [C₆C₁Im][Br₂I] (**IL-1**) was prepared by mixing 10.214 g (41.323 mmol) of 1-hexyl-3-methylimidazolium bromide

(99 %, purchased from IoLiTec and used without further processing) with 8.545 g (41.318 mmol) of iodine monobromide (Sigma-Aldrich, 98 %) – a 1 : 1 molar ratio. After shaking to mix the ingredients, the resultant IL was a deep red-brown liquid, with a viscosity lower than that of the starting halide. Because trihalide ILs are potentially photounstable, for all experiments steps measures were taken to minimise the ILs exposure to light.

The second trihalide IL **IL-2**, $[C_4C_1C_1Im][Br_2I]$, was prepared by mixing 1.314 g (5.634 mmol) of dry 1-butyl-2,3-dimethylimidazolium bromide (IoLiTec, 99 %, used without further processing) with 1.175 g (5.681 mmol) of IBr – again 1 : 1 molar ratio. After weighing out the $[C_4C_1C_1Im]Br$, it was stored in an evacuated bell jar whilst the iodine monobromide was weighed out. When the two ingredients were mixed (in a mortar) the IL initially liquified, turning a deep red-brown colour. After mixing with the pestle, the mixture was placed in the evacuated bell jar again, where it solidified after a few minutes under vacuum. After grinding again, the product was an orange powder with a melting point in the range of 45–50 °C. This powder has not be observed to reliquefy. A sample of the IL was taken for XPS analysis.

The $[C_6C_1Im][AuBr_2]$ (**IL-3A**) was prepared by placing 2.042 g (4.50 mmol) of the **IL-1** prepared above into a glass vial. To this, 884 mg (4.49 mmol) of gold powder ($<1 \mu m$, MaTeck 3N+) was added, followed by a stirrer bar. The vial was heated by a water bath at 60 °C for 6 h, then at 40 °C for a further 18 h. A sample was taken for XPS analysis.

A second batch of $[C_6C_1Im][AuBr_2]$ (**IL-3B**) was made for the water splitting and gold recovery experiments, described below. The procedure was the same as above, with 2.896 g of the trihalide IL and 1.086 g of the gold powder being used. The same heating profile (temperatures, times) was used as for batch A. As an additional step to drive off any remaining I_2 , after the 24 h of heating, the IL was placed in a continually evacuated bell jar at room temperature for approximately 9 d.

The $[C_4C_1C_1Im][AuBr_2]$ (**IL-4**) was made by adding 831 mg (1.89 mmol) of the **IL-2** prepared above to a round bottom Schlenk flask. Then, 381 mg (1.93 mmol, a 2 % excess) of gold powder. The two powders were then heated for 24 h in a water bath set to 60 °C. The IL powder rapidly melted, and once this was complete, a magnetic stirrer bar was added. The flask was stoppered, but the side arm was left open. After the 24 h reaction period, the flask was removed from the water bath and allowed to cool. Once fully solidified, the contents of

the flask were transferred to a mortar and ground to a powder. Some small particles of gold could be seen in the otherwise black powder. Samples were taken for crystallisation and for XPS analysis.

A.3 XPS of the Gold Saturated ILs

The samples were pumped down overnight in the chamber's load lock (base pressure 5×10^{-7} mbar) before being transferred to the UHV chamber's sample preparation and analysis chambers (base pressure better than 1×10^{-10} mbar), and subjected to X-ray photoelectron spectroscopy (XPS). To prevent corrosion, molybdenum sample holders were used for all samples. All spectra were recorded with the analyser normal to the sample.

The spectra of **IL-2** were collected at 45 °C, and the spectra of **IL-4** were collected at 70 °C. It was necessary to melt these samples to avoid charging. A type K thermocouple was used to monitor the temperature of the heated samples, and the thermocouple controller also regulated the voltage of the heating filament. During measurements, the temperature was maintained to within ± 0.1 °C. The $[\text{C}_6\text{C}_1\text{Im}]^+$ based ILs were liquid at room temperature; so they did not require any heating.

The radiation source was the Al K_α anode of a Specs XR-50 dual anode source, operating at 12 kV and 20 mA emission current. Spectra were recorded with a Scienta R3000 concentric hemispherical analyser in constant pass energy mode, with a pass energy of 200 eV for wide spectra, and 100 eV for detailed spectra. Data collected were analysed with CasaXPS and charge corrected such that the aliphatic carbon peak is at 284.8 eV.

The Au 4f peaks and the Br 3d peaks of the $[\text{C}_4\text{C}_1\text{C}_1\text{Im}]^+$ -based IL were fitted with an 80 % Lorentzian 20 % Gaussian pseudo-Voigt profile. All other peaks were fitted with 30 % Lorentzian 70 % Gaussian pseudo-Voigt profiles. The Br 3d spectra were fitted with two peaks ($3d_{5/2}$ and $3d_{3/2}$), with the area ratio of the two peaks being set at the expected value of a 3d doublet, 3 : 2, and the full width at half maximum (FWHM) set equal to one another. Two sets of these peaks were necessary for **IL-4**. The C 1s spectra were fitted with two peaks (C_{alkyl} and C_{hetero}) for the $[\text{C}_6\text{C}_1\text{Im}]^+$ -containing ILs, and three peaks (C_{alkyl} , C_{hetero} and C_{NCN}) for the $[\text{C}_4\text{C}_1\text{C}_1\text{Im}]^+$ -containing ILs. In both cases, the FWHM of the C_{hetero} peak was set to $1.1 \times$ that of the C_{alkyl} peak.

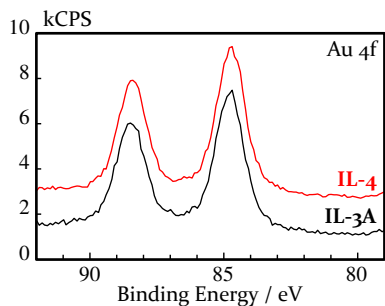


Figure A.1: Au 4f region scan of $[\text{C}_6\text{C}_1\text{Im}][\text{AuBr}_2]$ (batch A) and $[\text{C}_4\text{C}_1\text{C}_1\text{Im}][\text{AuBr}_2]$.

corresponding spectra in chapter 3 (figures 3.5 and 3.6). Comparison of the XPS-derived stoichiometry values given in table A.1 below and table 3.2 in chapter 3 shows that the gold content has doubles, from 0.4 to 0.8 and 0.9 Au atoms per imidazolium cation. As will be discussed below, from the loss of iodine signal intensity and Au 4f binding energy shifts, the use of gold powder has led to a more or less complete conversion of the initial trihalide anions to $[\text{Br}-\text{Au}^{\text{I}}-\text{Br}]^-$ anions by the reaction mechanism proposed in chapter 3.

Apart from the expected XPS lines, some oxygen and hydrocarbon contamination is also present in the $[\text{C}_6\text{C}_1\text{Im}]^+$ based ILs – this can be seen in both the excess of carbon (table A.1) and the enlarged C_{alkyl} peak (relative to the C_{hetero} peak) in figure A.2.

The peak positions for the four ILs studied are given in table A.2. Only minor changes in the cation-related peaks can be seen. It appears that the same amount of charge transfer occurs between the cation and $[\text{Br}_2\text{I}]^-$ and $[\text{AuBr}_2]^-$. Note that the trihalide is already a weakly basic anion⁴¹ – this was discussed in chapter 2.

Notable from the I $3d_{5/2}$ region spectra in figure A.2 in table A.1 is the significant loss of iodine on reaction with the IL. Whilst the depletion of iodine and bromine from the trihalide can be ascribed to halogen off-gassing, the loss of iodine on reaction with the gold indicates that iodine is preferentially reduced. This is not unexpected, because in general bromine will displace iodide.¹⁶ The lack of significant shift in the iodine $3d_{5/2}$ peak position, table A.2, suggests that the remaining iodine is still in the form of $[\text{Br}_2\text{I}]^-$ or a similar species. The bromine shifts (approximately +0.6 eV for both gold saturated ILs, table A.2) suggest that the

The XP spectra collected are presented in figures A.1 and A.2. From the wide spectra, all expected elements are present. Most importantly, the amount of gold in solution after etching of the gold powder by both trihalide ILs is drastically increased as compared to the foil corrosion experiments. This is proven by the higher Au 4f signal intensities in the detailed and survey spectra shown in figures A.1 and A.2 as compared to the

	C 1s	O 1s	N 1s	I 3d _{5/2}	Br 3d	Au 4f	Cu 2p _{3/2}
RSF →	0.208	0.599	0.364	5.740	0.551	3.756	5.77
[C ₆ C ₁ Im][Br ₂ I]	11.7	0.2	≡ 2	0.5	1.7	—	—
<i>nominal</i>	10	0	2	1	2	0	0
[C ₆ C ₁ Im][AuBr ₂]	11.4	—	≡ 2	0.1	1.8	0.8	—
<i>nominal</i>	10	0	2	0	2	1	0
[C ₄ C ₁ C ₁ Im][Br ₂ I]	9.4	0.4	≡ 2	0.5	1.6	—	—
<i>nominal</i>	9	0	2	1	2	0	0
[C ₄ C ₁ C ₁ Im][AuBr ₂]	10.0	0.2	≡ 2	<0.1	1.8	0.9	—
<i>nominal</i>	9	0	2	0	2	1	0
[AuBr ₂] ⁻ /Cu ⁺	10.8	0	≡ 2	0	2.4	0.3	0.6
<i>nominal</i>	10	0	2	0	3	1	1

Table A.1.: Composition of the neat trihalide ILs, the aurous bromide ILs (batch A), and the Au^I/Cu^I mixture.

	Binding Energy / eV							
	C _{hetero}	C _{NCN}	N 1s	I 3d _{5/2}	Br 3d _{5/2}	Au 4f _{7/2}	Cu 2p _{3/2}	
[C ₆ C ₁ Im][Br ₂ I]	IL-1	286.5	—	401.7	620.7	68.2	—	—
[C ₆ C ₁ Im][AuBr ₂]	IL-3A	286.5	—	401.8	620.6	68.8	84.8	—
[C ₄ C ₁ C ₁ Im][Br ₂ I]	IL-2	286.1	287.5	401.5	620.7	68.2	—	—
[C ₄ C ₁ C ₁ Im][AuBr ₂]	IL-4	286.1	287.5	401.5	620.6	68.8, 67.2	84.7	—
[AuBr ₂] ⁻ /Cu ⁺	IL-5	286.5	—	401.7	—	68.7	86.8, 84.8	932.6

Table A.2.: Binding energies of the most prominent lines of the neat trihalide ILs, the aurosbromide ILs, and the Au⁺/Cu⁺ mixture.

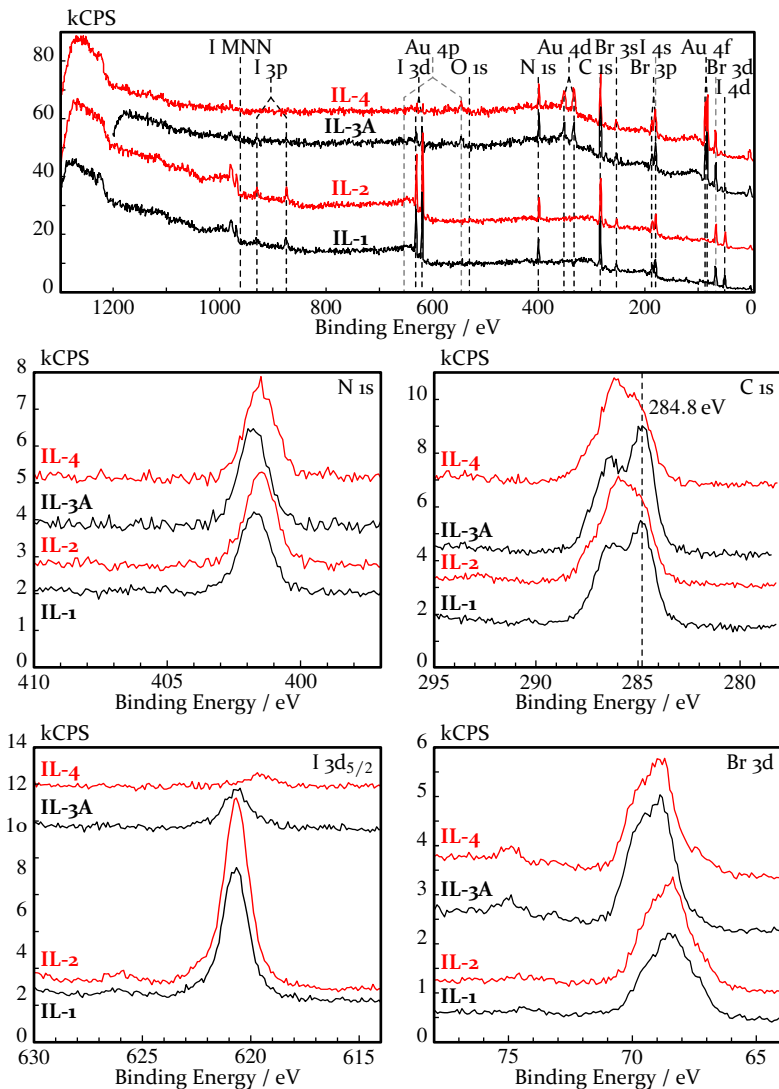


Figure A.2.: XP spectra of the neat trihalide and gold saturated ionic liquids.

degree of electron delocalisation is lessened compared to the trihalide, but still greater than that found in the neat halide (67.2 eV, as per table

2.2 and associated discussion in chapter 2). An interesting observation is that the Br 3d peak of the $[\text{C}_4\text{C}_1\text{Im}][\text{AuBr}_2]$ requires two doublets to fit; this is evidence that the $[\text{AuBr}_2]^-$ complex is not completely symmetric, with one Au – Br bond longer than the others.

The recorded Au 4f peak positions (figure A.1 and table A.2) show no significant difference between the two cations used. This lack of significant position difference is consistent with there being no significant H-bond-mediated charge transfer between the $[\text{AuBr}_2]^-$ species and the $[\text{C}_6\text{C}_1\text{Im}]^+$ cation, cf. the discussion of anion basicity in chapter 2. Further, the peak positions are fully consistent with a Au^1 species.⁶⁹

A.4 Spontaneous Plating

Drops of the saturated gold solution **IL-3B** were placed on copper foils with different treatments, and left in air for 2–3 d under a dust cover (an upturned beaker). The native copper foil was rinsed with acetone before two drops of the gold saturated IL were placed on it and left for 67 h before being rinsed again. For the polished copper foil, strips of copper and zinc were polished with P4000 carbide paper, then rinsed with acetone before the drops of the gold solution were applied. The drops were left on the strips for 63 h 30 min then rinsed with acetone. For the oxidised copper foil, a strip of copper was heated in a propane flame until the surface facing away from the flame had fully oxidised to black. This strip was then quenched in deionised water, rinsed with acetone, and wiped with tissue to remove any soot. Drops of the gold-saturated IL were then placed on the strip and left for 71 h 40 min before being rinsed again in acetone.

After the IL was rinsed off the foils, they were each mounted on separate aluminium stubs for SEM analysis. The EHT voltage used was 15 kV for all samples, and a probe current of 20 pA was used for all sample except the polished copper, where 100 pA was used. Energy-dispersive X-ray spectroscopy (EDX) was also carried out on selected areas of the samples.

The SE micrographs of one of the drops on the native copper foil are presented in figure A.3. At the lowest magnification, three areas are visible: the foil (labelled A), the initial area covered by the IL drop (labelled C), and an area that the drop expanded into over time (labelled B). Further magnification of area C reveals two features in this area. One feature is the large planes made of patches of light-coloured rods and

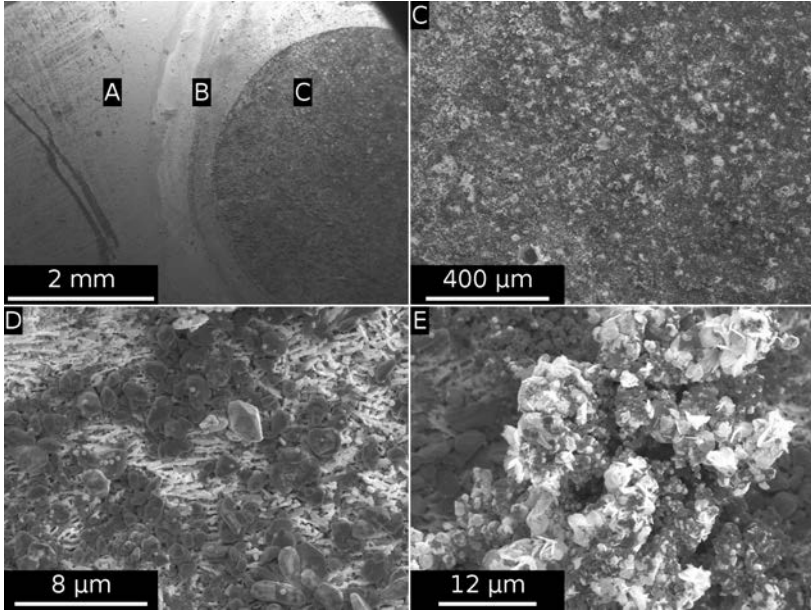


Figure A.3.: SE micrographs of the native copper foil after exposure to the Au-saturated IL for 67 h. Top left: overview with areas A (unexposed foil), C (IL covered area), and B (transition area); panels C–E: magnified views of area C.

darker boulders (labelled D in figure A.3), and vertical dendrite-like features (labelled E in figure A.3). EDX shows that the dark boulders are mostly Au (59.1 %, table A.3), with a smaller amount of copper and halides. It is not clear whether the halide is associated with the copper (as a $\text{Cu}^{\text{II}}/\text{Cu}^{\text{I}}$ salt of some sort), but it does appear that the ‘boulders’ are crystals of metallic gold. The more emissive rods contain less than half the amount of gold and more than twice the amount of copper, and appear to be salt crystals. The dendrites appear to be metallic gold crystals decorated with (possibly copper-based) salt flakes.

The polished copper and zinc (figures A.4 and A.5) by contrast, do not show any significant deposition of gold. No crystals of metallic gold are evident. Note that the amount of gold reported in table A.3 is likely near the lower limit of detection for the EDX system, so whilst any gold seen in EDX could easily be due to some AuBr left on the surface after rinsing, the actual quantification is not likely to be very reliable. It appears that

Foil	Area	Amount / % _{mol}							
		Zn	Cu	Au	Br	I	C	O	
Native Cu	D, boulders	—	12.5	59.1	20.3	8.1	0	0	
	D, rods	—	33.3	26.0	12.6	28.0	0	0	
	E, dendrite	—	13.2	52.2	24.7	10.0	0	0	
Polished Cu	B	—	62.5	7.0	22.6	3.9	0	3.9	
Polished Zn	B	27.5	—	3.2	22.1	1.5	0	45.6	
Oxidised Cu	D crust	—	36.9	7.6	19.2	1.2	0	35.1	
	E boulders	—	9.2	45.7	27.6	1.5	0	15.9	

Table A.3.: Composition (according to EDX) of various areas seen in the SE micrographs.

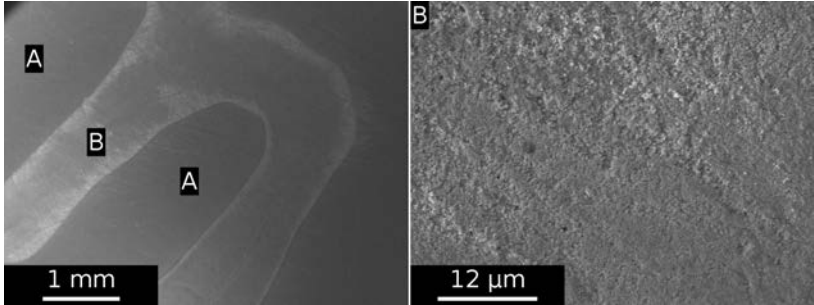


Figure A.4.: SEM of the polished copper foil after exposure to the Au-saturated IL for 63 h 30 min. Left: overview with areas A (unexposed) and B (IL covered area), and right: magnified view of B.

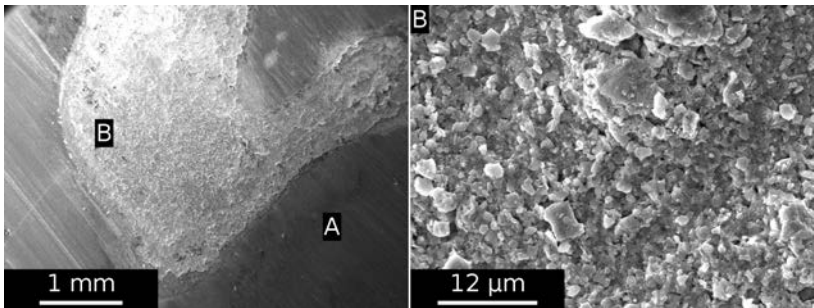


Figure A.5.: SEM of the polished zinc foil after exposure to the Au-saturated IL for 63 h 30 min. Left: overview with areas A (unexposed) and B (IL covered area), and right: magnified view of B.

the spontaneous plating of gold does not occur on polished copper or zinc.

In contrast to the polished copper, and similarly to the native copper, gold deposition is seen on the oxidised copper foil (figure A.6). The (believed to be metallic gold) boulders that were seen in area D of figure A.3 are also seen in area E of figure A.6. EDX of these area shows a significant amount of gold, similar to the boulders found on the native foil. The crust (area D of figure A.6) appears to be composed of a mixture of copper oxides and halides. No dendrite-like formation could be found. The morphological difference between these area and the rods seen

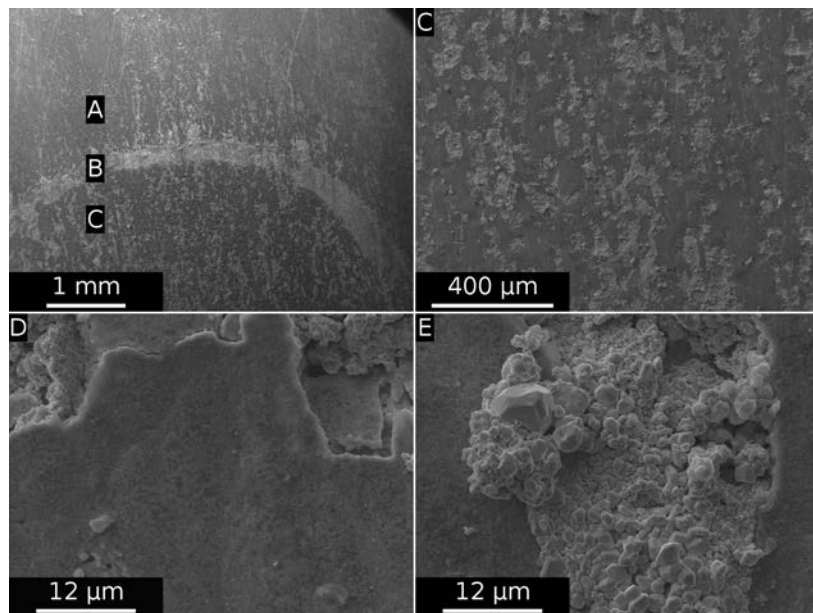


Figure A.6.: SEM of the oxidised copper foil after exposure to the Au-saturated IL for 71 h 40 min. Top left: overview with areas A (unexposed foil), C (IL covered area), and B (transition area); Panels C–E: magnified views of area C.

on the native foil are likely due to the much greater amount of copper oxide present.

It appears that gold will spontaneously deposit onto copper from the gold-saturated IL, but this autodeposition process requires some amount of oxide to be present. This correlates with the visual appearance of the foils. The native and oxidised foils both show patches of dirty looking gold once the IL was rinsed off, whereas the polished foils did not. Additionally, the autodeposition process resulted in patches of gold crystals (and for the native foil dendrite-like formations), rather than a uniform film.

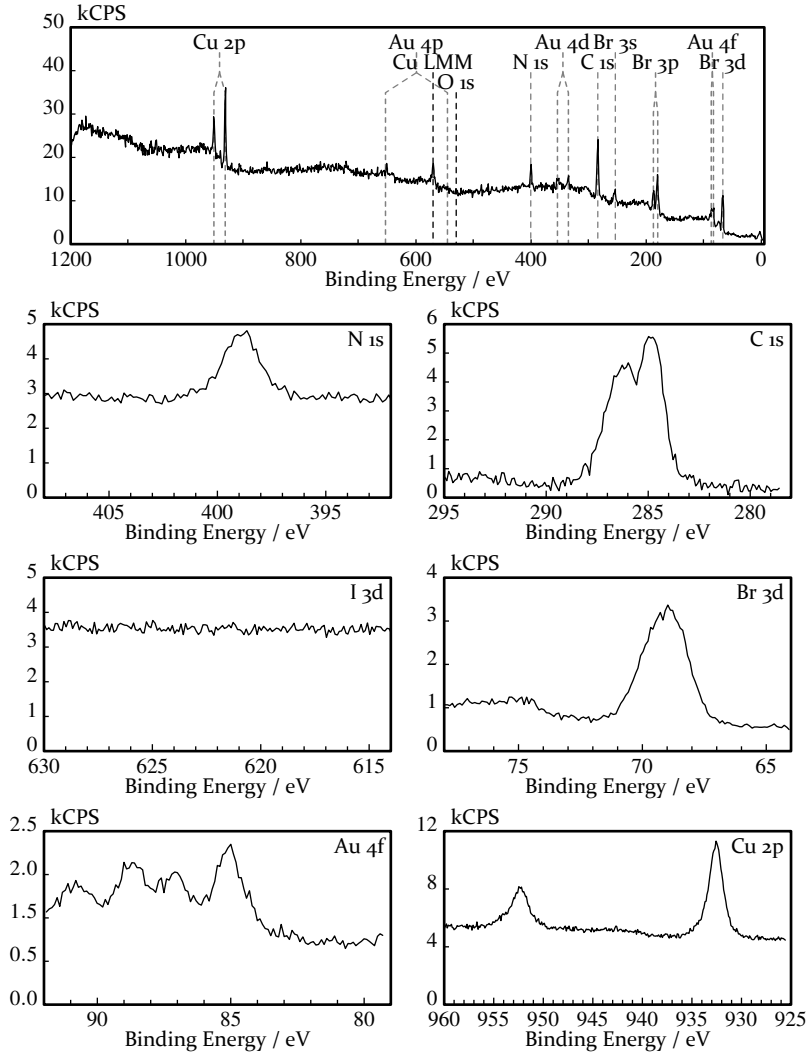


Figure A.7.: XPS spectra of the saturated ionic liquid mixed with an equimolar amount of CuBr.

A.5 Reaction with Copper(I) Bromide

For this test, 986 mg (1.88 mmol) of the gold saturated IL (**IL-3B**) was mixed with 0.27 mg (1.88 mmol) of Copper(I) bromide (CuBr, $\geq 98\%$, Honeywell). This mix (**IL-5**) was held at 40 °C in a water bath for 21 h, during which time it was stirred with a magnetic stirrer bar and occasionally shaken. A sample of the resultant mixture was taken for XPS analysis on a molybdenum sample holder.

As can be seen in figure A.7, both gold and copper can be seen in XPS. The Au 4f region shows two spin-orbit doublets, with the Au 4f_{7/2} peaks at 84.8 and 86.8 eV (table A.2), consistent with an Au^I and an Au^{III} species, respectively.⁶⁹ The Cu 2p_{3/2} peak is seen at 932.6 eV, which is similar to the position recorded for the Cu^I species in chapter 4 (932.3 eV), indicating that a Cu^I species is present. The absence of a large shake-up structure further rules out a Cu^{II} peak⁷²

From the quantification in table A.1, adding CuBr did lead to a loss of gold in solution. Presumably, this gold has formed metallic particles and dropped out of solution, but from the measurements taken this is only speculation.

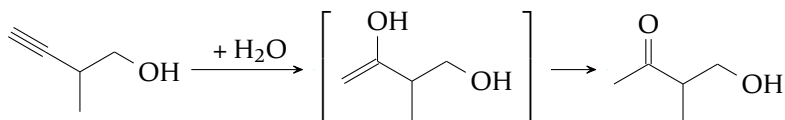
A.6 XRC of the Saturated ILs

Several attempts were made to crystallise **IL-3A** and **IL-4** by Vera Seidl (Lehrstuhl für Anorganische und Allgemeine Chemie, under Prof. Dr. Meyer). However, neither **IL-3A** nor **IL-4** could be crystallised, despite the use of several co-solvents and low temperatures.

A.7 Catalytic Activity

Au^I systems are known for activating carbon-carbon triple bonds⁷⁴ Hence, catalytic activity was tested with the hydration of an alkyne. Catalysis under two conditions was tested by Dr. M. Gantman (Lehrstuhl für Chemische Reaktionstechnik, under Prof. Dr. Wasserscheid): without and with acid present. In both cases 5.00 g of 2-methylbut-3-yn-1-ol, 1.05 g of deionised water (approximately equimolar with the alcohol), and 0.60 g of the gold saturated IL were added to a round bottomed flask. In the first experiment, no acid was added; in the second, 0.50 g of sulfuric acid was added to the water before adding the IL and

the alkyne. The reaction vessel was placed under a slight argon purge, and the mixture was then stirred magnetically at 80 °C for 3 h. A sample of the reaction products were taken for NMR analysis. The expected product of the hydration reaction is shown in scheme 7 – hydration of the alkyne functionality to form an intermediate enol species, followed by tautomerisation to a ketone species.



Scheme 7

At 80 °C the IL dissolved in the reaction mixture. The NMR spectra from both the no-acid and with-acid experiments showed only the original alcohol – no signals corresponding to either the enol nor the ketone could be found. From this, it can be concluded that [Br₂Au]⁻ is not significantly catalytically active with respect to alkyne functionalities. This is unsurprising, since the initial step in gold(I)-mediated alkyne activation is a Lewis acid attack on the triple bond⁷⁴ – an anionic complex is unlikely to exhibit the same degree of carbophilicity or Lewis acidity as a cationic complex, thus inhibiting its ability to form a coordinate bond with the triple bond and catalyse the reaction.

A.8 Cyclic voltammetry

Three ionic liquids were subjected to a cyclic voltammetry test experiment: the neat halide [C₆C₁Im]Br, the trihalide **IL-1**, and the gold-saturated **IL-3B**. Cyclic voltammetry was carried out with a Keithley 2450 SourceMeter, operating at 100 mV·s⁻¹ (lower scan speeds were tried, but did not yield additional information). The reference and counter electrodes were platinum (0.3 and 0.5 mm \varnothing), and the working electrode was either platinum (0.5 mm \varnothing) or copper (0.25 mm \varnothing). All of the platinum electrodes were cleaned by annealing then rinsing with ultra pure water, and for each IL fresh copper wires were used (which were cleaned with P4000 grit carbide paper and rinsed with isopropanol).

A Preliminary investigations of High-Gold Content Ionic Liquids

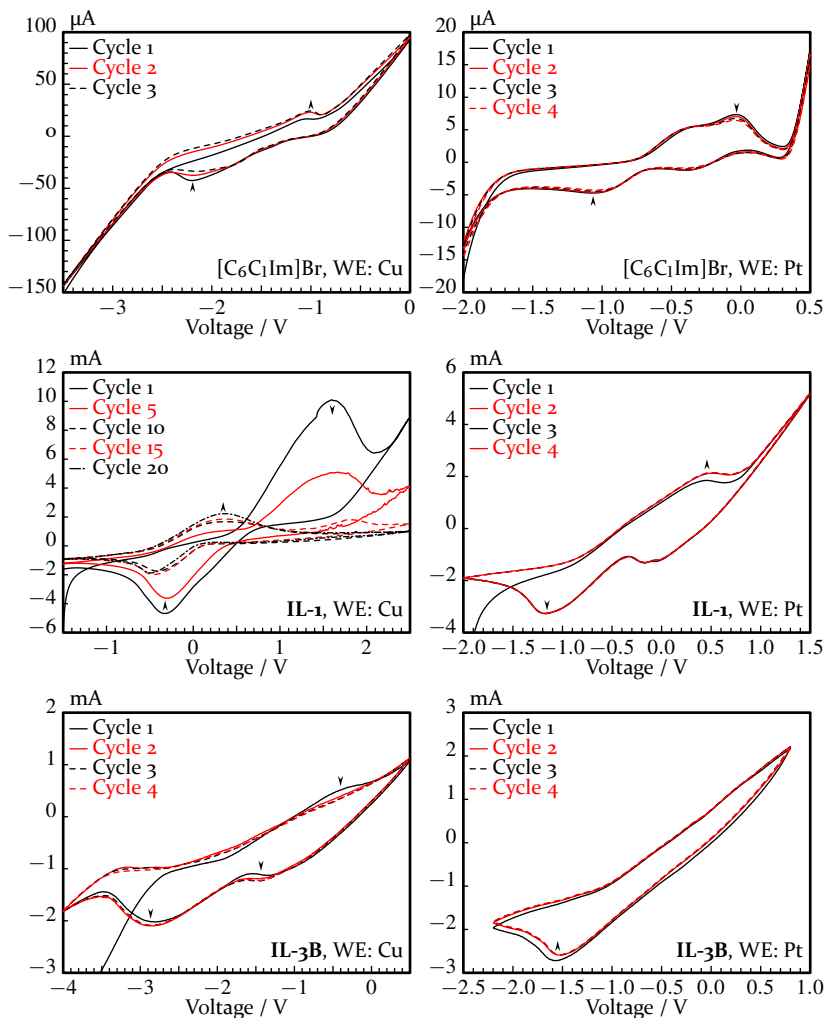


Figure A.8: Cyclic Voltammograms of $[C_6C_1Im]Br$, **IL-1**, and **IL-3B**; with copper (left) and platinum (right) working electrodes.

A.9 Differential Scanning Calorimetry and Thermogravimetric Analysis

Differential scanning calorimetry (DSC) was attempted by Dr. M. Gantman (Lehrstuhl für Chemische Reaktionstechnik, under Prof. Dr. Wasserscheid) with aluminium crucibles – unfortunately these proved susceptible to corrosion by the trihalide IL, and so DSC could not be performed.

Thermogravimetric analysis (TGA) of **IL-1** and **IL-3B** was also carried out by Dr. Gantman with a Setaram TG-Analyser in corrosion resistant quartz crucibles, heated from 30 to 600 °C at a set rate of 10 K·min⁻¹, under a nitrogen flow rate of 50 ml·min⁻¹. The spectra recorded are presented in figure A.9.

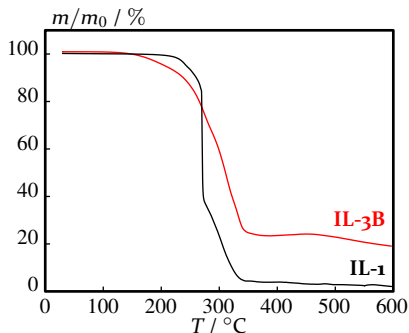


Figure A.9.: Relative mass changes of the neat trihalide IL and the gold-rich IL (batch B).

A.10 Infrared Spectroscopy

Infrared spectra of **IL-1** and **IL-3B** were collected by Dr. M. Gantman (Lehrstuhl für Chemische Reaktionstechnik, under Prof. Dr. Wasserscheid) on a Jasco FT/IR 6400 Spectrometer operating in ATR mode, with air used as the reference, with a scanning speed of 2 mm·s⁻¹. The scan range was 400–3700 cm⁻¹; however, in figure A.10 the spectra has been cut off below 1000 cm⁻¹, because at these wavenumbers the transmittance recorded is subject to some form of noise resulting in transmittances over 100%. Further, the recorded spectra have a low signal-to-noise ratio, the cause of which is not presently known.

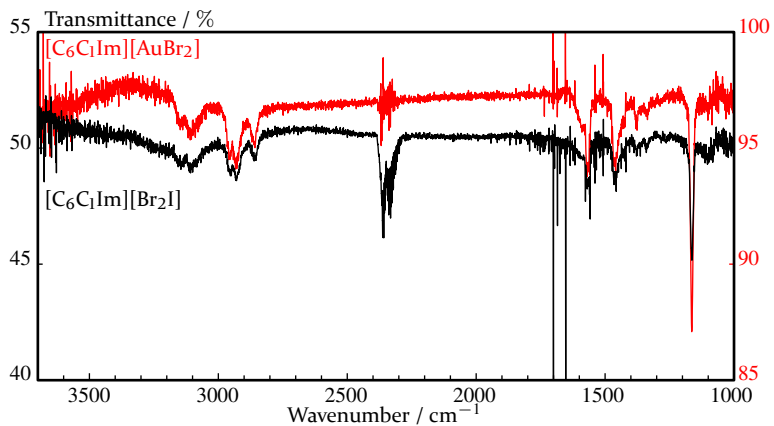


Figure A.10.: Transmittion FT/IR of the neat trihalide IL and the gold-rich IL (batch B).

B New Sample Holders For The ESCA Chamber

In the course of this work, two new sample holders, designed for ionic liquid work, were developed. The first holder was designed to bolt onto the existing sample holders, and featured a well into which ionic liquid could be spread. The second design integrated this well into the sample holder base plate.

B.1 The Bolt-On Well Plate

The standard sample holder has four threaded holes, allowing attachments to be bolted into place with four M2 bolts. There is already a deep reservoir for ionic liquids, but the walls of that reservoir are some 3 mm deep, making angle resolved measurements impractical, either due to the large amount of liquid needed to fill the reservoir or due to the walls shadowing the sample.

To solve this issue, a bolt-on well plate with a reservoir depth of 0.5 mm was designed – see figures B.1 and B.2. This well plate can be bolted onto the same sample holders as the deep reservoir, and require far less ionic liquid than the deep reservoir. If needed, thermocouple wires can be secured to the plate by one of the four retaining bolts.

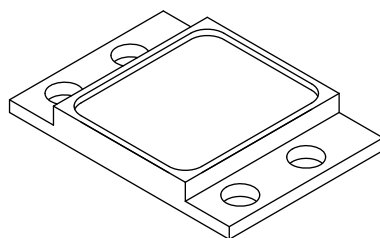


Figure B.1.: Isometric drawing of the well plate, 2 : 1 scale.

Earlier designs of this well plate featured a narrower well (9 × 13 mm) and a smaller radius for the corners (1 mm). Both were deemed to be a disadvantage. The narrower well led to the plate being visible in some

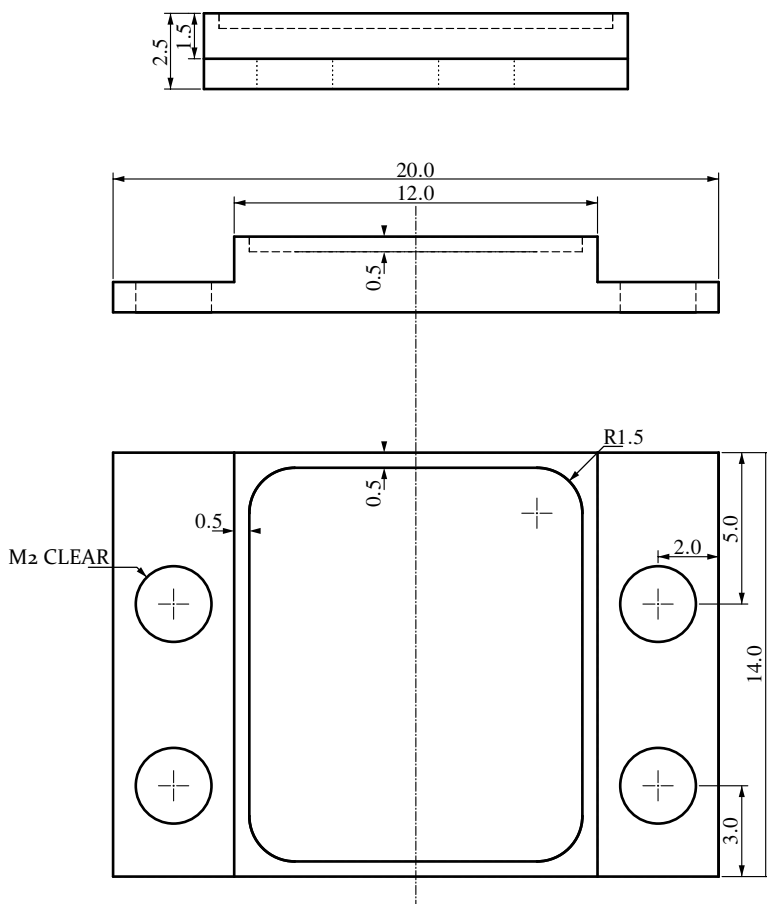


Figure B.2.: Schematic of the well plate, 4 : 1 scale. All dimensions are in mm. From the REV D schematics, sheet 1/1, dated 2017-03-09.

scans, and the smaller corner radius made polishing the sample holder more difficult. Aside from breaking the edges and polishing the inside of the well, the surface finish was as machined. Before use, the inside of the well plate was polished by a glass and ceramic cleaning paste.

Prototyping involved an initial design machined from aluminium (REV B), followed by a stainless steel prototype (REV C), and finally

several REV D well plated milled from A2 (nickel-chrome type) stainless steel. 1.4301 (DIN EN X5CrNi18-10) Stainless steel is specified in the drawings, but there is no reason why other materials cannot be substituted.

B.2 The Well Holder

Experience with the bolt-on well plate shows that for 80° measurements, a wider well is desirable. A design for a wider bolt-on plate was considered, however such a design would necessarily have a blind hole for the bolts. This is undesirable, since it requires special vacuum bolts of the right length. A ready supply of spares entails buying many of these specialised components and potentially cutting them to length. Rather than attempting to design around this, a new sample holder base with a milled-in well was designed, figures B.3 and B.4.

Aside from a $14 \times 20 \times 0.5$ mm well milled into the base of the plate, the design is the same as the existing sample holders. The same ceramic and pins assembly is mounted on the back of the sample holder as on the regular sample holders. A thermocouple can be spot welded onto the raised edge of the holder if needed.

The initial design of the well holder (REV A) contained an error. The notches, into which the barbs of the wobble stick lock when the sample is being transferred, were put onto the same side of the plate, when they should be on opposite sides. This was corrected in REV B. Two REV B sample holders were milled from molybdenum, to match the other sample holders already in use. It was found that the slot into which the wobble stick slides was slightly too tight on one of the holders – the fit can be loosened with a fine grinding bit.

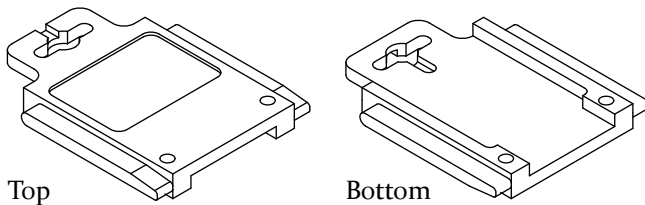


Figure B.3.: Isometric drawing of the well plate, 1 : 1 scale.

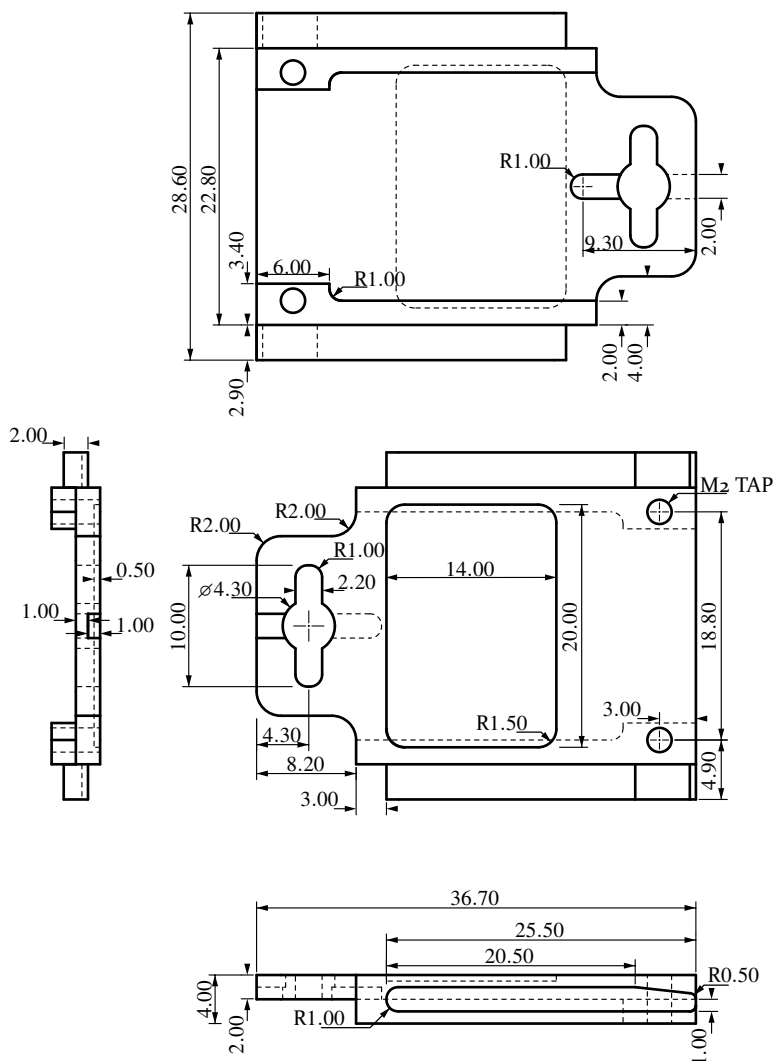


Figure B.4.: Schematic of the well plate, 4 : 1 scale. All dimensions are in mm. From the REV B schematics, sheet 1/2, dated 2017-05-22.

C Appendix: Electroplating Stainless Steel and Molybdenum

Electroplating is not an exact process, but the procedure and setup described here should give acceptable results most of the time. Stainless steel and molybdenum must be carefully prepared for gold plating – gold will not plate directly onto these metals, and the formation of a passivating oxide layer initially prevents other metals plating. Electroplating stainless steel and molybdenum consists of four steps: degreasing, masking, plating and polishing.

Before plating the surface should have the desired final finish. The plating process will not fill in scratches and machining marks. Heavy oxide layers should be removed with fine sand paper. If a smooth flat final surface is needed then it should be obtained before plating. Any grinding/smoothing operations should be completed before plating. Also, any tantalum should be removed from the piece – tantalum will poison the gold plating solution and isn't covered by the other plating metals.

C.1 Degreasing

Grease or other organic contaminants must be removed. In some cases a wipe and rinse with solvent is sufficient. Some pieces will need to be scrubbed with soap or Scheuermilch, or polished with glass/ceramic cleaner then rinsed in solvent. Finally, the part should be cleaned with isopropanol or acetone in an ultrasonic bath for 30 min. Once out of the bath, the piece should receive one final rinse in solvent, and be left to oven or air dry.

Throughout this process, it is important to prevent recontamination with oily residues. Clean gloves are a must. Brown or otherwise discoloured patches that appear after the nickel plating indicate a contaminating organic residue.

C.2 Masking

Once the piece is thoroughly dry, the area that shouldn't be plated can be covered. Parts with a large surface area may benefit from masking off some areas. Nail polish (acetone base, any colour) can be used for this. The masked sections should receive a coating thick enough to be entirely opaque. The mask must be allowed to fully cure before the next step, otherwise it may peel or blister.

C.3 Plating

The first plating solution is a nickel strike, followed by a copper solution, and finally the gold solution. The first two solutions can be made in the lab, the last one can be purchased from Conrad (EAN 4 016138 032512). For the nickel strike and the copper solution, use a standard lab power supply set to 6 V. For the gold plating, set the power supply to 4 V. Plating should be carried out in a fume hood. For each of the plating steps, a clean counter electrode made of the plating metal should be used. The piece should be thoroughly rinsed with deionised water after each plating step.

C.3.1 Wood's Nickel Strike

There are several nickel strike formulations, Wood's is one of the simpler ones. Wood's strike is made of nickel(II) chloride ($250 \text{ g}\cdot\text{l}^{-1}$ as $\text{NiCl}_2 \cdot (\text{H}_2\text{O})_6$, $136 \text{ g}\cdot\text{l}^{-1}$ as anhydrous) and concentrated hydrochloric acid (37 %, $250 \text{ ml}\cdot\text{l}^{-1}$) in deionised water. It may be necessary to reduce the pH of the solution if it rises above approximately pH 1.

The strike is applied to the part cathodically for 5 min. The finished plating should look somewhere between matte off-white and matte steel grey. During plating, the current should be *ca.* 1 A, and the part will effervesce hydrogen. It may be necessary to put a protective resistor in series with the part to prevent pitting, especially with smaller parts. 4Ω and 20 W is recommended.

C.3.2 Copper Plating Solution

The copper plating solution is copper acetate. This can be made by mixing acetic acid ($1 \text{ mol}\cdot\text{l}^{-1}$), hydrogen peroxide (*ca.* 20%), and deionised water in a 2 : 1 : 2 v : v : v ratio. Then stir and warm the mix to $\sim 75^\circ\text{C}$ and drop in some copper chunks – used UHV gaskets (sanded to remove obvious discolouration) are a suitable option. The exact amounts and concentrations are not important. After about an hour the solution should have gone a light blue colour. At this point, stop the heating and let the solution stand until the effervescence stops, then remove the copper chunks. Filter then dilute the solution up to the desired volume for plating with deionising water. This solution must be replaced after a few uses, when it starts to take on a green hue.

The copper should be applied cathodically for 20 min. During plating the current should be about 50 mA. No protective resistor should be necessary. The final plating should be a matte salmon pink.

C.3.3 Gold Plating Solution

The Conrad solution is based on ammonium tetrachloroaurate ($[\text{NH}_4][\text{AuCl}_4]$), and after a few uses will need to be filtered. As long as the filtrate is a bright yellow, the solution should be OK to reuse. This plating step is the most susceptible to failure. One common mistake is allowing the plating solution to contact the crocodile clip – this causes chromium to co-plate with the gold – this also contaminates the plating solution, which will have to be disposed of.

The gold should be applied cathodically for 30 min. Larger pieces may need a longer plating time. It may be necessary to change the position of the piece during plating to ensure an even coating.

C.4 Polishing

Polishing should be done with a very fine abrasive – glass/ceramic cleaner paste is a good option. A dremel tool with a buffing wheel bit is a good way to do the polishing.

C.5 Results

If everything has gone well then a stable, long lasting gold plating should be formed. The plated part can be cleaned in an ultrasonic bath

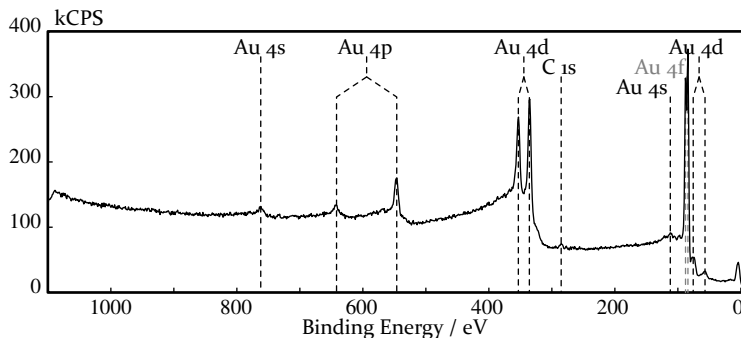


Figure C.1: XP spectra of a gold plated sample holder, after sputtering to remove carbon contamination.

as normal. The gold used should be sufficiently pure for sample holder use. Figure C.1 is the XPS spectrum of a gold plated sample holder

Unfortunately, achieving a uniform and thick coating is a matter of luck more than anything else. Several of the plated pieces have had the plating come off after several months of use. Additionally, it appears that some batches of the Conrad gold plating solution are contaminated with silver.

It appears that whilst gold plating stainless steel and molybdenum is possible, the plating solution sold by Conrad is not the most reliably pure, and the longevity of the platings have proved to be too variable to be considered reliable. Plating thickness may be to blame, but without further investigation it is not possible to say definitively.

D Spectra Plotting and Analysis Programs

In the course of this work, several Python 3 programs were written to plot data exported from CasaXPS. Two libraries were used extensively – NumPy⁸⁴ and matplotlib⁸⁵.

D.1 Basic CasaXPS Export XPS Data Plotting

The following program is a basic program for plotting data exported from CasaXPS. The plotting program ingests tab-delimited .TXT files, exported as Rows of Tables.

```
1 from glob import glob
2 from numpy import genfromtxt
3 from matplotlib.pyplot import plot, savefig, figure,
   title, xlabel, ylabel,\
4     xlim
5
6 ## Get the peak from the user
7 while True:
8     peak = input("Enter peak: ")
9     peak = peak.replace(' ', '')
10
11     ## Try to find files
12     files = glob("*_{}.TXT".format(peak))
13     if len(files) == 0:
14         print("No files with matching peak found.")
15     else:
16         print("")
17         break
18
19 ## Start plotting stuff
```

D Spectra Plotting and Analysis Programs

```
20 for file in files:
21     fig = figure(figsize=(11,7))
22
23     ## Load data from file
24     data = genfromtxt(file, unpack=True, names=True,
25                       delimiter='\t')
26
27     names = data.dtype.names[:-2]
28
29     ## Plot the data
30     try:
31         ## Plot Envelope
32         plot(data["BE"], data["Envelope"], 'b-',
33              linewidth=2, alpha=0.5,\
34              clip_on=False, solid_capstyle='round',
35              solid_joinstyle='round')
36         ## Plot CPS
37         plot(data["BE"], data[names[1]], 'k-', linewidth
38              =0.5,\
39              clip_on=False, solid_capstyle='round',
40              solid_joinstyle='round')
41         ## Plot Components
42         for name in names[2:-2]:
43             plot(data["BE"], data[name], 'r-', linewidth
44                  =0.5,\
45                  clip_on=False, solid_capstyle='round',
46                  solid_joinstyle='round')
47         ## Plot Background
48         plot(data["BE"], data["Background"], 'b-',
49              linewidth=0.5,\
50              clip_on=False, solid_capstyle='round',
51              solid_joinstyle='round')
52     except:
53         print("Data file {} has no Components.".format(
54               files_A[n]))
55         ## Plot CSP
56         plot(data["BE"], data[names[1]], 'k-', linewidth
57              =0.5,\
58              clip_on=False, solid_capstyle='round',
59              solid_joinstyle='round')
60         ## Plot Background
61         try:
62             plot(data["BE"], data["Background"], 'b-',
63                  linewidth=0.5,\
```

```

50             clip_on=False, solid_capstyle='round',
                solid_joinstyle='round')
51     except:
52         print("Data file {} has no background.".
                format(files_A[n]))
53
54     ## Set axis labels etc.
55     file_out = file[:-4]
56     title(file_out.replace('_', ' '))
57     xlabel("BE / eV")
58     ylabel("I / CPS")
59
60     ## Set BE scale
61     xlim(max(data["BE"]), min(data["BE"]))
62
63     ## Save the graphs
64     savefig(file_out+".svg")
65     savefig(file_out+".pdf")
66     print("File {} saved.\n".format(file_out+".svg"))

```

D.2 Plotting and Scaling Dual-Analyser XPS Data

This plotting script ingests two CasaXPS exports, scales one of them, and plots the two together. The program assumes that the file names are of the format $\langle variable \rangle_A_ \langle peak \rangle .TXT$, where $\langle variable \rangle$ is a marker denoting spectra in a series, for example -75C, -60C etc., and $\langle peak \rangle$ is the XPS peak, for example N1s. There should be no spaces in the file names.

```

1 from glob import glob
2 from numpy import genfromtxt, loadtxt
3 from matplotlib.pyplot import plot, savefig, figure,
    title, xlabel, ylabel, \
4     xlim
5
6 ###--- Function Definitions ---###
7
8 ## Function that does the plotting
9 def spectra_plot(data, alt_colour=False, scale=1):
10     ## Get data field names
11     names = data.dtype.names[:-2]

```

D Spectra Plotting and Analysis Programs

```
12
13     ##Set colours etc.
14     if alt_colour == False:
15         lines = {"env": 'b-', "CPS": 'k-', "comp": 'r-',
16                 "BG": 'b-'}
17     else:
18         lines = {"env": 'g-', "CPS": 'r-', "comp": 'k-',
19                 "BG": 'g-'}
20
21     try:
22         ## Plot Envelope
23         plot(data["BE"], data["Envelope"]*scale, lines["
24             env"], linewidth=2,\
25             alpha=0.5, clip_on=False, solid_capstyle='
26             round',\
27             solid_joinstyle='round')
28         ## Plot CPS
29         plot(data["BE"], data[names[1]]*scale, lines["
30             CPS"], linewidth=0.5,\
31             clip_on=False, solid_capstyle='round',
32             solid_joinstyle='round')
33         ## Plot Components
34         for name in names[2:-2]:
35             plot(data["BE"], data[name]*scale, lines["
36                 comp"], linewidth=0.5,\
37                 clip_on=False, solid_capstyle='round',
38                 solid_joinstyle='round')
39         ## Plot Background
40         plot(data["BE"], data["Background"]*scale, lines
41             ["BG"], linewidth=0.5,\
42             clip_on=False, solid_capstyle='round',
43             solid_joinstyle='round')
44     except:
45         print("Data file {} has no Components.".format(
46             files_A[n]))
47         ## Plot CSP
48         plot(data["BE"], data[names[1]]*scale, lines["
49             CPS"], linewidth=0.5,\
50             clip_on=False, solid_capstyle='round',
51             solid_joinstyle='round')
52         ## Plot Background
53         try:
```


D.2 Plotting and Scaling Dual-Analyser XPS Data

```
41         plot(data["BE"], data["Background"]*scale,
42              lines["BG"],\
43              linewidth=0.5, clip_on=False,
44              solid_capstyle='round',\
45              solid_joinstyle='round')
46     except:
47         print("Data file {} has no background.".
48               format(files_A[n]))
49
50 ###--- Main Program ---###
51
52 ## Get the peak from the user
53 while True:
54     peak = input("Enter peak: ")
55     peak = peak.replace(' ', '')
56
57     ## Get a list of file names
58     files_A = glob("*_A_{}.TXT".format(peak))
59     files_B = glob("*_B_{}.TXT".format(peak))
60
61     ## Transform the list into a dictionary
62     labels_A = [label.replace("_A_{}.TXT".format(peak),
63                               '') for label in\
64                 files_A]
65     files_A = {label: fname for label, fname in zip(
66                 labels_A, files_A)}
67     labels_B = [label.replace("_B_{}.TXT".format(peak),
68                               '') for label in\
69                 files_B]
70     files_B = {label: fname for label, fname in zip(
71                 labels_B, files_B)}
72
73     ## Test is any files were returned
74     if (len(files_A) and len(files_B)) > 0:
75         break
76     else:
77         print("No files with a matching peak.")
78
79 ## Ask whether to use both sets or just one
80 while True:
81     both_in = input("Do you want to plot both sets? y/n:
82                    ")
83     if both_in.lower().strip() == 'y':
```

D Spectra Plotting and Analysis Programs

```
76     ## Ask for scaling factor
77     while True:
78         B_fac = input("Enter scaling factor or file
79                     for B data: ")
80         try:
81             B_fac = {label: float(B_fac) for label
82                     in labels_A}
83             try_B = True
84             break
85         except:
86             try:
87                 labels = genfromtxt("B_fac.dat",
88                                     delimiter='\t', usecols=0,\
89                                     dtype=str)
90                 B_fac_raw = genfromtxt("B_fac.dat",
91                                       delimiter='\t',\
92                                       usecols=1)
93                 B_fac = {label.strip(): row for
94                         label, row in zip(labels,\
95                                           B_fac_raw)}
96                 try_B = True
97                 B_fac_file = True
98                 break
99             except:
100                print("Could not understand input.")
101
102     break
103
104 elif both_in.lower().strip() == 'n':
105     try_B = False
106
107     ## Ask whether to plot the A or B files
108     while True:
109         A_or_B_in = input("Plot set A or B? ")
110         if A_or_B_in.lower().strip() == 'a':
111             break
112         elif A_or_B_in.lower().strip() == 'b':
113             files_A = files_B
114             break
115         else:
116             print("Could not understand input.")
117
118
```

```

114         break
115
116     else:
117         print("Could not understand answer. Please enter
118             y or n.")
119
120 print("")
121
122 ## Start plotting stuff
123 for label in labels_A:
124     fig = figure(figsize=(11,7))
125
126     ## Load and plot B data
127     if try_B == True:
128         data_B = genfromtxt(files_B[label], unpack=True,
129                             names=True,\
130                             delimiter='\t')
131         spectra_plot(data_B, alt_colour=True, scale=
132                       B_fac[label])
133
134     ## Load and plot A data
135     data_A = genfromtxt(files_A[label], unpack=True,
136                         names=True, delimiter='\t')
137     spectra_plot(data_A)
138
139     ## Set axis labels etc.
140     if try_B == True:
141         file_out = files_A[label][:-4].replace("_A", '')
142                 .replace("_B", '')
143         title("{}, B factor {:.3f}".format(file_out.
144                                             replace('_', ' '),\
145                                             B_fac[label])
146              )
147     else:
148         file_out = files_A[label][:-4]
149         title(file_out.replace('_', ' '))
150
151     xlabel("BE / eV")
152     ylabel("I / CPS")
153
154     ## Set the BE scale
155     if try_B == True:

```

```
149         max_BE = max([max(data_A["BE"]), max(data_B["BE"  
                ])])  
150         min_BE = min([min(data_A["BE"]), min(data_B["BE"  
                ])])  
151     else:  
152         max_BE = max(data_A["BE"])  
153         min_BE = min(data_A["BE"])  
154     xlim(max_BE, min_BE)  
155  
156     ## Save the graphs  
157     savefig(file_out+".svg")  
158     savefig(file_out+".pdf")  
159     print("File {} saved.\n".format(file_out+".svg"))
```

D.3 Plotting Hidden Mass Spectra

The control software for the Hidden QMS attached to the Mass Spectrometry Chamber defaults to outputting propriety .exp files, but can export to the .csv format that this plotting program needs. When exporting, one can choose which spectra in a series to export – this program can plot multiple spectra in a single .csv file. Because this plotting program tends to produce a large number of output files, it stores the output file in a folder named after the name of the input file.

```
1 from os.path import isdir  
2 from os import mkdir  
3 from numpy import array, genfromtxt  
4 from matplotlib.pyplot import plot, savefig, xlabel,  
    xlim, ylim, ylabel, title,\br/>5     figure, show  
6  
7 ## Get file name  
8 while True:  
9     MS_file_name = input("Enter the file name: ")  
10    if MS_file_name[-4:].lower() == ".csv":  
11        MS_file_name = MS_file_name[:-4]  
12    else:  
13        MS_file_name = MS_file_name  
14  
15    try:  
16        file = open(MS_file_name+".csv")  
17        file.close()
```

```

18         break
19     except:
20         print("File not found.")
21
22     ## Check for and make the folder for the plotted graphs
23     if not isdir(MS_file_name):
24         mkdir(MS_file_name)
25
26     #MS_file_name = "2017-02-16_FAR_1-1e-6mbar.csv"
27     file_base = MS_file_name+"_{}"
28
29     with open(MS_file_name+".csv") as MS_file:
30         while True:
31             line = MS_file.readline()
32
33             ## Detects the start of a data block
34             if line == '"Scan","Cycle","Time","ms",\n':
35                 line = MS_file.readline().replace(',\n', ' ')
36                 scan, cycle, time, time_ms = line.split(',')
37
38                 ## Reset data arrays
39                 mass = []
40                 pressure = []
41
42                 ## Start reading the data
43                 while True:
44                     line = MS_file.readline()
45
46                     ## Skip units header
47                     if line == '"amu","torr"\n':
48                         MS_file.readline()
49
50                     ## process the numbers
51                     else:
52                         mz, torr = line.strip().split(',')
53                         try:
54                             mass.append(float(mz))
55                             pressure.append(float(torr))
56                         except:
57                             mass = [mz]
58                             pressure = [torr]
59

```

D Spectra Plotting and Analysis Programs

```
60         ## Stops reading in the numbers if
           the final mass is reached
61     if float(mz) == stop:
62         ## Convert to mbar from torr
63         pressure = array(pressure)
           *1.33322
64
65         figure(figsize=(11,7))
66
67         ## Plot the data
68         plot(mass, pressure, 'r-',
           linewidth=0.5,\
69             clip_on=False,
           solid_capstyle='round'
           ,\
70             solid_joinstyle='round')
71
72         ## Sets the plotting region,
           modify is needed
73         xlim(0, mass[-1])
74         ##ylim(
75
76         xlabel("m/z / amu")
77         ylabel("p / mbar")
78         title(file_base.replace('_', ' '
           ).format(cycle))
79
80         ## Save the figure
81         savefig(MS_file_name+"/"+
           file_base.format(cycle+".svg
           "))
82         savefig(MS_file_name+"/"+
           file_base.format(cycle+".pdf
           "))
83         print("Saved cycle {}".format(
           cycle))
84         break
85
86     elif line == '':
87         break
88
89     ## Read data relating to the scan
```

```

90     elif line == "Scan ID","Mode","Input","Scanned
          ,"Start","Stop","Increment","Dwell","Settle
          ","RS","RelSEM"\n':
91         line = MS_file.readline().replace('\n', '')
92         SID, mode, input_det, scanned, start, stop,
          increment, dwell,\
93             settle, RS, relSEM = line.split(',')
94
95         ## Convert the stop value to a float for
          later comparision
96         stop = float(stop)

```

D.4 Plotting Keithley Cyclic Voltammograms

The Keithley 2450 SourceMeter saves each scan as a .csv file, with one file containing all of the scan cycles programmed. The program below plots the voltammograms in two ways – as a single line for all cycles, and with each cycle as a separate line.

```

1  from os.path import isdir
2  from os import mkdir
3  from numpy import array, genfromtxt
4  from matplotlib.pyplot import plot, savefig, xlabel,
          xlim, ylim, ylabel, title,\
5          figure, show, close
6
7  for CV_file_name in CV_files:
8      ## Get file name
9      while True:
10         CV_file_name = input("Enter the file name: ")
11         if CV_file_name[-4:].lower() == ".csv":
12             CV_file_name = CV_file_name[:-4]
13         elif CV_file_name == "exit":
14             break
15
16         try:
17             file = open(CV_file_name+".csv")
18             file.close()
19             break
20         except:
21             print("File not found.")
22

```

D Spectra Plotting and Analysis Programs

```
23     ## Check for and make the folder for the plotted
      graphs
24     if not isdir(CV_file_name):
25         mkdir(CV_file_name)
26
27     file_base = CV_file_name+"_{}"
28
29     ## Read through headers
30     with open(CV_file_name+".csv") as CV_file:
31         while True:
32             line = CV_file.readline()
33
34             ## Read the General parametres block
35             if line == "General Parameters:\n":
36                 line = CV_file.readline().replace("EOC
      potential, ", ').strip()
37                 EOC_text, EOC_unit = line.split(', ')
38                 EOC = float(EOC_text)
39                 EOC_text = "{:.3f} {s}".format(EOC,
      EOC_unit)
40                 line = CV_file.readline().replace("
      fileName, ", ').strip()
41                 file_name = line
42
43             ## Read the Source parameters
44             elif line == "Source Parameters:\n":
45                 line = CV_file.readline().replace("
      Source Range, ", ').strip()
46                 source_range = int(line)
47                 line = CV_file.readline().replace("# of
      Vertices, ", ').strip('\n')
48                 vertex_count1, vertex_count2 = line.
      split(', ')
49                 line = CV_file.readline().replace("
      Vertex 1, ", ').strip()
50                 vertex1, vertex_unit1 = line.split(', ')
51                 line = CV_file.readline().replace("
      Vertex 2, ", ').strip()
52                 vertex2, vertex_unit2 = line.split(', ')
53                 line = CV_file.readline().replace("
      Vertex 3, ", ').strip()
54                 vertex3, vertex_unit3 = line.split(', ')
```


D.4 Plotting Keithley Cyclic Voltammograms

```
55     line = CV_file.readline().replace("
        Source Rate, ", '').strip()
56     rate, rate_unit = line.split(' ', ')
57     line = CV_file.readline().replace("# of
        Cycles, ", '').strip()
58     cycles = int(line)
59
60     ## Read the calculator parameters
61     elif line == "Calculated Parameters\n":
62         line = CV_file.readline().replace("
            stepSize, ", '').strip()
63         step_size, step_size_unit = line.split('
            , ')
64         line = CV_file.readline().replace("
            sourceDelay, ", '').strip()
65         delay, delay_unit = line.split(' ', ')
66
67     ## Read CV data
68     elif line == "Voltage,Current,Seconds\n":
69         while True:
70             line = CV_file.readline().strip()
71             if line == '':
72                 break
73
74             U, I, t = line.split(',')
75             try:
76                 voltage.append(float(U))
77                 current.append(float(I)*1e3)
78                 time.append(float(t))
79             except:
80                 voltage = [float(U)]
81                 current = [float(I)*1e3]
82                 time = [float(t)]
83
84         figure(figsize=(11,7))
85         ###current = array(current)
86
87         ## Plot the data
88         plot(voltage, current, 'r-', linewidth
            =0.5, clip_on=False,\
89             solid_capstyle='round',
            solid_joinstyle='round')
```

D Spectra Plotting and Analysis Programs

```
91         ##xlim(0, mass[-1])
92         ##ylim(
93
94         xlabel("U / V")
95         ylabel("I / mA")
96         title("{:}, {:} {:}".format(file_name,
97                                     rate, rate_unit))
98
99         ## Save the figure in it's own folder
100        savefig(CV_file_name+"/"+file_name+".svg
101                ")
102        savefig(CV_file_name+"/"+file_name+".pdf
103                ")
104        savefig(file_name+".png")
105        print("Saved CV {}".format(file_name))
106
107        break
108
109    figure(figsize=(11,7))
110    ## Setup lines for plottine individual cycles
111    line_colour = ['k-', 'r-', 'b-', 'g-', 'm-', 'k--', '
112                  r--', 'b--', 'g--', \
113                  'm--', 'k-.', 'r-.', 'b-.', 'g-.', 'm
114                  -.', 'k:', 'r:', 'b:', \
115                  'g:', 'm:']
116    styles = len(line_colour)
117    cycle = 0
118    reset = True
119    for n in range(len(voltage)):
120        if reset == True:
121            voltage_cycle = [voltage[n]]
122            current_cycle = [current[n]]
123            reset = False
124            cycle += 1
125        else:
126            voltage_cycle.append(voltage[n])
127            current_cycle.append(current[n])
128
129    if float(vertex1) < float(vertex2):
130        if (n == len(voltage)-1) or \
131            (voltage[n-1] > voltage[n] and voltage[n]
132             < voltage[n+1]):
```

```

128         style = cycle%styles - 1
129         plot(voltage_cycle, current_cycle,
130              line_colour[style], linewidth=0.5,\
              clip_on=False, solid_capstyle='
              round', solid_joinstyle='round'
              )
131         reset = True
132         print("Cycle {} plotted".format(cycle))
133     else:
134         if (n == len(voltage)-1) or\
135             (voltage[n-1] < voltage[n] and voltage[n]
136              > voltage[n+1]):
137             style = cycle%styles
138             plot(voltage_cycle, current_cycle,
139                  line_colour[style], linewidth=0.5,\
140                  clip_on=False, solid_capstyle='
141                  round', solid_joinstyle='round'
142                  )
143             reset = True
144             print("Cycle {} plotted".format(cycle))
145
146     xlabel("U / V")
147     ylabel("I / mA")
148     title("{:}, {:} {:}".format(file_name, rate,
149                                rate_unit))
150
151     ## Save the figure
152     savefig(CV_file_name+"/"+file_name+"_cycles.svg")
153     savefig(CV_file_name+"/"+file_name+"_cycles.pdf")
154     print("Saved CV {} with seperate cycles.\n".format(
155           file_name))
156
157     voltage = []
158     current = []
159     time = []
160     close('all')

```

D.5 Plotting Setaram TG-Analyser Data

The Setaram TG-Analyser can output .txt files, which this program will plot. The program will plot four graphs – mass against time, mass

against temperature, temperature against time, and relative mass against temperature. For this last plot, the program used the initial mass recorded in the header, rather than the first mass actually recorded; these two masses are different because different gas flow rates were used when they were measured, but the difference should be negligible. The header does not record the gas flow rate used.

```
1 from numpy import array
2 #from string import replace
3 from matplotlib.pyplot import plot, savefig, xlabel,
   xlabel, ylim, ylabel, title,\
4     figure, show
5
6 ## Get file name
7 while True:
8     TGA_file_name = input("Enter the file name: ")
9     if TGA_file_name[-4:].lower() == ".txt":
10         TGA_file_name = TGA_file_name[:-4]
11     else:
12         TGA_file_name = TGA_file_name
13
14     try:
15         file = open(TGA_file_name+".txt")
16         file.close()
17         break
18     except:
19         print("File not found.")
20
21 ## Name that will be used for the different plots
22 file_base = TGA_file_name+"_"
23
24 ## Parse the header then extract the data
25 with open(TGA_file_name+".txt") as TGA_file:
26     while True:
27         line = TGA_file.readline()
28
29         ## Get the initial mass
30         if "Initial Mass" in line:
31             initial_mass = float(line[16:-4])
32
33         ## Find the start of the data block and start
           compiling the data
```

```

34     if "Index\tTime (s)\tFurnace Temperature" in
        line:
35         line = TGA_file.readline()
36
37         ## Initalise arrays for each variable
38         index, time, temp, mass = line.strip('\n').
            split('\t')
39
40         indexes = [int(index)]
41         times = [float(time)]
42         temps = [float(temp)]
43         masses = [float(mass)]
44
45         ## Read all of the data
46         while True:
47             line = TGA_file.readline()
48
49             if line == "":
50                 break
51             else:
52                 index, time, temp, mass = line.
                    replace(',','').split('\t')
53
54                 indexes.append(int(index))
55                 times.append(float(time))
56                 temps.append(float(temp))
57                 masses.append(float(mass))
58         break
59
60     ## Plot as a time series
61     figure(figsize=(11,7))
62     plot(times, masses, 'r-', linewidth=0.5, clip_on=False,
63          solid_capstyle='round',\
64          solid_joinstyle='round')
65     title(file_base.format("time"))
66     xlabel("Time / s")
67     ylabel("Mass / mg")
68     savefig(file_base.format("time.pdf"))
69     savefig(file_base.format("time.svg"))
70
71     ## Plot as a temp series
72     figure(figsize=(11,7))

```

```
72 plot(temps, masses, 'r-', linewidth=0.5, clip_on=False,
      solid_capstyle='round',\
73      solid_joinstyle='round')
74 title(file_base.format("temp"))
75 xlabel("Temperature / C")
76 ylabel("Mass / mg")
77 savefig(file_base.format("temp.pdf"))
78 savefig(file_base.format("temp.svg"))
79
80 ## Plot temp against time
81 figure(figsize=(11,7))
82 plot(times, temps, 'r-', linewidth=0.5, clip_on=False,
      solid_capstyle='round',\
83      solid_joinstyle='round')
84 title(file_base.format("temp/time"))
85 xlabel("Time / s")
86 ylabel("Temperature / C")
87 savefig(file_base.format("temp_time.pdf"))
88 savefig(file_base.format("temp_time.svg"))
89
90 ## Plot relative mass against temperature
91 delta_mass = 100*array(masses)/initial_mass
92
93 figure(figsize=(11,7))
94 plot(temps, delta_mass, 'r-', linewidth=0.5, clip_on=
      False, solid_capstyle='round',\
95      solid_joinstyle='round')
96 ylim((0,110))
97 title(file_base.format("temp"))
98 xlabel("Temperature / C")
99 ylabel("Mass / %")
100 savefig(file_base.format("delta-temp.pdf"))
101 savefig(file_base.format("delta-temp.svg"))
```

D.6 Plotting Jasco FT/IR Data

The Jasco FT/IR 6400 Spectrometer can export .txt files, which this program will plot. The program was written for transmittance data, however because it extracts the x- and y-axis data from the files header, it could plot data collected in other operating modes. Changes may need to be made to the x- and y- limits currently set, but this is trivial.

```

1 from numpy import array
2 from matplotlib.pyplot import plot, savefig, xlabel,
  ylim, ylabel, title,\
3     figure, show, xlim
4
5 ## Get file name
6 while True:
7     IR_file_name = input("Enter the file name: ")
8     if IR_file_name[-4:].lower() == ".txt":
9         IR_file_name = IR_file_name[:-4]
10    else:
11        IR_file_name = IR_file_name
12
13    try:
14        file = open(IR_file_name+".txt")
15        file.close()
16        break
17    except:
18        print("File not found.")
19
20 ## Name that will be used for the different plots
21 file_base = IR_file_name+"_{}"
22
23 ## Parse the header then extract the data
24 with open(IR_file_name+".txt") as IR_file:
25     while True:
26         line = IR_file.readline()
27
28         ## Get x any y axes labels
29         if "XUNITS" in line:
30             junk, x_units = line.replace(',','').split(
31                 '\t')
32         if "YUNITS" in line:
33             junk, y_units = line.replace(',','').split(
34                 '\t')
35
36         ## Get the first and last wavenumbers
37         if "FIRSTX" in line:
38             junk, wave_no_start = line.replace(',','').split('\t')
39         if "LASTX" in line:
40             junk, wave_no_end = line.replace(',','').split('\t')

```

D Spectra Plotting and Analysis Programs

```
39
40     ## Find the start of the data block and start
      compiling the data
41     if "XYDATA" in line:
42         line = IR_file.readline()
43
44         ## Initialise arrays for each variable
45         wave_no, transmittance = line.replace(',', '.
          ').split('\t')
46
47         wave_nos = [float(wave_no)]
48         transmittances = [float(transmittance)]
49
50         ## Read all of the data
51         while True:
52             line = IR_file.readline()
53             #print(line)
54
55             wave_no, transmittance = line.replace(',
          ', '.').split('\t')
56
57             wave_nos.append(float(wave_no))
58             transmittances.append(float(
          transmittance))
59
60             ## Stop reading data after the final
          wavenumber
61             if wave_no in wave_no_end:
62                 break
63         break
64
65     ## Plot the spectra
66     figure(figsize=(11,7))
67     plot(wave_nos, transmittances, 'r-', linewidth=0.5,
          clip_on=False,\
68         solid_capstyle='round', solid_joinstyle='round')
69     ylim(0, 100) ## Set y-limits
70     xlim(3700, 400) ## Set x-limits
71     title(IR_file_name)
72     xlabel(x_units)
73     ylabel(y_units)
74     savefig(IR_file_name+".pdf")
75     savefig(IR_file_name+".svg")
```


E Charge Correction in the ILSS Group

Tables E.2, E.3, and E.1 list all of the ionic liquid-related publications (excluding reviews) to date of the Ionic Liquid Surface Science (ILSS) group. These tables are also summarised in figure E.1. 16 publications use the Fermi edge and/or most prominent line of a metal foil or crystal, 12 use a line due to an ion, and 10 do not specify any charge correction.

The use of the Au $4f_{7/2}$ line as an external reference (i. e. instrument binding energy scale calibration) is associated with early (pre-2011) studies of bulk ILs, although two papers of this time period did use the C_{alkyl} line as an internal reference (see table E.2). However, from 2011 onwards, the use of Fermi edges and metal lines is associated with thin-film studies, where they act as internal references.

With the exception of the 2013 paper by Deyko et al.¹⁰¹, all of the papers that used an ion as the charge reference were studies of bulk ILs (mostly in the form of ~ 0.1 mm films). This practice makes sense, since it is obviously not possible to use a line of the underlying substrate as an internal reference. The choice of line used as an internal reference depends on the ILs studied – no one line can be considered a ‘universal’ internal reference. The Deyko et al.¹⁰¹ paper, however, was a study of an IL deposited onto a mica substrate by physical vapour deposition (PVD). This was classed as an ‘ion’ reference simply because the potassium in the substrate is in a cationic form.

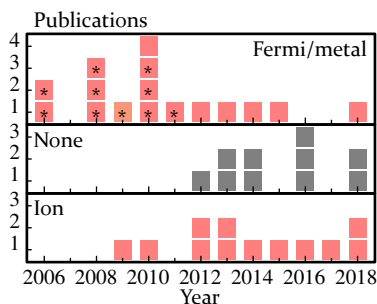


Figure E.1. Type of charge reference used in ILSS group publications. *External reference.

Paper	Year	Chamber	Reference	eV	$C_{\text{alkyl}}/\text{eV}$
Lexow et al. ⁴	2018	ESCA	Fermi, Ag $3d_{5/2}$	368.2	—
Rietzler et al. ⁸⁶	2015	ESCA	Fermi, Ni $2p_{3/2}$	852.4	284.5
Rietzler et al. ⁸⁷	2014	ESCA	Fermi, Au $4f_{7/2}$	83.85	—
Uhl et al. ⁸⁸	2013	ESCA	Fermi, Ni	—	—
Cremer et al. ⁸⁹	2012	ESCA	Fermi, Ni	—	—
Cremer et al. ⁹⁰	2011	ESCA	Fermi, Au $4f_{7/2}^*$	83.85	—
Kolbeck et al. ⁹¹	2010	ESCA	Au $4f_{7/2}^{*\ddagger}$	83.55	—
Kolbeck et al. ⁹²	2010	ESCA	Au $4f_{7/2}^{*\ddagger}$	83.55	—
Sobota et al. ⁹³	2010	mini-ESCA	Fermi, Au $4f_{7/2}$	83.95	—
Maier et al. ²⁸	2010	ESCA	Au $4f_{7/2}^*$	83.55	—
Lovelock et al. ⁶⁷	2009	ESCA	Au $4f_{7/2}^*$	83.55	—
Cremer et al. ⁹⁴	2008	ESCA	Au $4f_{7/2}^*$	83.55	—
Kolbeck et al. ¹⁴	2008	ESCA	Au $4f_{7/2}^*$	83.55	—
Paape et al. ⁹⁵	2008	ESCA	Au $4f_{7/2}^*$	83.55	—
Gottfried et al. ⁹⁶	2006	ESCA	Au $4f_{7/2}^*$	83.55	—
Maier et al. ⁹⁷	2006	ESCA	Au $4f_{7/2}^*$	83.55	—

Table E.1.: Charge references based on metal lines and Fermi edges used in ILSS group publications.*External reference.
[‡]Charge correction details form a referenced publication.

Paper	Year	Chamber	Reference	eV	C_{alkyl} / eV
May et al. ⁵	2018	ESCA	C_{alkyl}	284.8	284.8
Heller et al. ⁹⁸	2018	DASSA	F 1s	686.8, 655.8	285.0
May et al. ³	2017	DASSA	N_{1m}	401.82	—
Tang et al. ²	2016	ESCA	I 3d _{5/2}	619.5	—
Matsuda et al. ⁹⁹	2015	ESCA	N_{1m} 1s	402.2	—
Kolbeck et al. ¹⁰⁰	2014	ESCA	S 2p _{3/2}	168.3, 168.7	—
Kolbeck et al. ³⁰	2013	ESCA	C_{alkyl}	285.0	285.0
Deyko et al. ¹⁰¹	2013	ESCA	K 2p _{1/2}	296.6	—
Taccardi et al. ¹⁰²	2012	ESCA	[Tf ₂ N] ⁻	—*	—
Kolbeck et al. ¹⁰³	2012	ESCA	N_{1m} 1s	401.9	—
Cremer et al. ⁸	2010	ESCA	C_{alkyl}	285.0	285.0
Kolbeck et al. ¹⁰⁴	2009	ESCA	C_{alkyl}	285.0	285.0

Table E.2.: Charge references based on ion-derived lines used in ILSS group publications. *Charge correction was performed, but the exact line and position used are not specified.

Paper	Year	Chamber	Reference	eV	C_{alkyl} / eV
Bhuin et al. ¹⁰⁵	2018	DASSA	none	—	—
Shimizu et al. ¹⁰⁶	2018	ESCA	none	—	—
Rietzler et al. ¹	2016	ESCA	none	—	—
Scheuermeyer et al. ¹⁰⁷	2016	DASSA	none	—	—
Niedermaier et al. ³⁵	2016	DASSA	none	—	284.7
Kolbeck et al. ¹⁰⁸	2014	ESCA	none	—	—
Niedermaier et al. ³¹	2014	NAP, ESCA	none	—	—
Deyko et al. ⁶⁸	2013	ESCA	none	—	—
Niedermaier et al. ¹⁰⁹	2013	ESCA	none	—	—
Niedermaier et al. ²⁶	2012	ESCA	none	—	285.0

Table E.3.: ILSS group publications where no charge correction was reported.

Publications that do not report any charge correction are mostly studies of bulk ILs, with the exception of the 2016 paper by Rietzler et al.¹ and the 2013 paper by Deyko et al.⁶⁸, the latter of which looked at both bulk and thin film molten salts. Another commonality of these publications focused on surface ordering at the vacuum-liquid interface, except for three papers by Niedermaier and co-workers that focused on reactions occurring in IL solution (published in 2014,³¹ 2013,¹⁰⁹ and in 2012²⁶).

Overall, studies focusing on bulk ILs have abandoned the use of Au $4f_{7/2}$ as an external reference (although this line is still used to calibrate the energy scale of the spectrometer during commissioning), and in cases where charge correction is applied, the lines used are derived from one of the ionic species present. For thin film studies, a line derived from the metal substrate is generally used as an internal reference, if one is used.

F Graphics Standard For Thesis Work

F.1 Colour

Aside from photographs, two base colours shall be used - red (#FF0000) and black (#000000). All colours shall be derived from these two base colours, by applying one of four alpha levels: 255 (#FF, fully alpha), 192 (#C0, 75 % alpha), 128 (#80, 50 % alpha), and 64 (#40, 25 % alpha) – examples are presented in figure F.1. However, in actual graphics the use of transparency is to be avoided. In the case of black three full alpha shades of grey may be used: 70 % grey (#4D4D4DFF), 50 % grey (#808080FF), and 30 % grey (#B3B3B3FF). In the case of red three full alpha shades of pink may be used: 3F pink (#FF3F3FFF), 7F pink (#FF7F7FFF), and BF pink (#FFBF3FFF).

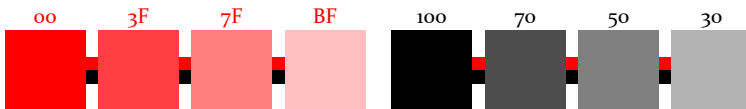


Figure F.1.: Colour swatches, with hex G and B values for red shades (left) and grey percentage (right).

For label text (except text labelling data lines and indicator lines), axes labels (including numbers), labels not otherwise specified, black shall be used. For data labels and indicator line labels, the text colour shall match that of the data/indicator line. For graph frames, axis ticks, and most other lines not otherwise detailed, the colour black shall be used. For indicator lines, black shall be the primary colour, and where clarity, or the density of different indicator lines, 50 % grey shall be used. For data lines, black shall be the primary colour, and for multiple lines plotted in the same graph, the data line colour shall alternate

between black and red. For components in spectra, the line colour shall be black and the fill shall be red with an alpha of 64. The summation of components (if shown) shall be a black line with no fill, or a fill of 64 alpha red with no line.

F.2 Line Weights and Dashes

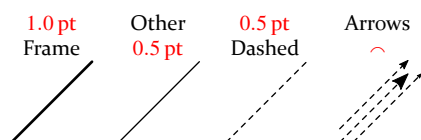


Figure F.2.: Line types.

used. For all lines, the order (from bottom to top) shall be fill, stroke, marker. Dashed lines shall use the 3rd equal on-off dash style. Arrows shall be of the type with the rounded back.

The frame around each graph and outliers in schematics shall have a weight of 1.0 pt. All other lines shall have a weight of 0.5 pt. Except for axis ticks, all lines shall have round end caps and round joints. For the axis ticks, butt caps shall be

F.3 Dimensions

For all graphics, dimensions shall be set in points. Note that Inkscape works with pixels internally, so if the DPI setting is changed (Document Properties > Page > Scale) then the absolute size of all objects on the page will change. Graph width shall be measured as in figure F.3. Graphs shall be 130 pt wide for half page-width figures and two graphs placed side by side in a full page-width figure. Wide spectra shall be plotted in a graph that is 260 pt wide. Other full page-width graphs shall be 230 pt or 260 pt wide.

F.4 Micrographs

For micrographs that are 1024×768 px (i. e. the standard export size of the SEM), the micrograph shall have a scale bar placed in the bottom left corner (unless doing so would obscure an important feature of the micrograph, in which case another corner shall be used, as appropriate). The scale bar shall consist of a 390×100 px (width \times height) black (#000000) rectangle with a single 10 px high white (#FFFFFF) bar, centred horizontally and offset from the bottom of the rectangle

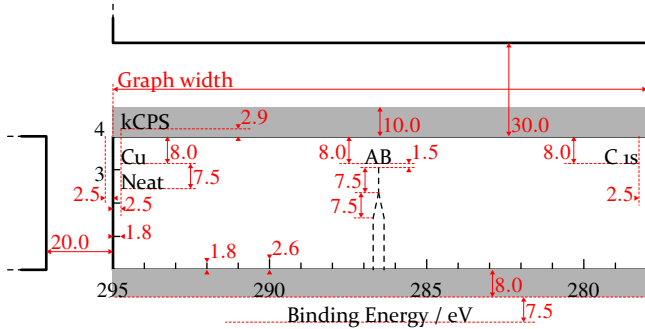


Figure F.3.: Dimensions to be used for all graphs, given in points. Gray areas represent the height to use for setting the vertical page size.

by 10 px, of appropriate width to represent the scale. The white bar shall not be sub-divided. Text giving the scale shall be white (#FFFFFF) and placed above the bar (with the top of the text's bounding box on the edge of the black rectangle, as in figure F.4), shall be of size 60 px, and centred horizontally. The typeface shall be Sans-serif (typically selected as the default in GIMP), with antialiasing disabled. For both the text and the scale bar, if perfect horizontal centring is not possible due to the element being an odd number of pixels wide, the extra pixel shall be placed on the right of centre.

For labels, a black (#000000) rectangle of size 47×71 px, along with one capital letter (of the same typeface, size etc. as specified above), positioned vertically such that the upper and lower bounding box are at the edge of the black box, and centred horizontally (displaced one pixel to the right if the width of the bounding box is an uneven number of pixels). The label shall be placed in the top left hand corner, unless in-



Figure F.4.: Text alignment for scale bars and labels in micrographs.

dicating a particular feature or region, or doing so would obscure some important feature.

When compiling several images into one larger image, a white (#FFFFFF) boundary of 5 px width shall be placed between each micrograph, but no border around the image as a whole shall be used.

Bibliography

- [1] F. Rietzler, B. May, H.-P. Steinrück and F. Maier. 'Switching adsorption and growth behavior of ultrathin [C₂C₁Im][OTf] films on Au(111) by Pd deposition'. In: *Physical Chemistry Chemical Physics* 18 (36 2016), pp. 25143–25150. DOI: 10.1039/C6CP04938A.
- [2] X. Tang, M. Brandl, B. May et al. 'Photoinduced degradation of methylammonium lead triiodide perovskite semiconductors'. In: *Journal of Materials Chemistry A* 4 (41 2016), pp. 15896–15903. DOI: 10.1039/C6TA06497C.
- [3] B. May, M. Hönlle, B. Heller, F. Greco, R. Bhui, H.-P. Steinrück and F. Maier. 'Surface-Induced Changes in the Thermo-chromic Transformation of an Ionic Liquid Cobalt Thiocyanate Complex'. In: *The Journal of Physical Chemistry Letters* 8.6 (2017), pp. 1137–1141. DOI: 10.1021/acs.jpcllett.7b00142.
- [4] M. Lexow, T. Talwar, B. S. J. Heller, B. May, R. G. Bhui, F. Maier and H.-P. Steinrück. 'Time-dependent changes in the growth of ultrathin ionic liquid films on Ag(111)'. In: *Physical Chemistry Chemical Physics* 20 (18 2018), pp. 12929–12938. DOI: 10.1039/C8CP01411F.
- [5] B. May, M. Lexow, N. Taccardi, H.-P. Steinrück and F. Maier. 'Reactions of a Polyhalide Ionic Liquid with Copper, Silver, and Gold'. In: *ChemistryOpen* (2018). DOI: 10.1002/open.201800149.
- [6] H.-P. Steinrück and P. Wasserscheid. 'Ionic Liquids in Catalysis'. In: *Catalysis Letters* 145 (2015), p. 380. DOI: 10.1007/s10562-14-1435-x.
- [7] M. Gorlov and L. Kloo. 'Ionic liquid electrolytes for dye-sensitized solar cells'. In: *Dalton Transactions* (20 2008), pp. 2655–2666. DOI: 10.1039/B716419J.

- [8] S. P. Borikar, T. Daniel and V. Paul. 'An efficient, rapid, and regioselective bromination of anilines and phenols with 1-butyl-3-methylpyridinium tribromide as a new reagent/solvent under mild conditions'. In: *Tetrahedron Letters* 50.9 (2009), pp. 1007–1009. ISSN: 0040-4039. DOI: 10.1016/j.tetlet.2008.12.053.
- [9] P. Wasserscheid and W. Keim. 'Ionic Liquids—New “Solutions” for Transition Metal Catalysis'. In: *Angewandte Chemie International Edition* 39.21 (2000), pp. 3772–3789. DOI: 10.1002/1521-3773(20001103)39:21<3772::AID-ANIE3772>3.0.CO;2-5.
- [10] T. Welton. 'Ionic liquids in catalysis'. In: *Coordination Chemistry Reviews* 248.21 (2004), pp. 2459–2477. DOI: 10.1016/j.ccr.2004.04.015.
- [11] H.-P. Steinrück. 'Recent developments in the study of ionic liquid interfaces using X-ray photoelectron spectroscopy and potential future directions'. In: *Physical Chemistry Chemical Physics* 14 (15 2012), pp. 5010–5029. DOI: 10.1039/C2CP24087D.
- [12] F. Maier, I. Niedermaier and H.-P. Steinrück. 'Perspective: Chemical reactions in ionic liquids monitored through the gas (vacuum)/liquid interface'. In: *The Journal of Chemical Physics* 146.17 (2017), p. 170901. DOI: 10.1063/1.4982355.
- [13] R. F. Roberts, D. L. Allara, C. A. Pryde, D. N. E. Buchanan and N. D. Hobbins. 'Mean free path for inelastic scattering of 1.2 keV electrons in thin poly(methylmethacrylate) films'. In: *Surface and Interface Analysis* 2.1 (1980), pp. 5–10. DOI: 10.1002/sia.740020103.
- [14] C. Kolbeck, M. Killian, F. Maier, N. Paape, P. Wasserscheid and H.-P. Steinrück. 'Surface Characterization of Functionalized Imidazolium-Based Ionic Liquids'. In: *Langmuir* 24.17 (2008), 9500–9507. DOI: 10.1021/la801261h.
- [15] C. P. Mehnert. 'Supported Ionic Liquid Phases'. In: *Chemistry – A European Journal* 11 (2005), p. 50. DOI: 10.1002/chem.200400683.
- [16] '17 – The Halogens: Fluorine, Chlorine, Bromine, Iodine and Astatine'. In: *Chemistry of the Elements (Second Edition)*. Ed. by N. Greenwood and A. Earnshaw. Second Edition. Oxford: Butterworth-Heinemann, 1997, pp. 789–887. ISBN: 978-0-7506-3365-9.

- [17] C. E. Housecroft and A. G. Sharpe. '17 – The Group 17 Elements'. In: *Inorganic Chemistry*. Third Edition. Harlow: Pearson Education Limited, 2008, pp. 532–560. ISBN: 978-0-13-175553-6.
- [18] T. Cremer, C. Kolbeck, K. R. J. Lovelock et al. 'Towards a Molecular Understanding of Cation–Anion Interactions—Probing the Electronic Structure of Imidazolium Ionic Liquids by NMR Spectroscopy, X-ray Photoelectron Spectroscopy and Theoretical Calculations'. In: *Chemistry – A European Journal* 16.30 (2010), pp. 9018–9033. DOI: 10.1002/chem.201001032.
- [19] M. Georgiadou and R. Alkire. 'Anisotropic Chemical Etching of Copper Foil: I. Electrochemical Studies in Acidic Solutions'. In: *Journal of The Electrochemical Society* 140.5 (1993), pp. 1340–1347. DOI: 10.1149/1.2220981.
- [20] S. Walter, M. Haumann, P. Wasserscheid, H. Hahn and R. Franke. 'n-Butane Carbonylation to n-Pentanal Using a Cascade Reaction of Dehydrogenation and SILP-catalyzed Hydroformylation'. In: *AIChE Journal* 61 (2015), p. 893. DOI: 10.1002/aic.14676.
- [21] C. J. Carrasco, F. Montilla, L. Bobadilla, S. Ivanova, J. A. Odriozola and A. Galindo. 'Oxidiperoxomolybdenum Complex Immobilized onto Ionic Liquid Modified SBA-15 as an Effective Catalysis for Sulfide Oxidation to Sulfoxides Using Hydrogen Peroxide'. In: *Catalysis Today* 255 (2015), p. 102. DOI: 10.1016/j.cattod.2014.10.053.
- [22] L. B. Malihan, G. M. Nisola, N. Mittal, S.-P. Lee, J. G. Seo, H. Kim and W.-J. Chung. 'SBA-15 Supported Ionic Liquid Phase (SILP) with H₂PW₁₂O₄₀⁻ for the Hydrolytic Catalysis of Red Macroalgal Biomass to Sugars'. In: *RSC Advances* 6 (2016), p. 33901. DOI: 10.1039/C6RA03740B.
- [23] D. C. Frost, A. Ishitani and C. A. McDowell. 'X-ray Photoelectron Spectroscopy of Copper Compounds'. In: *Molecular Physics* 24 (1972), p. 861. DOI: 10.1080/00268977200101961.
- [24] D. C. Frost, C. A. McDowell and I. S. Woolsey. 'X-ray Photoelectron Spectra of Cobalt Compounds'. In: *Molecular Physics* 27 (1974), p. 1473. DOI: 10.1080/00268977400101251.

- [25] D. Briggs and V. A. Gibson. 'Direct Observation of Multiplet Splitting in 2P Photoelectron Peaks of Cobalt Complexes'. In: *Chemical Physics Letters* 25 (1974), p. 493. DOI: 10.1016/0009-2614(74)85350-9.
- [26] I. Niedermaier, C. Kolbeck, N. Taccardi, P. S. Schulz, J. Li, T. Drewello, P. Wasserscheid, H.-P. Steinrück and F. Maier. 'Organic Reactions in Ionic Liquids Studied by in situ XPS'. In: *ChemPhysChem* 13 (2012), p. 1725. DOI 10.1002/cphc.201290030
- [27] P. Licence. 'In Situ XPS Monitoring of Bulk Ionic Liquid Reactions: Shedding Light on Organic Reaction Mechanisms'. In: *Angewandte Chemie International Edition* 51 (2012), p. 4789. DOI: 10.1002/anie.201201070.
- [28] F. Maier, T. Cremer, C. Kolbeck, K. R. J. Lovelock, N. Paape, P. S. Schulz, P. Wasserscheid and H.-P. Steinrück. 'Insights into the Surface Composition and Enrichment Effects of Ionic Liquids and Ionic Liquid Mixtures'. In: *Physical Chemistry Chemical Physics* 12 (2010), p. 1905. DOI: 10.1039/b920804f
- [29] K. R. J. Lovelock, I. J. Villar-Garcia, F. Maier, H.-P. Steinrück and P. Licence. 'Photoelectron Spectroscopy of Ionic Liquid-Based Interfaces'. In: *Chemical Reviews* 110 (2010), p. 5158. DOI: 10.1021/cr100114t.
- [30] C. Kolbeck, A. Deyko, T. Matsuda, F. Kohler, P. Wasserscheid, F. Maier and H.-P. Steinrück. 'Temperature-Dependent Surface-Enrichment Effects of Imidazolium-Based Ionic Liquids'. In: *ChemPhysChem* 14 (2013), p. 3726. DOI: 10.1002/cphc.201300719.
- [31] I. Niedermaier, M. Bahlmann, C. Papp et al. 'Carbon Dioxide Capture by an Amine Functionalized Ionic Liquid: Fundamental Differences of Surface and Bulk Behavior'. In: *Journal of the American Chemical Society* 136 (2014), p. 436. DOI: 10.1021/ja410745a
- [32] T. Peppel, M. Köckerling, M. Geppert-Rybczyńska, R. V. Ralys, J. Lehmann, S. P. Verevkin and A. Heintz. 'Low-Viscosity Paramagnetic Ionic Liquids with Doubly Charged [Co(NCS)₄]²⁻Ions'. In: *Angewandte Chemie International Edition* 49.39 (2010), 7116–7119. ISSN: 1521-3773. DOI: 10.1002/anie.201000709.

- [33] S. J. Osborne, S. Wellens, C. Ward, S. Felton, R. M. Bowman, K. Binnemans, M. Swadzba-Kwasny, H. Q. N. Gunaratne and P. Nockemann. 'Thermochromism and switchable paramagnetism of cobalt(ii) in thiocyanate ionic liquids'. In: *Dalton Transactions* 44 (25 2015), pp. 11286–11289. DOI: 10.1039/C5DT01829C.
- [34] E. McCourt, Z. Wojnarowska, J. Jacquemin, P. Nockemann, H. G. Manyar, L. Hawelek and M. Paluch. 'Temperature- and Pressure-Induced Structural Changes of Cobalt(II) in a Phosphonium-Based Ionic Liquid'. In: *Journal of Physical Chemistry C* 120 (2016), p. 10156. DOI: 10.1021/acs.jpcc.6b01325.
- [35] I. Niedermaier, C. Kolbeck, H.-P. Steinrück and F. Maier. 'Dual analyzer system for surface analysis dedicated for angle-resolved photoelectron spectroscopy at liquid surfaces and interfaces'. In: *Review of Scientific Instruments* 87.4 (2016), p. 045105. DOI: 10.1063/1.4942943.
- [36] M. Mezger, B. M. Ocko, H. Reichert and M. Deutsch. 'Surface layering and melting in an ionic liquid studied by resonant soft X-ray reflectivity'. In: *Proceedings of the National Academy of Sciences* 110.10 (2013), pp. 3733–3737. DOI: 10.1073/pnas.1211749110.
- [37] W. D. Amith, J. J. Hettige, E. W. Castner and C. J. Margulis. 'Structures of Ionic Liquids Having Both Anionic and Cationic Octyl Tails: Lamellar Vacuum Interface vs Sponge-Like Bulk Order'. In: *The Journal of Physical Chemistry Letters* 7.19 (2016), pp. 3785–3790. DOI: 10.1021/acs.jpcclett.6b01763.
- [38] J. Hicks and C. Jones. 'Low-Coordinate Cobalt(I) Complexes Stabilized by an Extremely Bulky Amide Ligand'. In: *Organometallics* 34.11 (2015), pp. 2118–2121. DOI: 10.1021/om501233f.
- [39] H. Haller and S. Riedel. 'Recent Discoveries of Polyhalogen Anions – from Bromine to Fluorine'. In: *Zeitschrift für anorganische und allgemeine Chemie* 640.7 (2014), pp. 1281–1291. ISSN: 1521-3749. DOI: 10.1002/zaac.201400085.
- [40] M. Wolff, A. Okrut and C. Feldmann. '[(Ph)₃PBr][Br₇], [(Bz)(Ph)₃P]₂[Br₈], [(n-Bu)₃MeN]₂[Br₂₀], [C₄MPyr]₂[Br₂₀], and [(Ph)₃PCl]₂[Cl₁₂I₄]: Extending the Horizon of Polyhalides via Synthesis in Ionic Liquids'. In: *Inorganic Chemistry* 50.22 (2011), pp. 11683–11694. DOI: 10.1021/ic201291k.

- [41] S. Men, K. R. Lovelock and P. Licence. 'X-ray photoelectron spectroscopy of trihalide ionic liquids: Comparison to halide-based analogues, anion basicity and beam damage'. In: *Chemical Physics Letters* 679. Supplement C (2017), pp. 207–211. ISSN: 0009-2614. DOI: 10.1016/j.cplett.2017.05.010.
- [42] I. J. Villar-Garcia, E. F. Smith, A. W. Taylor, F. Qiu, K. R. J. Lovelock, R. G. Jones and P. Licence. 'Charging of ionic liquid surfaces under X-ray irradiation: the measurement of absolute binding energies by XPS'. In: *Physical Chemistry Chemical Physics* 13 (7 2011), pp. 2797–2808. DOI: 10.1039/C0CP01587C.
- [43] B. B. Hurisso, K. R. J. Lovelock and P. Licence. 'Amino acid-based ionic liquids: using XPS to probe the electronic environment via binding energies'. In: *Physical Chemistry Chemical Physics* 13 (39 2011), pp. 17737–17748. DOI: 10.1039/C1CP21763A.
- [44] A. W. Taylor, S. Men, C. J. Clarke and P. Licence. 'Acidity and basicity of halometallate-based ionic liquids from X-ray photoelectron spectroscopy'. In: *RSC Advances* 3 (24 2013), pp. 9436–9445. DOI: 10.1039/C3RA40260F.
- [45] M. Fieser and L. Fieser. *Fieser and Fieser's Reagents for Organic Synthesis, Volume 1*. WILEY-VCH Verlag, 1967. ISBN: 0-471-25875-9.
- [46] V. Kavala, S. Naik and B. K. Patel. 'A New Recyclable Ditribromide Reagent for Efficient Bromination under Solvent Free Condition'. In: *The Journal of Organic Chemistry* 70.11 (2005), pp. 4267–4271. DOI: 10.1021/j0050059u.
- [47] T. Schlama, K. Gabriel, V. Gouverneur and C. Mioskowski. 'Tetraethylammonium Trichloride: A Versatile Reagent for Chlorinations and Oxidations'. In: *Angewandte Chemie International Edition in English* 36.21 (1997), pp. 2342–2344. DOI: 10.1002/anie.199723421.
- [48] V. M. Zelikman, V. S. Tyurin, V. V. Smirnov and N. V. Zyk. 'Quaternary ammonium polychlorides as efficient reagents for chlorination of unsaturated compounds'. In: *Russian Chemical Bulletin* 47.8 (1998), pp. 1541–1546. DOI: 10.1007/BF02495606.

- [49] C. Chiappe, D. Capraro, V. Conte and D. Pieraccini. 'Stereoselective Halogenations of Alkenes and Alkynes in Ionic Liquids'. In: *Organic Letters* 3.7 (2001), pp. 1061–1063. DOI: 10.1021/ol015631s.
- [50] J. Salazar and R. Dorta. 'Pentylpyridinium Tribromide: A Vapor Pressure Free Room Temperature Ionic Liquid Analogue of Bromine'. In: *Synlett* 2004.07 (2004), pp. 1318–1320. ISSN: 0936-5214. DOI: 10.1055/s-2004-825598.
- [51] B. O'Regan and M. Grätzel. 'A low-cost, high-efficiency solar cell based on dye-sensitized colloidal TiO₂ films'. In: *Nature* 353.6346 (1991), pp. 737–740. DOI: 10.1038/353737a0.
- [52] M. Grätzel. 'Recent Advances in Sensitized Mesoscopic Solar Cells'. In: *Accounts of Chemical Research* 42.11 (2009), pp. 1788–1798. DOI: 10.1021/ar900141y.
- [53] A. Hagfeldt, G. Boschloo, L. Sun, L. Kloo and H. Pettersson. 'Dye-Sensitized Solar Cells'. In: *Chemical Reviews* 110.11 (2010), pp. 6595–6663. DOI: 10.1021/cr900356p.
- [54] K. Kakiage, T. Tokutome, S. Iwamoto, T. Kyomen and M. Hanaya. 'Fabrication of a dye-sensitized solar cell containing a Mg-doped TiO₂ electrode and a Br₃⁻/Br⁻ redox mediator with a high open-circuit photovoltage of 1.21 V'. In: *Chemical Communications* 49 (2 2013), pp. 179–180. DOI: 10.1039/C2CC36873K.
- [55] J. Moulder and J. Chastain. *Handbook of X-ray Photoelectron Spectroscopy: A Reference Book of Standard Spectra for Identification and Interpretation of XPS Data*. Physical Electronics Division, Perkin-Elmer Corporation, 1992. ISBN: 9780962702624.
- [56] M. Kundel, R.-J. Huang, U. R. Thorenz, J. Bosle, M. J. D. Mann, M. Ries and T. Hoffmann. 'Application of Time-of-Flight Aerosol Mass Spectrometry for the Online Measurement of Gaseous Molecular Iodine'. In: *Analytical Chemistry* 84.3 (2012), pp. 1439–1445. DOI: 10.1021/ac202527a.
- [57] S. S. (director). *NIST Standard Reference Database Number 69. NIST Mass Spec Data Center*. Ed. by P. Linstrom and W. Mallard. National Institute of Standards and Technology, NIST Mass Spec Data Center. 8th July 2018. URL: <https://webbook.nist.gov/cgi/cbook.cgi?ID=C7726956&Mask=1E9F#Mass-Spec>.

- [58] D. C. Frost and C. A. McDowell. 'THE IONIZATION and DISSOCIATION of SOME HALOGEN MOLECULES by ELECTRON IMPACT'. In: *Canadian Journal of Chemistry* 38.3 (1960), pp. 407–420. DOI: 10.1139/v60-057.
- [59] J. Scott McIndoe and D. G. Tuck. 'Studies of polyhalide ions in aqueous and non-aqueous solution by electrospray mass spectrometry'. In: *Dalton Transactions* (2 2003), pp. 244–248. DOI: 10.1039/B208035B.
- [60] N. V. Plechkova and K. R. Seddon. 'Applications of ionic liquids in the chemical industry'. In: *Chemical Society Reviews* 37 (1 2008), pp. 123–150. DOI: 10.1039/Bo06677J.
- [61] S. Yanagida, Y. Yu and K. Manseki. 'Iodine/Iodide-Free Dye-Sensitized Solar Cells'. In: *Accounts of Chemical Research* 42.11 (2009), pp. 1827–1838. DOI: 10.1021/ar900069p.
- [62] T. A. Green. 'Gold etching for microfabrication'. In: *Gold Bulletin* 47.3 (2014), pp. 205–216. DOI: 10.1007/s13404-014-0143-z.
- [63] X. Li, A. Van den Bossche, T. Vander Hoogerstraete and K. Binne-mans. 'Ionic liquids with trichloride anions for oxidative dissolution of metals and alloys'. In: *Chemical Communications* 54 (5 2018), pp. 475–478. DOI: 10.1039/C7CC08645H.
- [64] M. Uerdingen, C. Treber, M. Balsler, G. Schmitt and C. Werner. 'Corrosion behaviour of ionic liquids'. In: *Green Chemistry* 7 (5 2005), pp. 321–325. DOI: 10.1039/B419320M.
- [65] Q. Zhang, Y. Hua and Z. Zhou. 'Corrosion Properties of Copper, Nickel, and Titanium in Alkylimidazolium Chloroaluminate Based Ionic Liquids'. In: *International Journal of Electrochemical Science* 8 (8 2013), pp. 10239–10249.
- [66] B. Dilasari, Y. Jung, J. Sohn, S. Kim and K. Kwon. 'Review on Corrosion Behavior of Metallic Materials in Room Temperature Ionic Liquids'. In: *International Journal of Electrochemical Science* 11 (2 2016), pp. 1482–1495.
- [67] K. R. J. Lovelock, C. Kolbeck, T. Cremer, N. Paape, P. S. Schulz, P. Wasserscheid, F. Maier and H.-P. Steinrück. 'Influence of Different Substituents on the Surface Composition of Ionic Liquids Studied Using ARXPS'. In: *The Journal of Physical Chemistry B* 113.9 (2009), pp. 2854–2864. DOI: 10.1021/jp810637d.

- [68] A. Deyko, S. Bajus, F. Rietzler, A. Bösmann, P. Wasserscheid, H.-P. Steinrück and F. Maier. 'Interface Properties and Physico-chemical Characterization of the Low-Temperature Molten Salt Li/K/Cs Acetate'. In: *The Journal of Physical Chemistry C* 117.44 (2013), pp. 22939–22946. DOI: 10.1021/jp407689c.
- [69] H. Kitagawa, N. Kojima and T. Nakajima. 'Studies of mixed-valence states in three-dimensional halogen-bridged gold compounds, Cs₂AuAuX₆, (X = Cl, Br or I). Part 2. X-Ray photoelectron spectroscopic study'. In: *Journal of the Chemical Society, Dalton Transactions* (11 1991), pp. 3121–3125. DOI: 10.1039/DT9910003121.
- [70] V. K. Kaushik. 'XPS core level spectra and Auger parameters for some silver compounds'. In: *Journal of Electron Spectroscopy and Related Phenomena* 56.3 (1991), pp. 273–277. DOI: 10.1016/0368-2048(91)85008-H.
- [71] S. W. Gaarenstroom and N. Winograd. 'Initial and final state effects in the ESCA spectra of cadmium and silver oxides'. In: *The Journal of Chemical Physics* 67.8 (1977), pp. 3500–3506. DOI: 10.1063/1.435347.
- [72] M. C. Biesinger, L. W. Lau, A. R. Gerson and R. S. Smart. 'Resolving surface chemical states in XPS analysis of first row transition metals, oxides and hydroxides: Sc, Ti, V, Cu and Zn'. In: *Applied Surface Science* 257.3 (2010), pp. 887–898. DOI: 10.1016/j.apsusc.2010.07.086.
- [73] S. Eustis and M. A. El-Sayed. 'Molecular Mechanism of the Photochemical Generation of Gold Nanoparticles in Ethylene Glycol: Support for the Disproportionation Mechanism'. In: *The Journal of Physical Chemistry B* 110.29 (2006), pp. 14014–14019. DOI: 10.1021/jp062972k.
- [74] A. S. K. Hashmi and M. Rudolph. 'Gold catalysis in total synthesis'. In: *Chemical Society Reviews* 37 (9 2008), pp. 1766–1775. DOI: 10.1039/B615629K.
- [75] M. Rudolph and A. S. K. Hashmi. 'Gold catalysis in total synthesis —an update'. In: *Chemical Society Reviews* 41 (6 2012), pp. 2448–2462. DOI: 10.1039/C1CS15279C.

- [76] C. M. Flaminia, P. Cristina, R. Olga, G. Lorenzo, S. Giuseppe and L. Adolfo. 'NMR Investigation of Imidazolium-Based Ionic Liquids and Their Aqueous Mixtures'. In: *ChemPhysChem* 13.5 (2012), pp. 1339–1346. DOI: 10.1002/cphc.201100810.
- [77] A. Deyko, S. G. Hessey, P. Licence, E. A. Chernikova, V. G. Krasovskiy, L. M. Kustov and R. G. Jones. 'The enthalpies of vapourisation of ionic liquids: new measurements and predictions'. In: *Physical Chemistry Chemical Physics* 14 (9 2012), pp. 3181–3193. DOI: 10.1039/C2CP23705A.
- [78] G. Kelsall, N. Welham and M. Diaz. 'Thermodynamics of Cl-H₂O, Br-H₂O, I-H₂O, Au-Cl-H₂O, Au-Br-H₂O and Au-I-H₂O systems at 298 K'. In: *Journal of Electroanalytical Chemistry* 361.1 (1993), pp. 13–24. DOI: 10.1016/0022-0728(93)87034-S.
- [79] C. H. Gammons, Y. Yu and A. Williams-Jones. 'The disproportionation of gold(I) chloride complexes at 25 to 200°C'. In: *Geochimica et Cosmochimica Acta* 61.10 (1997), pp. 1971–1983. DOI: 10.1016/S0016-7037(97)00060-4.
- [80] *Printed circuits handbook*. 4. ed. New York [u.a.]: McGraw-Hill, 1996. ISBN: 0070127549.
- [81] P. C. Andricacos and P. N. Ross. 'Diffusion-Controlled Multi-sweep Cyclic Voltammetry: I. Reversible Deposition on a Rotating Disk Electrode'. In: *Journal of The Electrochemical Society* 130.6 (1983), pp. 1340–1352. DOI: 10.1149/1.2119949.
- [82] K. Murase, K. Nitta, T. Hirato and Y. Awakura. 'Electrochemical behaviour of copper in trimethyl-n-hexylammonium bis((trifluoromethyl)sulfonyl)amide, an ammonium imide-type room temperature molten salt'. In: *Journal of Applied Electrochemistry* 31.10 (2001), pp. 1089–1094. ISSN: 1572-8838. DOI: 10.1023/A:1012255601793.
- [83] D. Lloyd, T. Vainikka, L. Murtomäki, K. Kontturi and E. Ahlberg. 'The kinetics of the Cu₂⁺/Cu⁺ redox couple in deep eutectic solvents'. In: *Electrochimica Acta* 56.14 (2011), pp. 4942–4948. DOI: 10.1016/j.electacta.2011.03.133.
- [84] T. E. Oliphant. *Guide to NumPy*. 2nd ed. USA: CreateSpace Independent Publishing Platform, 2015. ISBN: 9781517300074.

- [85] J. D. Hunter. 'Matplotlib: A 2D graphics environment'. In: *Computing In Science & Engineering* 9.3 (2007), pp. 90–95. DOI: 10.1109/MCSE.2007.55.
- [86] F. Rietzler, J. Nagengast, H.-P. Steinrück and F. Maier. 'Interface of Ionic Liquids and Carbon: Ultrathin [C₁C₁Im][Tf₂N] Films on Graphite and Graphene'. In: *The Journal of Physical Chemistry C* 119.50 (2015), pp. 28068–28076. DOI: 10.1021/acs.jpcc.5b09649.
- [87] F. Rietzler, M. Piermaier, A. Deyko, H.-P. Steinrück and F. Maier. 'Electrospray Ionization Deposition of Ultrathin Ionic Liquid Films: [C₈C₁Im]Cl and [C₈C₁Im][Tf₂N] on Au(111)'. In: *Langmuir* 30.4 (2014), pp. 1063–1071. DOI: 10.1021/la404429q.
- [88] B. Uhl, T. Cremer, M. Roos, F. Maier, H.-P. Steinrück and R. J. Behm. 'At the ionic liquid|metal interface: structure formation and temperature dependent behavior of an ionic liquid adlayer on Au(111)'. In: *Physical Chemistry Chemical Physics* 15 (40 2013), pp. 17295–17302. DOI: 10.1039/C3CP52184B.
- [89] T. Cremer, L. Wibmer, S. K. Calderón, A. Deyko, F. Maier and H.-P. Steinrück. 'Interfaces of ionic liquids and transition metal surfaces—adsorption, growth, and thermal reactions of ultrathin [C₁C₁Im][Tf₂N] films on metallic and oxidised Ni(111) surfaces'. In: *Physical Chemistry Chemical Physics* 14 (15 2012), pp. 5153–5163. DOI: 10.1039/C2CP40278E.
- [90] T. Cremer, M. Stark, A. Deyko, H.-P. Steinrück and F. Maier. 'Liquid/Solid Interface of Ultrathin Ionic Liquid Films: [C₁C₁Im][Tf₂N] and [C₈C₁Im][Tf₂N] on Au(111)'. In: *Langmuir* 27.7 (2011), pp. 3662–3671. DOI: 10.1021/la105007c.
- [91] C. Kolbeck, J. Lehmann, K. R. J. Lovelock, T. Cremer, N. Paape, P. Wasserscheid, A. P. Fröba, F. Maier and H.-P. Steinrück. 'Density and Surface Tension of Ionic Liquids'. In: *The Journal of Physical Chemistry B* 114.51 (2010), pp. 17025–17036. DOI: 10.1021/jp1068413.
- [92] C. Kolbeck, N. Paape, T. Cremer, P. S. Schulz, F. Maier, H.-P. Steinrück and P. Wasserscheid. 'Ligand Effects on the Surface Composition of Rh-Containing Ionic Liquid Solutions Used in Hydroformylation Catalysis'. In: *Chemistry – A European Journal* 16.40 (2010), pp. 12083–12087. DOI: 10.1002/chem.201000903.

- [93] M. Sobota, M. Schmid, M. Happel et al. 'Ionic liquid based model catalysis: interaction of [BMIM][Tf₂N] with Pd nanoparticles supported on an ordered alumina film'. In: *Physical Chemistry Chemical Physics* 12 (35 2010), pp. 10610–10621. DOI: 10.1039/C003753B.
- [94] T. Cremer, M. Killian, J. M. Gottfried, N. Paape, P. Wasserscheid, F. Maier and H.-P. Steinrück. 'Physical Vapor Deposition of [EMIM][Tf₂N]: A New Approach to the Modification of Surface Properties with Ultrathin Ionic Liquid Films'. In: *ChemPhysChem* 9.15 (2008), pp. 2185–2190. DOI: 10.1002/cphc.200800300.
- [95] N. Paape, W. Wei, A. Bösmann, C. Kolbeck, F. Maier, H.-P. Steinrück, P. Wasserscheid and P. S. Schulz. 'Chloroalkylsulfonate ionic liquids by ring opening of sultones with organic chloride salts'. In: *Chemical Communications* (33 2008), pp. 3867–3869. DOI: 10.1039/B805444D.
- [96] J. Gottfried, F. Maier, J. Rossa, D. Gerhard, P. S. Schulz, P. Wasserscheid and H.-P. Steinrück. 'Surface Studies on the Ionic Liquid 1-Ethyl-3-Methylimidazolium Ethylsulfate Using X-Ray Photoelectron Spectroscopy (XPS)'. In: *Zeitschrift für Physikalische Chemie* 220.10 (2006), pp. 1439–1453. DOI: 10.1524/zpch.2006.220.10.1439.
- [97] F. Maier, J. M. Gottfried, J. Rossa, D. Gerhard, P. S. Schulz, W. Schwieger, P. Wasserscheid and H.-P. Steinrück. 'Surface Enrichment and Depletion Effects of Ions Dissolved in an Ionic Liquid: An X-ray Photoelectron Spectroscopy Study'. In: *Angewandte Chemie International Edition* 45.46 (2006), pp. 7778–7780. DOI: 10.1002/anie.200602756.
- [98] B. S. J. Heller, C. Kolbeck, I. Niedermaier, S. Dommer, J. Schatz, P. Hunt, F. Maier and H.-P. Steinrück. 'Surface Enrichment in Equimolar Mixtures of Non-Functionalized and Functionalized Imidazolium-Based Ionic Liquids'. In: *ChemPhysChem* 19.14 (2018), pp. 1733–1745. DOI: 10.1002/cphc.201800216.
- [99] T. Matsuda, N. Taccardi, J. Schwegler, P. Wasserscheid, H.-P. Steinrück and F. Maier. 'Vacuum Surface Science Meets Heterogeneous Catalysis: Dehydrogenation of a Liquid Organic Hydrogen Carrier in the Liquid State'. In: *ChemPhysChem* 16.9 (2015), pp. 1873–1879. DOI: 10.1002/cphc.201500236.

- [100] C. Kolbeck, N. Taccardi, N. Paape, P. S. Schulz, P. Wasserscheid, H.-P. Steinrück and F. Maier. 'Redox chemistry, solubility, and surface distribution of Pt(II) and Pt(IV) complexes dissolved in ionic liquids'. In: *Journal of Molecular Liquids* 192 (2014). Fundamental Aspects of Ionic Liquid Science, pp. 103–113. DOI: 10.1016/j.molliq.2013.07.007.
- [101] A. Deyko, T. Cremer, F. Rietzler, S. Perkin, L. Crowhurst, T. Welton, H.-P. Steinrück and F. Maier. 'Interfacial Behavior of Thin Ionic Liquid Films on Mica'. In: *The Journal of Physical Chemistry C* 117.10 (2013), pp. 5101–5111. DOI: 10.1021/jp3115397.
- [102] N. Taccardi, I. Niedermaier, F. Maier, H.-P. Steinrück and P. Wasserscheid. 'Cyclic Thiouronium Ionic Liquids: Physicochemical Properties and their Electronic Structure Probed by X-Ray Induced Photoelectron Spectroscopy'. In: *Chemistry – A European Journal* 18.27 (2012), pp. 8288–8291. DOI: 10.1002/chem.201200971.
- [103] C. Kolbeck, I. Niedermaier, N. Taccardi, P. S. Schulz, F. Maier, P. Wasserscheid and H.-P. Steinrück. 'Monitoring of Liquid-Phase Organic Reactions by Photoelectron Spectroscopy'. In: *Angewandte Chemie International Edition* 51.11 (2012), pp. 2610–2613. DOI: 10.1002/anie.201107402.
- [104] C. Kolbeck, T. Cremer, K. R. J. Lovelock, N. Paape, P. S. Schulz, P. Wasserscheid, F. Maier and H.-P. Steinrück. 'Influence of Different Anions on the Surface Composition of Ionic Liquids Studied Using ARXPS'. In: *The Journal of Physical Chemistry B* 113.25 (2009), pp. 8682–8688. DOI: 10.1021/jp902978r.
- [105] R. G. Bhui, P. Schreiber, B. S. Heller, M. Scheuermeyer, P. Wasserscheid, H.-P. Steinrück and F. Maier. 'Surface behavior of low-temperature molten salt mixtures during the transition from liquid to solid'. In: *Journal of Molecular Liquids* 275 (2019), pp. 290–296. DOI: 10.1016/j.molliq.2018.11.056.
- [106] K. Shimizu, B. S. J. Heller, F. Maier, H.-P. Steinrück and J. N. Canongia Lopes. 'Probing the Surface Tension of Ionic Liquids Using the Langmuir Principle'. In: *Langmuir* 34.14 (2018), 4408–4416. DOI: 10.1021/acs.langmuir.7b04237.
- [107] M. Scheuermeyer, M. Kusche, F. Agel, P. Schreiber, F. Maier, H.-P. Steinrück, J. H. Davis, F. Heym, A. Jess and P. Wasserscheid. 'Thermally stable bis(trifluoromethylsulfonyl)imide salts and

- their mixtures'. In: *New Journal of Chemistry* 40 (8 2016), pp. 7157–7161. DOI: 10.1039/C6NJ00579A.
- [108] C. Kolbeck, I. Niedermaier, A. Deyko, K. R. J. Lovelock, N. Taccardi, Wei, P. Wasserscheid, F. Maier and H.-P. Steinrück. 'Influence of Substituents and Functional Groups on the Surface Composition of Ionic Liquids'. In: *Chemistry – A European Journal* 20.14 (2014), pp. 3954–3965. DOI: 10.1002/chem.201304549.
- [109] I. Niedermaier, N. Taccardi, P. Wasserscheid, F. Maier and H.-P. Steinrück. 'Probing a Gas/Liquid Acid–Base Reaction by X-ray Photoelectron Spectroscopy'. In: *Angewandte Chemie International Edition* 52.34 (2013), pp. 8904–8907. DOI: 10.1002/anie.201304115.

In this thesis, studies involving ionic liquids (ILs) in the context of IL-transition metal reactions were reported on: the thermochromatic transformation of a cobalt thiocyanate-containing IL, the characterisation of polyhalide ionic liquids, the corrosion of group 11 metals by trihalide ILs, and the comproportionation of copper metal and CuI salts in solution. X-ray photoelectron spectroscopy (XPS) was the main technique used in all of these studies, but other techniques such as mass spectrometry (MS) and scanning electron microscopy (SEM) were also used.

